FLORIDA STATE UNIVERSITY

COLLEGE OF ENGINEERING

APPLICATION OF PARTICLE TRACKING VELOCIMETRY TO THERMAL

COUNTERFLOW AND TOWED-GRID TURBULENCE IN HELIUM II

By

BRIAN MASTRACCI

A Dissertation submitted to the
Department of Mechanical Engineering
in partial fulfillment of the
requirements for the degree of
Doctor of Philosophy

2018

Brian Mastracci defended this dissertation on August 21, 2018.
The members of the supervisory committee were:

Wei Guo

Professor Directing Dissertation

Jorge Piekarewicz

University Representative

William Oates

Committee Member

Kunihiko Taira

Committee Member

The Graduate School has verified and approved the above-named committee members, and certifies
that the dissertation has been approved in accordance with university requirements.

ACKNOWLEDGMENTS

TABLE OF CONTENTS

LIST OF TABLES

LIST OF FIGURES

ABSTRACT

The superfluid phase of helium-4, known as He II, is predominantly used to cool low-temperature devices. It transfers heat by a unique thermally driven counterflow of its two constituents, a classical normal fluid and an inviscid superfluid devoid of entropy. It also has potential use for economical reproduction and study of high Reynolds number turbulent flow due to the extremely small kinematic viscosity and classical characteristics exhibited by mechanically driven flow. A number of diagnostic techniques have been applied in attempts to better understand the complex behavior of this fluid, but one of the most useful, flow visualization, remains challenging because of complex interactions between foreign tracer particles and the normal fluid, superfluid, and a tangle of quantized vortices that represents turbulence in the superfluid. An apparatus has been developed that enables application of flow visualization using particle tracking velocimetry (PTV) in conjunction with second sound attenuation, a mature technique for measuring quantized vortex line density, to both thermal counterflow and mechanically-driven towed-grid turbulence in He II. A thermal counterflow data set covering a wide heat flux range and a number of different fluid temperatures has been analyzed using a new separation scheme for differentiating particles presumably entrained by the normal fluid ("G2") from those trapped on quantized vortices ("G1"). The results show that for lower heat flux, G2 particles move at the normal fluid velocity v_n, but for higher heat flux all particles move at roughly $v_n/2$ ("G3"). Probability density functions (PDFs) for G1 particle velocity v_p are Gaussian curves with tails proportional to $|v_p|^{-3}$, which arise from observation of particles trapped on reconnecting vortices. A probable link between G1 velocity fluctuations and fluctuations of the local vortex line velocity has been established and used to provide experimental estimation of c_2, a parameter related to energy dissipation in He II. Good agreement between the length of observed G2 tracks and a simple model for the mean free path of a particle traveling through the vortex tangle suggests that flow visualization may be an alternative to second sound attenuation for measurement of vortex line density in steady-state counterflow. Preliminary PTV and second sound data in decaying He II towed-grid turbulence shows agreement with theoretical predictions, and enables reliable estimation of an effective kinematic viscosity and calculation of longitudinal and transverse structure functions, from which information about the energy spectrum evolution and intermittency enhancement can be obtained.

CHAPTER 1

INTRODUCTION

H. Kamerlingh Onnes successfully liquefied helium for the first time in 1908, and a short time later used liquid helium to discover superconductivity, the complete loss of electrical resistance in certain substances upon cooling [1]. These discoveries enabled such groundbreaking research technologies as superconducting particle accelerators [2, 3], high field superconducting magnets [4], and orbital infrared telescopes [5]. Researchers in the field of fluid dynamics have also explored the use of cryogenic helium as a medium in which to conduct efficient scale model testing, a task for which it is particularly well suited because of its vanishingly small kinematic viscosity [6, 7]. In both of the above named applications for cryogenic helium—as a coolant and as a test medium—significant advantage can be had by utilizing liquid helium in its superfluid phase: Helium II.

1.1 Helium II

Despite numerous reports of the strange behaviors exhibited by liquid helium when cooled to temperatures below its normal boiling point of approximately 4.2 K, 20 years passed before the formal proposal of the existence of a second liquid phase with unique properties [8]. The so-called λ-transition line, shown in the ^{4}He phase diagram of Fig. 1.1 [9], separates the higher-temperature, classical liquid phase, known as He I, from the lower-temperature, superfluid phase known as He II. Along the saturated liquid-vapor line, the λ-transition temperature is $T_\lambda \approx 2.17$ K. Among the anomalous behaviors of He II are its ability to flow without friction, but also to provide viscous coupling between solid bodies, and its remarkable capability to transport heat [9]. These phenomena are now understood in terms of the two-fluid model and the ability of He II to transport thermal energy by counterflow of the two fluids.

The two-fluid model of Tisza and Landau, in which a superfluid condensate and normal fluid of thermal excitations coexist and are fully miscible [10, 11], provides a phenomenological description for the mechanics of He II. The bulk fluid density is $\rho = \rho_n + \rho_s$, where ρ_n and ρ_s represent the temperature-dependent densities of the normal fluid and superfluid components, respectively. At
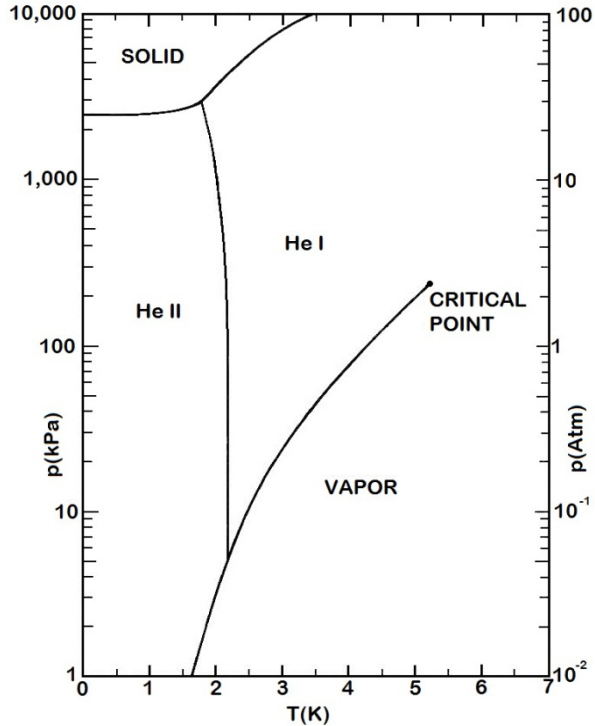
Figure 1.1: Phase diagram for ^{4}He.

T_λ, $\rho_n = \rho$; in other words, He II is comprised entirely of normal fluid at the phase transition temperature. The normal fluid fraction ρ_n/ρ decreases, and the superfluid fraction ρ_s/ρ increases accordingly, as shown in Fig. 1.2 [9], as the fluid temperature is reduced. The composition is almost entirely superfluid below 1 K, and $\rho_s = \rho$ at the absolute zero temperature.

From the definition of the superfluid as a ground-state condensate, it follows that the superfluid component carries no entropy, since entropy depends logarithmically on the number of available states, which in this case is one. The specific entropy s of He II is therefore carried entirely by the normal fluid. Furthermore, the superfluid is inviscid under the two-fluid model. With these properties of the superfluid in mind, simplified equations of motion for He II, including expressions for each of the two fluids, are

$$\frac{\partial \mathbf{v}_n}{\partial t} = -\frac{1}{\rho}\nabla P - \frac{\rho_s}{\rho_n}s\nabla T + \frac{\mu_n}{\rho_n}\nabla^2 \mathbf{v}_n + A_{GM}\rho_s \left|\mathbf{v}_n - \mathbf{v}_s\right|^3 \tag{1.1}$$

2
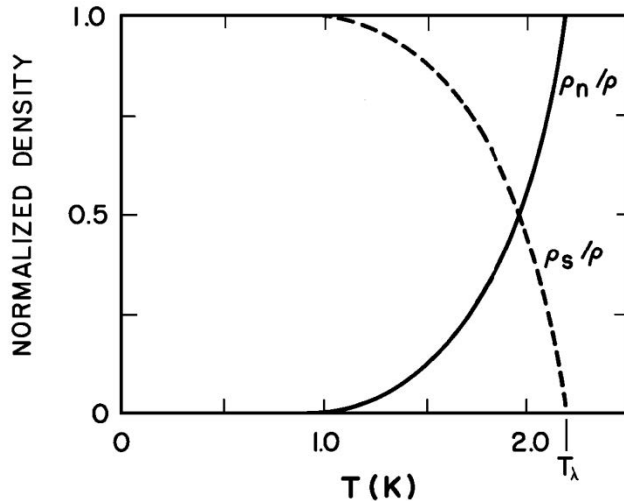
Figure 1.2: Normal fluid and superfluid density fractions as a function of temperature.

for the normal fluid component and

$$\frac{\partial \mathbf{v}_s}{\partial t} = -\frac{1}{\rho}\nabla P + s\nabla T - A_{GM}\rho_n \left| \mathbf{v}_n - \mathbf{v}_s \right|^3 \tag{1.2}$$

for the superfluid [9]. In these expressions, $\mathbf{v}_n$ and $\mathbf{v}_s$ represent the normal fluid and superfluid velocities, respectively, and P and T represent the bulk fluid pressure and temperature. Only Eqn. (1.1) contains a viscous term, with μ_n representing the dynamic viscosity of the normal fluid. The Gorter-Mellink mutual friction coefficient A_{GM}, which appears in both expressions, arises from a unique form of turbulence that appears in the superfluid but affects the behavior of both fluid components.

Lack of viscosity in the superfluid implies that the curl of its velocity field $\nabla \times \mathbf{v}_s = 0$, indicating that the superfluid component is irrotational. It follows that in a rotating container the superfluid should remain stationary, and that the two fluids should be able to flow past each other without friction. However, early experiments showed that the superfluid does exhibit large-scale solid-body rotation [12], and that a kind of mutual friction opposes relative motion of the two fluids [13, 14]. These observations can be explained by the existence of quantized vortex lines [15], topological defects with a core size of approximately $\xi_0 = 0.1$ nm, about which the superfluid rotates with a single quantum of circulation $\kappa = h/m$, where h is Planck's constant and m the mass of a

3

single helium atom. Nearly 30 years after the theoretical proposal of such vortex lines, visual confirmation of their existence was achieved first by photographing electrons [16] and later solidified gas particles [17] captured by the vortices.

The mutual friction force stems from scattering of thermal excitations, or the normal fluid, from quantized vortices [18], and it has also been linked to turbulence in the superfluid component [19]; it follows that turbulence in the superfluid component manifests as quantized vortex lines [20]. Due to the strong influence of quantum effects, namely, quantized vortices and the unique properties of the superfluid, on the macroscopic behavior of He II, turbulence of this kind is generally referred to as quantum turbulence [21].

Perhaps the most common manifestation of quantum turbulence is thermal counterflow, the mechanism by which He II transports thermal energy. In the presence of a heat source, the normal fluid carries entropy away from the source, with velocity $\mathbf{v}_n$, while the superfluid moves toward it, with velocity $\mathbf{v}_s$, such that the overall mass flow is equal to zero [9]:

$$\rho_n \mathbf{v}_n + \rho_s \mathbf{v}_s = 0. \tag{1.3}$$

As per the two-fluid model, these two velocity fields are interpenetrating, and not spatially distinct as in a classical natural convection loop. In a simple one-dimensional case (e.g. counterflow through an insulated channel with a heater at one end), the normal fluid velocity is related to the magnitude of the heat flux, q, as

$$v_n = \frac{q}{\rho s T}. \tag{1.4}$$

The corresponding superfluid velocity is easily obtained from Eqn. (1.3):

$$v_s = -\frac{\rho_n}{\rho_s} v_n. \tag{1.5}$$

As the heat flux increases, the counterflow velocity, $v_{ns} = v_n - v_s$, increases accordingly, and turbulence can develop in both fluid components [22, 23]. Turbulence in the superfluid manifests as a tangle of quantized vortex lines [20], with the line length per unit volume L approximated by

$$L = \gamma^2 \left(v_{ns} - v_0 \right)^2, \tag{1.6}$$

where γ is an experimentally determined temperature dependent parameter [24–29] and v_0 is a small critical counterflow velocity of approximately 2 mm/s [28–30]. Turbulence in the normal

4

fluid behaves classically, excepting its interaction with the vortex tangle through mutual friction. Little is known about this novel form of turbulence, as it was only recently discovered [23].

Despite the complex two-fluid behavior and non-classical nature of the superfluid, experimental observations suggest that mechanically generated turbulent flow in He II behaves similarly to analogous turbulent flow in classical fluids. Classical Kolmogorov energy spectra and decay behavior have been observed for turbulence in the wake of a moving grid [31], between rotating propellers [32, 33], and downstream of a stationary grid installed in a He II forced flow channel [34, 35]. This quasiclassical behavior has been attributed to coupling of the two fluid components due to mutual friction on length scales exceeding the average spacing between quantized vortices [36]; turbulent eddies in the normal fluid component are matched by polarized bundles of vortices in the superfluid [37]. However, not all research supports this picture of quasiclassical turbulence. Recent simulations suggest that eddies in the normal fluid and superfluid may not become locked together [38]. Others point to non-classical features of turbulence in He II, such as temperature-dependent enhancement of intermittency [39], though a recent study of turbulent flow in the wake of a disc indicates that intermittency is not temperature dependent [40]. There is clearly room for improving the general understanding of quasiclassical turbulence in He II.

1.2   Measurement techniques

Two common measurement techniques applied to modern He II research are second sound attenuation and flow visualization. Most investigations make use of one or the other; this work describes only the second apparatus to use both [23]. Second sound attenuation is a mature technique that provides measurement of the average quantized vortex line length in a unit volume of He II. Flow visualization is a powerful tool for high resolution and unobtrusive measurements of flow velocity field, and is relatively new to He II research. Understanding how application of these measurement techniques can answer open questions about quantum and quasiclassical turbulence in He II requires a basic understanding of the techniques themselves.

1.2.1   Second sound attenuation

As a consequence of the two-fluid model, multiple speeds of sound can be obtained for He II. Ordinary sound is the in-phase oscillation of the two fluid component densities, or density waves

in the bulk fluid, and it travels at a characteristic speed c_1, given by

$$c_1^2 = \frac{C_p}{C_v \rho \kappa},$$

(1.7)

where C_p and C_v are the specific heat capacities at constant pressure and constant volume, respectively. Second sound is the out-of-phase oscillation of the component densities while the bulk fluid density remains constant. Since only the normal fluid carries entropy, second sound is associated with the propagation of entropy waves at a characteristic speed c_2, given by

$$c_2^2 = \frac{\rho_s}{\rho_n} \frac{T s^2}{C_v}.$$

(1.8)

The speeds of sound c_1 and c_2 are shown as functions of temperature in Fig. 1.3 [9].

Second sound can be used to determine the average length of quantized vortex lines in a unit volume, or vortex line density L, by measuring the attenuation of a standing second sound wave
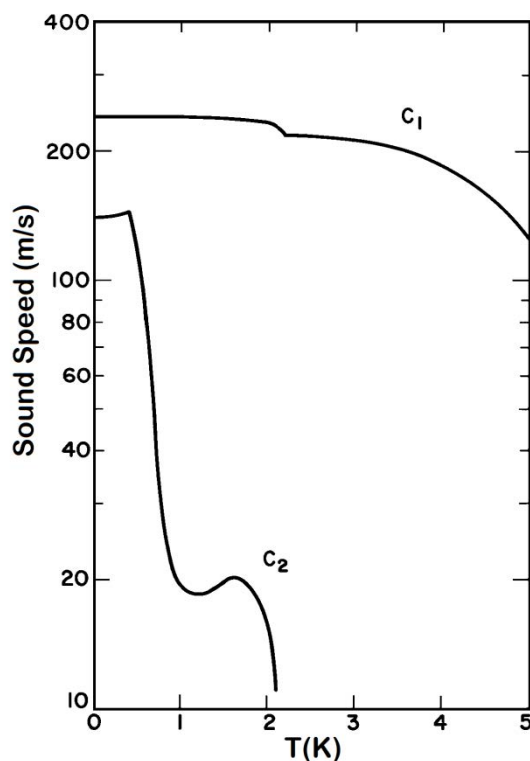
Figure 1.3: Velocity of ordinary and second sound as functions of temperature.

established between two oscillating superleak transducers (OSTs). These are essentially parallel plate capacitors, with one plate and the dielectric formed by stretching a thin gold-coated porous membrane over a metal electrode, which serves as the other plate [41]. Applying an alternating current to the OST causes the membrane to vibrate, but only the normal fluid component transmits the vibrations, since the superfluid is inviscid and can slip through the pores. As a result, oscillation of ρ_n and ρ_s, or a second sound wave, develops in the fluid. Similarly, a second sound wave impinging on an OST membrane causes it to vibrate, inducing a measurable alternating current. If a standing second sound wave is established between two OSTs in a volume containing quantized vortices, the wave will be attenuated by mutual friction, or scattering of the second sound wave from the vortices [18], as illustrated in Fig. 1.4. The line density is obtained by comparing the amplitude A of a Lorentzian resonant peak in the second sound frequency spectrum to its amplitude in the absence of vortices A_0 using the expression [42, 43]

$$L = \frac{6\pi\Delta_0}{B\kappa} \left(\frac{A_0}{A} - 1 \right),$$
(1.9)

where Δ_0 is the full width of the resonant peak at its half-maximum height (FWHM), and B is a temperature dependent mutual friction coefficient [44].

1.2.2 Flow visualization

Flow visualization offers quantitative whole-velocity-field measurements of a fluid in motion. Besides the fluid itself, there are three key components involved: tracer particles, a light source,
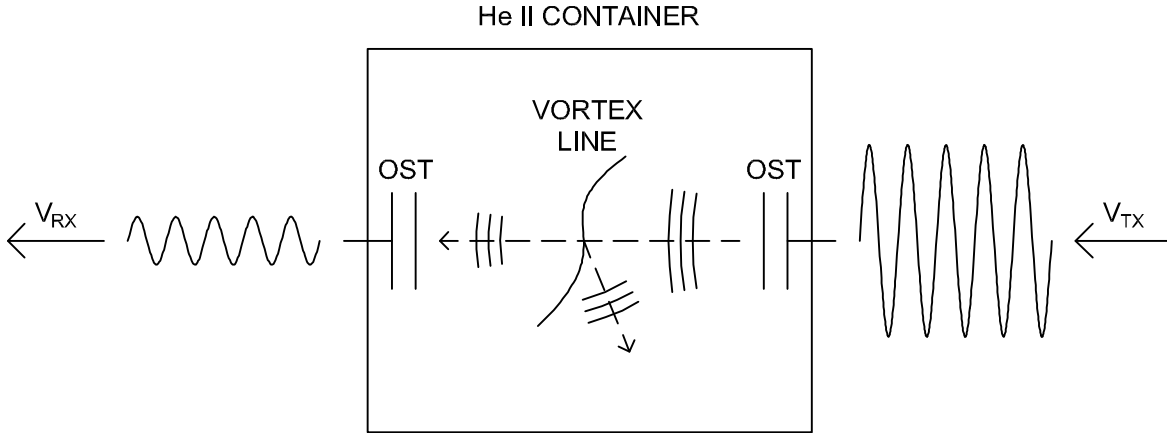
Figure 1.4: Attenuation of a second sound wave due to scattering from quantized vortex lines.

7

and a camera. A homogeneous distribution of foreign tracer particles, whose size and density are such that they passively but faithfully follow the fluid motion [45], is introduced to the fluid by an appropriate seeding procedure. The light source, typically a laser shaped into a thin sheet, illuminates the particles as they move with the fluid through a planar slice of the container. The camera is focused on the illuminated plane, and captures images of the tracer particles at specified times. In the simplest terms, the laser sheet illuminates tracer particles so that the camera can "see" the motion of the fluid. An illustration of a typical flow visualization arrangement is shown in Fig. 1.5.

Flow visualization data are images of the tracer particles, which appear as bright features against a dark background. A computer algorithm measures displacement of the features from
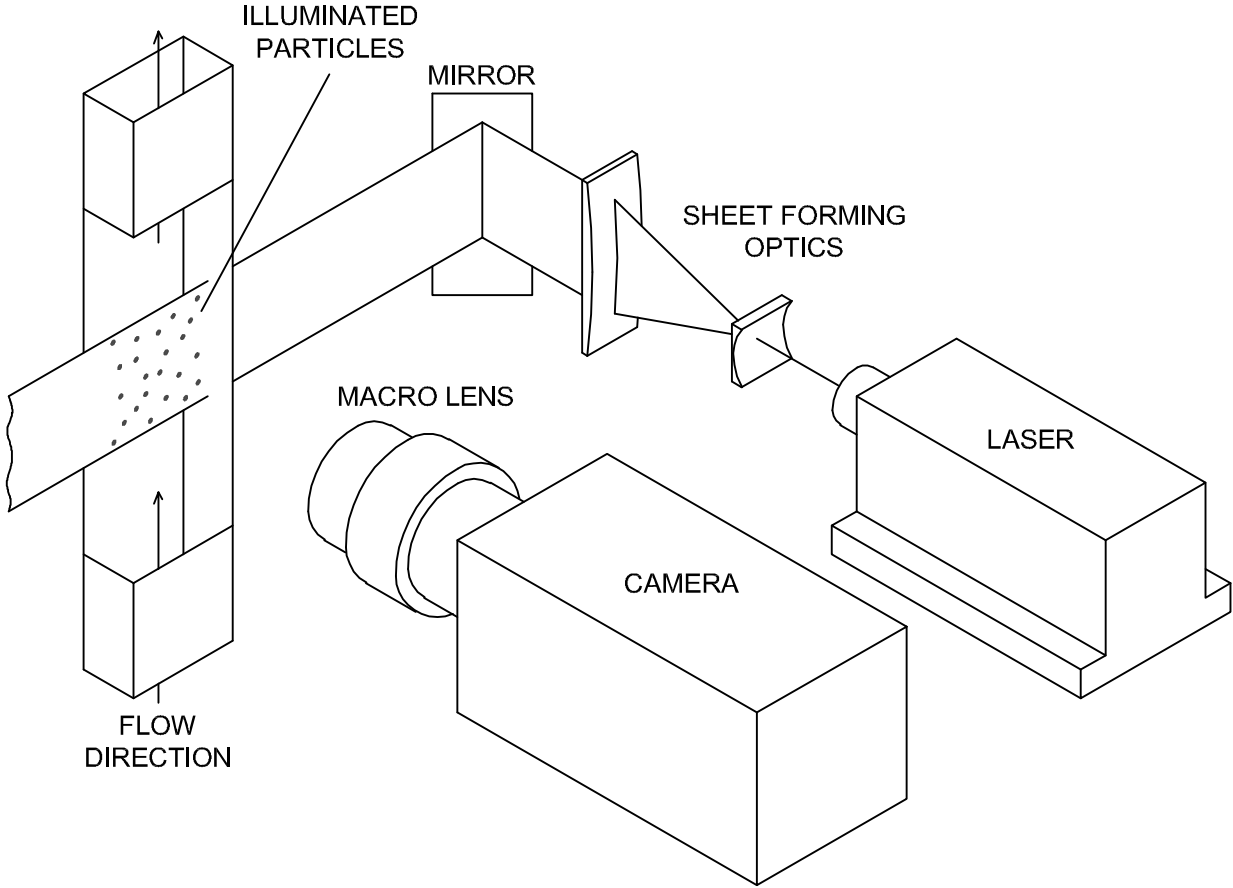
Figure 1.5: Illustration of a typical flow visualization apparatus.

one image to the next, and the local flow velocity is obtained after dividing by the time elapsed between the two images. Multiple methods exist for this procedure. In particle image velocimetry (PIV), the Eulerian approach, two images acquired in rapid succession are divided into segments called interrogation windows. An interrogation window from the first image is cross-correlated with the corresponding window from the second image, and assuming that all of the particles move a similar distance in the same direction, a strong peak occurs in the cross-correlation function that corresponds with the particle displacement. Repeating the process for each interrogation window provides enough local displacement vectors to resolve the velocity field across the entire imaging region. In particle tracking velocimetry (PTV), the Lagrangian approach, a sequence of images with fixed separation time, or a video, is obtained, and the location of each individual particle throughout the sequence of images is determined. Temporal and spatial coordinates for each particle form pathlines, or trajectories, along which the velocity and other kinematic properties for each particle can be calculated.

After nearly two decades of development [46], application of flow visualization to He II remains challenging. In particular, small, neutral density tracer particles with a uniform size distribution do not exist for this low-density ($\rho \approx 145$ kg/m^3), low temperature ($T < 2.17$ K) environment. The almost universally accepted solution is to form micron-sized solidified gas particles by introducing a dilute mixture of hydrogen, or its heavy isotope deuterium, into the liquid helium [47]. If this particle seeding process is successful, the challenge becomes interpretation of the particle motion in He II. In the simplest scenario, particles move with the normal fluid, entrained by the Stokes drag force F_S exerted on the particle,

$$F_S = 3\pi\mu_n d_p \left(v_n - v_p \right), \tag{1.10}$$

where d_p is the particle diameter. If a particle moves close to a vortex line, a trapping force [48]

$$F_T = \frac{\rho_s \kappa^2}{\pi} \ln \left(\frac{d_p}{2\xi_0} \right), \tag{1.11}$$

caused by the Bernoulli pressure gradient surrounding the vortex can potentially trap the particle [17, 49] and cause it follow the motion of the vortex line. However, if relative motion exists between the normal fluid and vortex line, as in thermal counterflow, it will still experience a drag force from the normal fluid and can slide along the vortex [50, 51] or be pulled away if the drag

9

force exceeds the trapping force [48, 52]. With the addition of inertial and added mass effects contributed by the superfluid [53], it is easy to understand why interpretation of this ambiguous particle motion is challenging.

Despite the challenges, PIV and PTV have been successfully applied to study the motion of particles in thermal counterflow [48, 52, 54], as well as to investigate several other practical scenarios, including counterflow [55–57] and forced flow [58] around cylinders, the velocity profile in mechanically driven pipe flow [59], dynamics of quantized vortices [60–62], and flow induced by oscillating grids [63]. More recently, a different approach to He II flow visualization has been introduced, making use of a line of metastable He_2^* molecules as tracer particles [64]. Measurements of the line deformation due to thermal counterflow have lead to non-classical forms of the second order transverse structure function [23], measurement of the effective kinematic viscosity in decaying counterflow turbulence [65], and the energy spectrum in a sustained thermal counterflow [29]. These measurements are free of the ambiguity associated with PIV and PTV since the He_2^* molecules strictly trace the normal fluid for temperatures above about 1 K [64]. However, this approach is not without its limitations: deformation of the line provides information about the flow in only one spatial direction, and since the molecular tracers do not interact with vortices, direct visual measurements of the vortex tangle are not available.

1.3   Motivation

The purpose of this work is to arrive at a deeper understanding of quantum and quasiclassical turbulence through comprehensive measurements using both second sound attenuation and particle tracking velocimetry. Of equal importance is the development of new equipment and advanced visualization techniques to enable such measurements.

A thorough understanding of thermal counterflow turbulence is important for applications of He II as a coolant because turbulence lowers the efficiency of counterflow heat transfer. Even before acknowledgment of superfluidity and the two-fluid model, researchers observed a reduction in apparent thermal conductivity with increasing heat load [8]. For this work, application of PTV will provide information about both the normal fluid component and the quantized vortex tangle, and a new data processing method will remove the particle motion ambiguity. In other words, for the first time, whole-field velocity measurements obtained from particles entrained by the normal

fluid can be identified and analyzed separately from those obtained from particles trapped on vortices, enhancing the utility of PTV for quantum turbulence research applications.

Characterizing quasiclassical turbulence is of vital importance to the potential use of He II as a medium for fundamental and applied high-Reynolds number turbulence research. Since He II exhibits the lowest kinematic viscosity ν of any known substance, less than 10^{-8} m^2/s in the rough temperature range of 1.4–2.0 K [44], the Reynolds number, defined as $Re = DU/\nu$ (where D represents a characteristic length and U a characteristic velocity), for helium flows can be pushed to extremely high values within a compact laboratory apparatus. $Re \sim 10^7$ have already been achieved in liquid helium pipe flow [66] and von Kármán flow, and plans to achieve $Re \sim 10^8$ are in place [33].

While this prospect is attractive in terms of efficiency, implementation still lies in the future because resolution of the somewhat confusing picture of quasiclassical turbulence is beyond the capability of existing experimental apparatus and instrumentation. Traditional probes such as pressure tubes monitor the mixed effects of both fluids, but due to their size they have limited spatial resolution. Furthermore, the invasive nature of such probes can introduce substantial turbulence that is difficult to separate from that generated intentionally, as can other factors such as the boundary layer established by flow past the container walls. Second sound attenuation is certainly useful for its reliable measurement of vortex line density, but it offers no information about the normal fluid. A systematic investigation of simple, well controlled turbulence in both fluid components is an imperative first step towards a deeper understanding of quasiclassical turbulence and the use of He II in high-Re applications.

This work is the first to take that step by applying PTV and second sound attenuation to towed-grid turbulence in He II. Flow in the wake of a towed grid is generally accepted to be homogeneous isotropic turbulence (HIT), a simple form of turbulence that has received extensive theoretical and experimental attention in classical fluids research [67]. Application of PTV will result in high resolution and unobtrusive measurement of the entire two-dimensional flow field in the bulk fluid, and second sound attenuation will provide a measure of the quantized vortex tangle in the superfluid. Careful design of the experimental apparatus and instrumentation ensure that the flow generation and measurement mechanisms work together to generate simple turbulence with the prescribed characteristics so that reliable, comprehensive measurements can be obtained.

Considerable effort was devoted to development of a new facility capable of meeting the strict demands for this experiment. Chapter 2 and Chapter 3 cover the design and operation, respectively, of this facility. Chapter 4 describes results from the first experiments on thermal counterflow, showing that application of the new data analysis technique leads to a deeper understanding of particle motion in thermal counterflow. Chapter 5 demonstrates new applications for PTV enabled by the new analysis method. Experimental confirmation of a link between quantized vortex reconnection and particle velocity statistics, experimental measurement of an important parameter related to energy dissipation, and a new way to measure vortex line density are all covered. In Chapter 6, the comprehensive second sound and PTV data sets from the grid turbulence experiment are represented graphically, accompanied by discussions of how the data can be used for determining effective kinematic viscosity and characterizing evolution of the energy spectrum. Finally, Chapter 7 summarizes the impact of this work and offers suggestions for future work.

CHAPTER 2

EXPERIMENTAL APPARATUS

The apparatus for generating and visualizing thermal counterflow and towed-grid turbulence consists of a vertical flow channel, instrumentation, and grid and pulling system, and resides inside a standard liquid helium cryostat with optical access. In this chapter the design of the flow visualization facility and experimental apparatus will be presented. Fig. 2.1 shows a simple illustration of the vital components for reference.
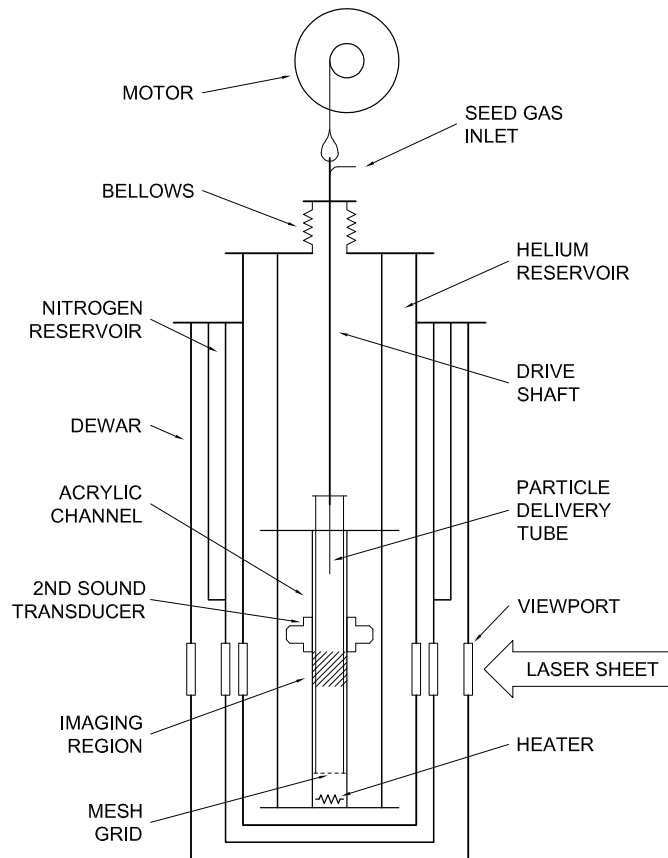
Figure 2.1: Simple illustration of the experimental apparatus (not to scale).

2.1 Flow visualization facility

A photograph of the flow visualization facility developed for the experiment is shown in Fig. 2.2. A helium cryostat with optical access is suspended from a custom made aluminum frame, which provides vibration damping for the cryostat and places the viewports several inches above the surface of an optical table. The laser light source, beam steering optics, and camera for the PTV experiment are all attached to the surface of the table.

Figure 2.2: Photograph of the flow visualization facility.

2.1.1 Optical cryostat

The cryostat consists of a stainless steel helium reservoir inside of a larger vacuum vessel, or dewar. Evacuated space inside the dewar eliminates conduction and convection heat transfer to the liquid helium. Between the helium bath and dewar walls is an annular liquid nitrogen reservoir, which intercepts thermal radiation from the room temperature dewar walls. Both reservoirs are wrapped with several layers of low emissivity aluminized mylar, also referred to as superinsulation or multi-layer insulation, to further reduce radiative heating of the liquid reservoirs.

The helium reservoir is connected to a powerful house vacuum system that provides evaporative cooling for the liquid helium bath. By reducing the vapor pressure from atmospheric down to the vacuum system base pressure of less than 1 Torr, the saturated liquid temperature can be reduced from 4.2 K down to a minimum of about 1.2 K.

Three viewports spaced at 90° intervals in each of the helium reservoir, nitrogen reservoir, and vacuum dewar allow optical access to the liquid helium. Viewports in the helium reservoir are fused silica sealed with indium wire, which is sufficient to prevent the inviscid superfluid from leaking into the vacuum insulation. The original viewport design called for 2 mm indium wires on each side of the glass window, but indium creep caused leaks to open after a few thermal cycles [68]. Eliminating the external indium wire, which does not function as a seal, and replacing it with a thin polytetrafluoroethylene (PTFE) spacer seems to correct the issue. The cryostat can be repeatedly cooled down over a period of at least one year before the indium seals start to leak.

Nitrogen reservoir viewports are heat absorbing glass that transmits visible light but absorbs wavelengths in the infrared spectrum [69]. Heat radiated from the room temperature dewar viewports is absorbed and dissipated into the liquid nitrogen reservoir, preventing it from reaching the helium reservoir without sacrificing optical access. The vacuum space is common on either side of the nitrogen reservoir, so these windows are not sealed.

Viewports in the vacuum dewar are also fused silica, but are sealed by o-rings. A fluoroelastomer such as Viton [70] is recommended over nitrile rubber. It seems that the latter outgasses under vacuum, and deposits of the released substance have been observed on the cold interior viewports, obscuring optical access to the helium reservoir. Care should be taken to avoid excessive clamping force on these viewports, which can cause the glass to break unexpectedly. Allowing the o-rings

to compress under atmospheric pressure during evacuation of the dewar, and then tightening the clamping screws an additional 1/8 turn, is sufficient.

2.1.2 Laser

Laser light sources are preferred for flow visualization since they provide light with high energy density and the beam cross section can be easily manipulated [45]. The light source selected for this work is a continuous wave 473 nm diode pumped solid state laser manufactured by Changchun New Industries Optoelectronics Tech. Co., Ltd. [71]. Its output power is adjustable and peaks at over 600 mW.

The laser beam enters the cryostat through one viewport and exits through the one opposite to minimize heating in the cryogenic environment through absorption of the beam energy. The target profile in the imaging region, or the center of the cryostat, is rectangular with cross section 200 μm thick and at least 9 mm tall. This shape is achieved by a spherical beam expander, followed by a cylindrical expander to generate the rectangular profile and a cylindrical focusing lens to achieve the narrow width, arranged on the optical table as shown in Fig. 2.3.

For a diverging Gaussian laser beam with wavelength λ, the beam radius w as a function of z, the distance from the narrowest point or waist w_0, is given by the expression

$$w\left(z\right) = w_0 \left(1 + \frac{z^2}{z_R^2}\right)^{1/2}. \tag{2.1}$$

The Rayleigh range $z_R = \pi w_0^2/\lambda$, or the distance over which the beam radius remains suitably close to w_0, is defined as $w\left(z_R\right) = \sqrt{2}w_0$. $z_R \approx 66$ mm for a 473 nm laser with 100 μm waist, exceeding the channel width, so the sheet thickness will be relatively uniform across the imaging plane.

The 100 μm waist, or 200 μm sheet thickness, is achieved by passing the beam through a cylindrical focusing lens with focal length $f = 250$ mm just before it enters the cryostat. Considering that w_0 occurs a distance f from the lens, Eqn. (2.1) indicates that the beam radius (or half-thickness, since it will have already obtained a rectangular cross section) should be $w\left(f\right) \approx 0.4$ mm.

The 9 mm sheet height target is based on the 16 mm channel width and 16:9 aspect ratio of the camera (see 2.1.3), and is achieved by a cylindrical beam expander. Placing two lenses such that their focal points coincide results in a magnification $M = |f_2|/|f_1|$, where f_1 is the focal length of the first lens in the expander and f_2 that of the second. For an initially round beam with diameter 0.8 mm, a magnification factor of $M = 11.25$ will achieve the desired 9 mm sheet
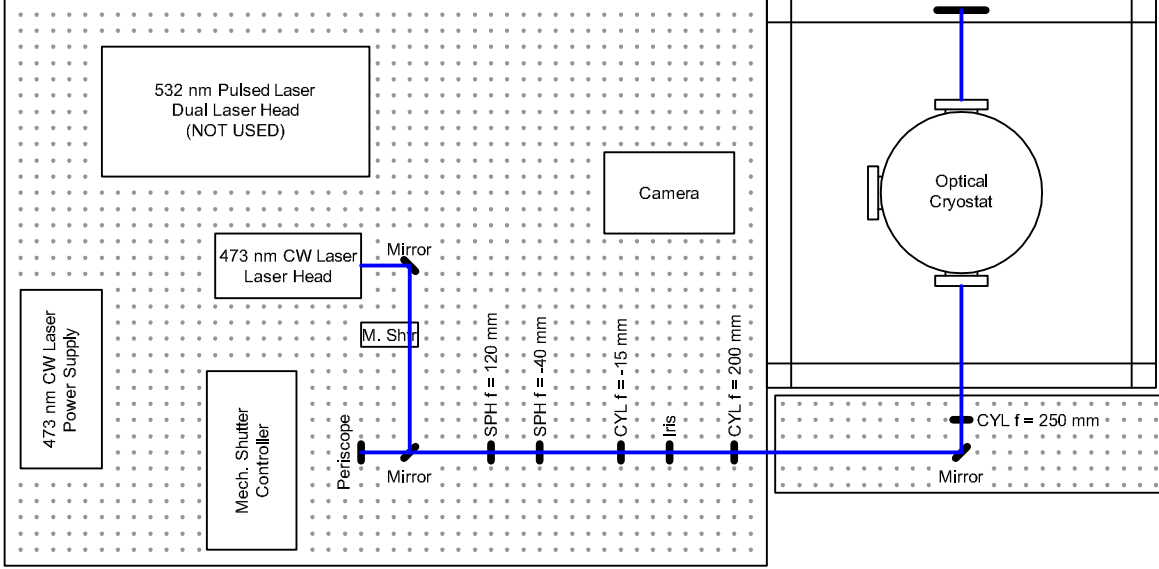
Figure 2.3: Sketch of the laser beam path and optical components.

height. An expander with $f_1 = -15$ mm and $f_2 = 200$ mm is acceptably close. Finally, converting the approximately 2 mm laser beam diameter to 0.8 mm in the first place requires a spherical expander with $M = 0.4$. An expander with $f_1 = 120$ mm and $f_2 = -40$ mm is acceptable. Based on imperfections in lens selection, the resulting laser sheet profile in the imaging region is roughly 224 μm thick and 8.9 mm high, which is reasonably close to the target profile.

A mechanical shutter placed in the beam path allows the laser beam to enter the cryostat only during image acquisition, preventing unnecessary heating of the channel walls. Coordination of the shutter with the camera depends on the image acquisition scheme and will be addressed in Sect. 3.3.2.

2.1.3 Camera

The imaging device is a high-speed complimentary metal-oxide semiconductor camera, X-StreamVISION XS-3 by IDT [72], coupled with a Nikon Micro-Nikkor 105mm f/2.8 lens [73]. It captures images of the illuminated plane through the third cryostat viewport, perpendicular to the laser sheet viewports. The peak image acquisition rate is over 600 fps at the full resolution of 1280×1024 pixels. The number of images acquired in each video sequence is limited by the relatively low onboard memory capacity (1 GB). At the reduced resolution typically used for the

experiment, 1280×720, a maximum of 720 images can be stored in memory before acquisition stops to transmit images to the computer.

Camera operation is made relatively simple by the IDT Motion Studio control software. It acquires images based on an internal trigger, which is configured in Motion Studio, or an external trigger, in which case the acquisition rate and exposure time are interpreted from a series of external trigger pulses as described in Sect. 3.3.2.

2.2   Flow channel and instrumentation

The centerpiece of the experimental apparatus is a vertical flow channel. It is suspended inside the helium reservoir by a custom built support structure consisting of mounting provisions for the channel and a series of radiation shields that prevent radiation exchange between the liquid helium and helium reservoir top plate. The purpose of the channel is to contain the flow under study and to secure instruments that generate and probe the flow. For compatibility with all of the intended experiments, the following criteria were considered when designing the channel:

1. The channel must provide optical access for the visualization experiment.

2. The channel must be free of any geometry that might obstruct the grid motion.

3. The channel must not induce anomalous flow structures that might interfere with the intentionally generated flow.

4. The channel must have attachment provisions for instrumentation (for example, second sound transducers).

Due to its optical transparency and machinability, cast acrylic is the ideal material for a channel that satisfies all of the design criteria. The acrylic flow channel, shown in Fig. 2.4(a), measures 33 cm tall with cross section 1.6 cm square, and is made from four pieces that fit together as shown in Fig. 2.4(b). The pieces are bonded by chemically melting the acrylic with a commercially available solvent welding compound [74]. All mating surfaces are formed by a computer numerical control machine, so that consistency of the channel width and depth depends only on the ability of the machine to cut a straight line. This ensures a uniform square cross section along the entire length of the final assembly, allowing the grid to freely traverse the channel without becoming stuck.
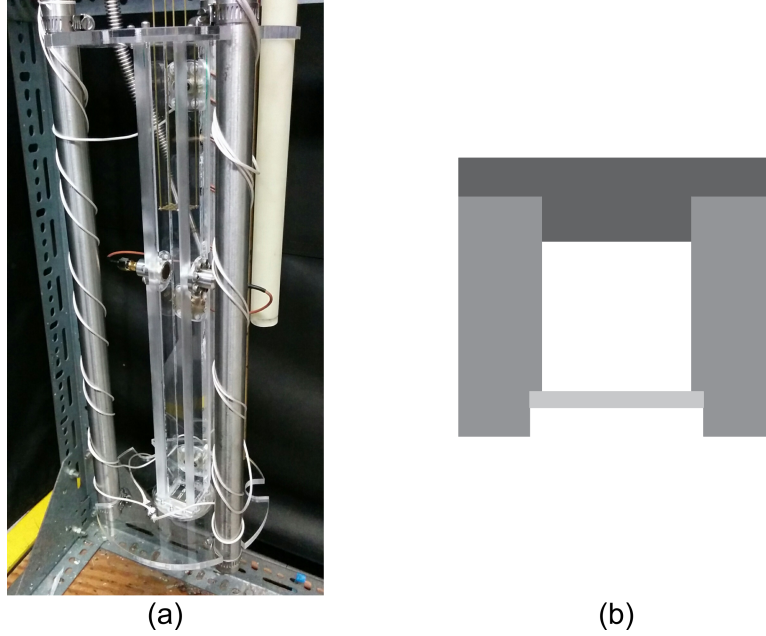
Figure 2.4: (a) Photograph of cast acrylic flow channel and (b) illustration showing how the walls fit together.

The relatively large ratio of length to hydraulic diameter D_h of the channel is intended to reduce interference from entrance and exit effects in the imaging region. The support structure holds the channel so that its geometric center resides at the intersection of the cryostat view ports, and it extends approximately $10D_h$ above and below the windows.

Optical access to the inside of the channel is inherent, eliminating the need for viewports that might introduce a step or recession in the inner walls. Such geometry could potentially snag the grid or induce anomalous flow in the imaging region. To prevent distortion in the image data, a relatively thin piece of acrylic, 1/16 in., is selected for the front wall (through which the camera looks). On the outside of the thicker 3/8 in. back and side walls, several threaded hole patterns facilitate attachment of second sound transducers, temperature sensors, and a resistive heater.

2.2.1 Counterflow heater

The counterflow heater, shown in Fig. 2.5, is the source of flow for thermal counterflow experiments, and also serves as the bottom end of the flow channel. It consists of a stainless steel flange with a square extrusion in the center, on which rests a small circuit board. Four 100 Ω sur-
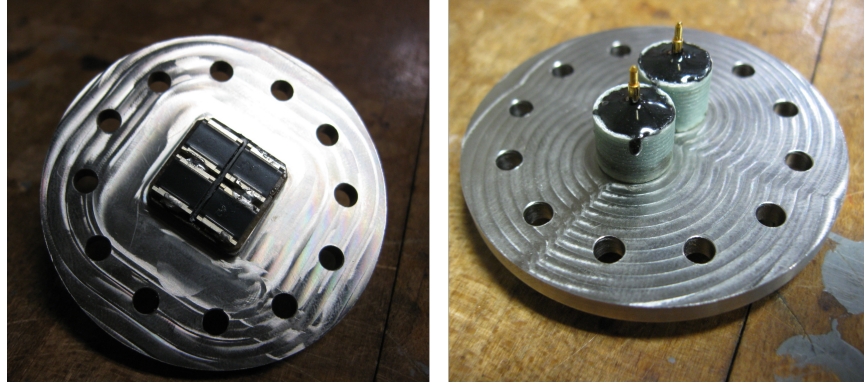
Figure 2.5: Photograph of the (left) top and (right) bottom of the counterflow heater.

face mount resistors arranged in series on the circuit board dissipate heat upon application of an electrical current, generating thermal counterflow. The resistors are evenly spaced across roughly 80% of the bottom of the channel to ensure uniform heating across the channel cross section. Two brass pins protrude through the flange to serve as electrical leads and are sealed by Stycast 2850FT epoxy [75] using a method suitable for preventing leaks at cryogenic temperatures [76].

The heater is sealed to the bottom of the channel by a 1 mm indium wire, which is placed around the square extrusion and crushed against the bottom edge of the channel as the heater mounting screws are tightened. Attachment of the stainless steel flange to the acrylic channel in this manner is cause for concern due to the substantially different thermal expansion coefficients for the two materials. At low temperature the bolt pattern diameter in each material will differ, potentially placing enough stress on the acrylic to break it (the magnitude of this stress is unquantifiable since no data exists on the low temperature properties of this material). To prevent the issue, clearance holes in the flange are oversized and PTFE washers are placed in between the components, with the intention that the parts are free to slide against each other as they cool down. After repeated thermal cycling there is no observable damage to the acrylic.

2.2.2 Temperature sensors

Liquid helium temperature inside the channel is monitored by a pair of Cernox temperature sensors [77]. These penetrate the back wall of the channel, one placed 2.5 cm from the top and the other 2.5 cm from the bottom, but they do not violate the requirement for smooth and uni-

Figure 2.6: Photographs of the (left) sensing side and (right) connector side of the temperature sensor assembly.

form interior channel walls. Dhuley and Van Sciver have developed a method for encapsulating temperature sensors in Stycast 2850FT such that the sensing surface and epoxy form a smooth surface [78]. This method is applied in conjunction with a carefully machined mounting flange that holds the finished surface flush with the interior channel wall. The flange also contains the structure necessary for the epoxy to form an effective seal against leaks through the temperature sensor assembly. Photographs of the assembly are shown in Fig. 2.6.

The same concern raised over bolting together materials with substantially different thermal properties that exists for the heater also exists for the temperature sensor flanges, and the same solution is applied. While the original design also called for an indium seal, the force required to crush the indium wire, distributed over a smaller number of screws, is enough to break the screw threads out of the acrylic. In this case Varnish [77] forms the seal around the temperature sensor flanges in place of indium, and the screws serve only to hold the temperature sensors in place.

2.2.3 Second sound transducers

Measurement of vortex line density in the channel will be accomplished with a pair of oscillating superleak second sound transducers of the kind described in Sect. 1.2.1, placed across from each other on opposite sides of the channel (refer to Fig. 2.1). Design of an OST appropriate for the acrylic channel is non-trivial. Typically, the coated side of the membrane is pressed against the outside of an electrically conductive channel (or against a counterbore in the outer wall, to bring the membrane closer to the inner wall), providing an electrical ground for the transducer. This

is not a viable solution for the acrylic channel for two reasons, the more obvious of which is that acrylic does not conduct electricity. The second is that the membrane surface would be at least partially recessed in the channel wall, violating the criteria for a smooth interior surface.

A novel adaptation of the OST that is fully self-contained and presents a flat sensing surface to the inside of the channel has been developed for compatibility with the new apparatus. The design is represented graphically in Fig. 2.7. It consists of two sub-assemblies: the porous membrane and the base flange. The membrane sub-assembly is formed by placing a piece of polycarbonate membrane with 0.2 μm pores [79] and 500 Å gold coating over a brass electrode, coated side up. An aluminum retaining ring stretches the membrane over the electrode and holds it in place. Due to variability of the membrane thickness and limitations on machining tolerance, finishing of the retaining ring is a trial-and-error process using sandpaper to expand the inside diameter of the ring until it fits tightly over the electrode, but does not tear the membrane. Integrity of the membrane can be confirmed by measuring an open circuit between the electrode and retaining ring with a digital multimeter.

The membrane assembly is attached to the base flange by threading the electrode onto the center
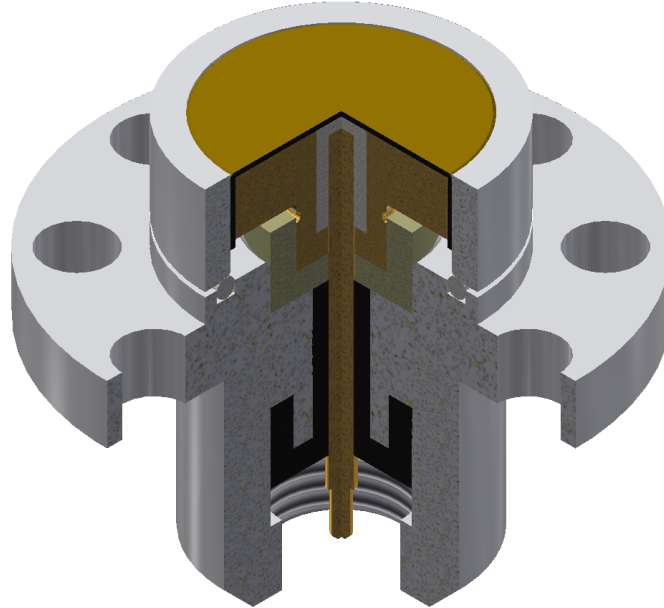
Figure 2.7: Cross section of the custom designed second sound transducers.

pin. Short segments of 1 mm indium wire are pinched between the base flange and retaining ring to provide electrical continuity with the membrane coating. On the back side of the base flange, a built in Sub-Miniature version A coaxial connector allows transmission of the second sound signal by coaxial cable, ensuring that the signal-carrying conductor is fully shielded between the transducer and measurement electronics outside the cryostat. Stycast epoxy serves as the insulating material in the built in connector, and also forms a seal to prevent leakage through the base flange. The fully assembled second sound transducer is attached to the channel using the same system of screws and PTFE washers as the other instrumentation, and Varnish is again applied to the base flange to form the seal.

2.3   Towed grid system

A key component for the grid turbulence experiment is the mesh grid itself and the system that pulls it through the channel. As with all of the other devices that make up this system, the grids and pulling system must be carefully designed. In particular, the grid geometry determines whether turbulence in its wake is truly homogeneous and isotropic, and the pulling system must be able to generate quick but smooth linear motion inside the He II environment.

2.3.1   Mesh grids

Design requirements for the grid, mostly adopted from the literature on classical turbulence, are summarized as follows:

1. The grid solidity must not exceed 40%.

2. The grid must not have a solid or continuous border.

3. The grid must be centered in the channel, with minimal gap between the grid and channel walls.

4. The width of any grid support structures must be smaller than the width of the grid bars.

5. Contact between the grid or support structures and the channel wall must be kept to a minimum.

Grid solidity is the ratio of the solid surface area of the grid to the open area. Fernando and De Silva showed that for a grid oscillating in water, if the solidity exceeds about 40%, the resulting flow will resemble an array of jet flows as opposed to HIT [80].

Fernando and De Silva also showed that if the grid has a solid or continuous border, excessive shear between this border and the channel wall will generate large-scale, inhomogeneous secondary flow around the grid that obstructs the smaller scale (presumably homogeneous isotropic) turbulence generated by the interior mesh [80]. They recommend instead that the grid end halfway through the mesh pattern.

Honey et al. refine the requirements for preventing large-scale flow around the grid by suggesting that the gap between the grid and channel walls be minimized as well as equal on all four sides of the grid [81].

Honey et al. also recommend that elements making up the grid support structure, for example wires by which it is suspended, have smaller width than the grid bars. They imply that turbulence generated by the supports may overshadow HIT produced by the grid itself [81].

The final requirement has been imposed specifically for towed grid turbulence in He II. Dragging the grid or its supports along the channel will produce frictional heating, and the effect will become worse with increasing contact area or contact force. This is problematic in the He II environment since counterflow generated by the frictional heating will be superimposed on HIT generated by the grid.

Three grids with different mesh sizes, $M = 3$, 3.75, and 5 mm, of the design shown in Fig. 2.8 were produced. The solidity for each is 40%, and it can be seen by inspection that the grids end on a half-mesh instead of a solid border. These were manufactured on an abrasive water jet machine by cutting the patterns out of brass sheet stock, the thickness of which (0.025, 0.032, and 0.040 in.) was selected so that the bars have square cross section. Due to the large length-to-width ratio of the channel, contact between the grid and channel is inevitable. To minimize the effect of this contact on the flow field in the imaging region, the corners of the grid, which represent the points farthest from the imaging region, extend slightly (about 0.4 mm) beyond the edges of the mesh. This allows the grid to contact the channel as needed, keeping it roughly in the center, while isolating the contact to the corners. This is desired over contact along the grid edges because it keeps frictional heating as far as possible from the imaging region, and it prevents the metal grid from scratching the acrylic where optical transparency is vital.

The corners of the grid also contain holes for attachment of four 1 mm brass wires that connect the grid to the pulling system. While the diameter of these wires exceeds the width of the bars for
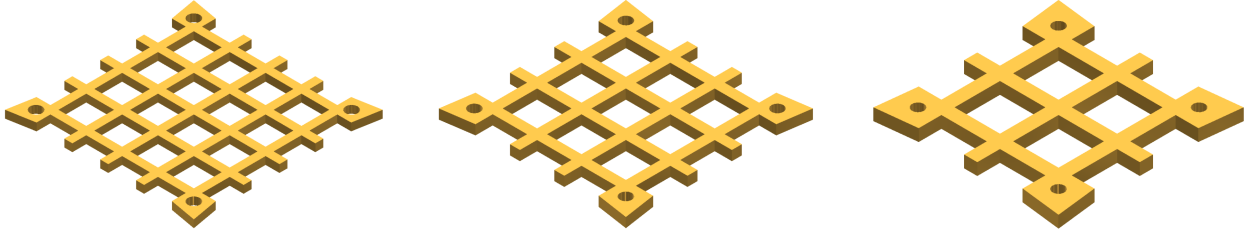
Figure 2.8: Illustrations of the mesh grids with mesh sizes, from left to right, of $M = 3, 3.75$, and 5 mm.

the $M = 3$ mm and $M = 3.75$ mm grids, the compromise is justified by availability of materials and by limitations on the water jet resolution. Suitably straight wires for suspending the grid can be produced from spooled wire by twisting a length of wire around its axis. These wires extend out of the top of the flow channel where they are connected to the main linear drive shaft. The connection is intentionally loose, allowing lateral translation of the grid with respect to the shaft, so that changes in equipment size and position during the cooling down process will not place strain on the grid components.

2.3.2 Towing system

The towing system must generate linear grid motion inside the helium reservoir, with a target constant speed of 100 cm/s, over the 30 cm stroke length. Typically in liquid helium grid turbulence experiments, the motion is generated by an electric motor outside the cryostat. Specifying a motor powerful enough to generate the grid motion is trivial, but transferring that motion from the atmospheric environment to the low temperature, low pressure helium reservoir is particularly challenging. Past apparatus have used a magnetic coupling between an external drive mechanism and internal linear drive shaft [82], or an o-ring seal around a continuous shaft that penetrates the top of the helium reservoir [83]. While effective, both designs offer room for improvement: with the magnetic coupling, the internal drive shaft probably lags behind the external magnet, so it is unlikely that the grid position and speed can be accurately controlled; with the o-ring seal, pulling the grid brings a cold portion of the drive shaft outside of the cryostat, potentially leading to issues with embrittlement, and subsequent leaking, of the seals as well as icing of the drive shaft.

For this apparatus, a 0.5 in. stainless steel tube, serving as the main linear drive shaft, provides a direct mechanical connection to the grid support wires and is sealed to the top of the cryostat by an edge welded metal bellows, which was designed and manufactured specifically for this experiment [84]. The bellows has a 13 in. stroke length, providing a good vacuum seal throughout the full range of motion while isolating the cold portions of the drive shaft from atmospheric conditions. Atmospheric pressure on the bellows provides force for the downward stroke, while a Vectran [85] cord routed over a series of pulleys to a 1.25 in. drum on an electric stepper motor [86] provides force for the upward stroke. The drum is sufficiently wide to prevent the cable from over-wrapping itself, which would effectively change the drum diameter and increase the grid speed. Vectran is a polymer cord chosen for its suitably low stretch (about 0.04% under the load generated by atmospheric pressure on the bellows) and ease of handling when compared with stainless steel cable. A photograph of the bellows and pulling cable system is shown in Fig. 2.9.

Inside the cryostat, three PTFE shaft guides provide low friction alignment of the linear drive

Figure 2.9: Photograph of the top of the cryostat, showing the bellows and a portion of the pulling cable system.

shaft. The first is a sleeve that facilitates motion through the feedthrough on top of the helium reservoir, and also fills the volume inside the bellows. Besides providing alignment for the shaft, this provides support for the bellows core against buckling or squirm during the contraction stroke. Deeper in the cryostat, the other two shaft guides are attached to the radiation shields. Rather than a traditional linear bearing, which is typically a PTFE collar concentric with and surrounding the shaft, these guides make use of four PTFE rods placed parallel to and around the shaft, as illustrated in Fig. 2.10. This not only reduces the contact surface area, but also eliminates potential restriction of shaft movement at low temperature due to thermal contraction of a collar. Instead, the motion is restricted at room temperature, and the shaft moves freely at the operating temperature. Over time, the guides will wear down; if it is not difficult to move the shaft by hand at room temperature, the PTFE rods need to be replaced.

This system has successfully pulled the grid at a range of speeds between 0.1 cm/s and 60 cm/s. Though it is was not tested up to the target maximum velocity of 100 cm/s, it is probably capable of such speed if necessary for future work. Acceleration to full speed is accomplished in the first 3 cm or 10% of the stroke at 60 cm/s. Since the grid acceleration is constant, target velocity is achieved earlier in the stroke for slower speeds. The grid maintains constant velocity until the
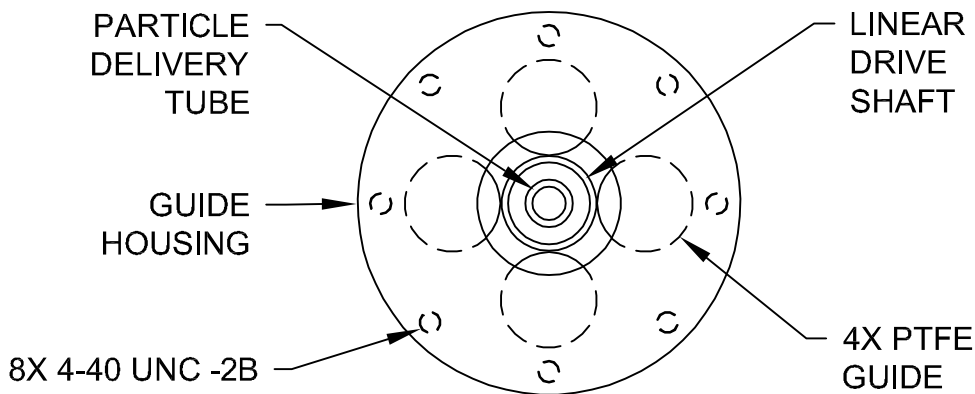
Figure 2.10: Top view of the lower alignment assembly for the linear drive shaft.

deceleration region in the last 3 cm (or less, again depending on grid speed) of the stroke.

An additional component of the pulling system is unrelated to the grid motion. A 0.25 in. stainless steel tube passes through the center of the main linear drive shaft, with one end opening inside the channel, just above the imaging region, when the linear shaft is moved to its lowest position (i.e. the grid is at the bottom of the channel). The other end of the tube is connected to a partial pressure gas blending system outside the cryostat. This is the seed gas delivery tube, which delivers mixed gas to the flow channel to generate tracer particles for the PTV experiment. It is placed inside the drive shaft so that tracer particles can be delivered to the optimal location, but since it moves together with the drive shaft, it will not prevent the grid from traversing the full length of the channel. Details about tracer particles and the blending and delivery system are given in Sect. 3.3.1.

2.4   Chapter summary

A novel experimental apparatus has been developed to enable previously unobtainable measurements of turbulence in He II. Generation of turbulence by either thermal counterflow or a towed mesh grid, and diagnosis by flow visualization or second sound attenuation, is possible due to careful design of the apparatus. Extensive thought was applied to every component, including the vertical flow channel, instrumentation, and towed grid system, to solve the unique design challenges and produce a state of the art experimental facility. Most of the contents of this chapter have been peer-reviewed and appear in the Review of Scientific Instruments [87].

CHAPTER 3

OPERATIONAL PROTOCOL

Flow can be generated either with the counterflow heater or towed grid system, and probed by either second sound attenuation or flow visualization. It is not advisable to attempt flow visualization and second sound attenuation simultaneously, as it is not clear how the presence of tracer particles might affect the attenuation of second sound. Protocols for the two experimental techniques will be presented separately, following a discussion of the method for cooling down the cryostat.

3.1   Cooling-down phase

The cryostat is prepared for cooling down by first evacuating the dewar with a turbomolecular pump for approximately one week, lowering the vacuum insulation pressure to about 10^{-6} Torr. Contaminants are then removed from the helium reservoir by evacuating it with the house vacuum and refilling it with helium gas. This flushing procedure is typically performed three times, and each time the reservoir is refilled through the tracer particle delivery tube to flush any contaminants out of the tube, preventing blockages at cryogenic temperatures. The cryostat is then pre-cooled by slowly filling the nitrogen reservoir with liquid nitrogen until it is expelled from the open vent. Refilling is required at least daily. As helium gas gives up heat to the liquid nitrogen, the helium reservoir temperature and pressure will fall.

Temperature and pressure in the helium reservoir are monitored by a Lake Shore silicon diode and an MKS [88] 650 series pressure control system, respectively. The block diagram of Fig. 3.1 shows how these instruments interface with a computer that serves as the control center for the experiment. A 10 μA constant current source (CCS) generates a temperature-dependent voltage across the silicon diode, which is measured through a National Instruments [89] PCIe-6341 multi-function I/O device. The diode is accurate to ± 0.5 K from room temperature to liquid helium temperatures, providing a reliable monitor for the helium reservoir temperature throughout the cool-down procedure. Note that the Cernox sensors installed in the channel (discussed in Sect. 2.2.2) are only accurate at liquid helium temperatures.
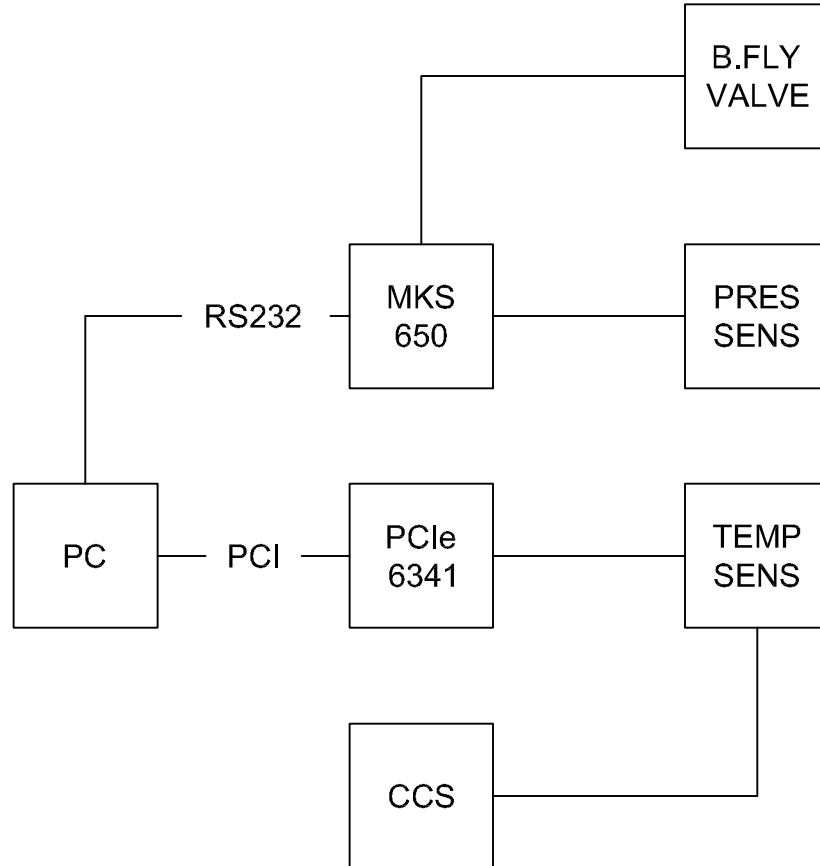
Figure 3.1: Block diagram of the instruments used to control the helium reservoir temperature and pressure.

The MKS pressure control system monitors helium reservoir absolute pressure with a capacitance manometer, and adjusts an electronic butterfly valve in the house vacuum plumbing to control vapor pressure, and by extension, liquid helium bath temperature. Configuration commands are sent from the PC serial port but the pressure control system is otherwise self-contained. During the cool-down process, it serves only as a helium reservoir pressure monitor.

Pre-cooling will bring the helium reservoir temperature down to about 230 K after several days, and the reservoir pressure will be slightly less than atmospheric. At this point the reservoir can be re-pressurized from a compressed gas cylinder, and then cold helium gas followed by liquid helium can be siphoned from a transport dewar into the cryostat. When the liquid level reaches no more than 30–31 in., the siphon is removed and the liquid helium is evaporatively cooled. Once

the Cernox temperature sensors indicate the desired He II temperature, the MKS pressure control system is engaged to control the pumping rate so that the corresponding saturated vapor pressure is maintained. Flow generation and measurement commences once the fluid temperature is stabilized.

3.2   Second sound attenuation

The system used to measure second sound attenuation is shown schematically in Fig. 3.2. The signal can be thought to travel clockwise through the network. It begins with the sinusoidal output of the Stanford Research Systems (SRS) [90] DS345 Function Generator, which is converted to a second sound wave by the transmitting OST. The attenuated wave is converted back into an electrical signal by the receiving transducer. Due to poor efficiency inherent to the OST, the received signal magnitude V_{RX} is several orders of magnitude smaller than the transmitted signal magnitude V_{TX} [91], and typically buried in environmental noise. A lock-in amplifier can be used to pick out the receiver signal component at the transmitter frequency f_{TX} and generate a direct current (DC) output signal R proportional to V_{RX}. An SR810 Lock-In Amplifier is used for this purpose. Preceding it with an SR560 Low Noise Preamplifier improves the signal-to-noise ratio of the output signal. Finally, two high voltage power supplies provide a DC bias to flatten the membranes and improve sensitivity [41]. 10 MΩ resistors prevent excessive current draw from the DC power supplies should a short circuit develop in the network, and 220 nF capacitors isolate electronic equipment from the bias voltage.

This system should be calibrated at each temperature to optimize second sound transducer performance, and it can then be used for both steady-state and transient VLD measurements, though the approach to each is slightly different.

3.2.1   Calibration

Optimal settings for the DC power supplies and function generator are selected using an adaptation of the method described by Stalp [42]. To illustrate the calibration process, this section walks through the calibration procedure carried out at 1.65 K. The fluid was stagnant, and since the mesh grid was installed, it was parked at the top of the channel to prevent interference from the support wires. First the DC bias voltage was increased from 10 V to 190 V, the maximum safe voltage based on the coaxial cable rating, in steps of 10 V while the alternating current (AC) component
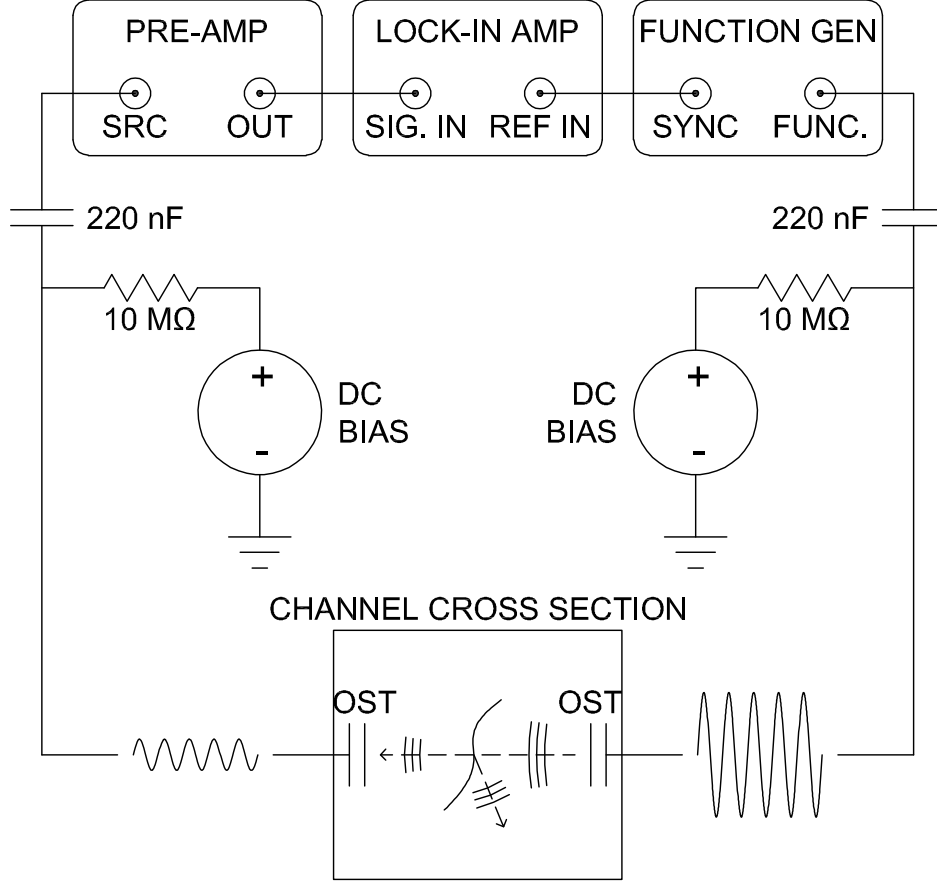
Figure 3.2: Schematic representation of the second sound measurement system.

was held at a fixed frequency and amplitude. For each DC voltage step, R was sampled several times. The mean and standard deviation measured for each step are shown in Fig. 3.3(a) (error bars represent standard deviation multiplied by 100). Beyond about 170 V the signal amplitude ceased to increase with bias voltage, so 170 V was selected for the DC bias.

Similarly, the AC component, V_{TX}, was increased from 1 V_{pp} to 10 V_{pp}, the upper limit of the function generator output, in steps of 1 V while f_{TX} and the DC bias were held constant. Fig. 3.3(b) shows that R increases linearly with V_{TX}, but the signal-to-noise ratio, defined here as the ratio of mean signal value to standard deviation, increased when V_{TX} exceeded about 8 V_{pp}. Therefore 8 V_{pp} was selected for the AC excitation amplitude.

To determine the mean vortex line length per unit volume L in the channel, a suitable peak
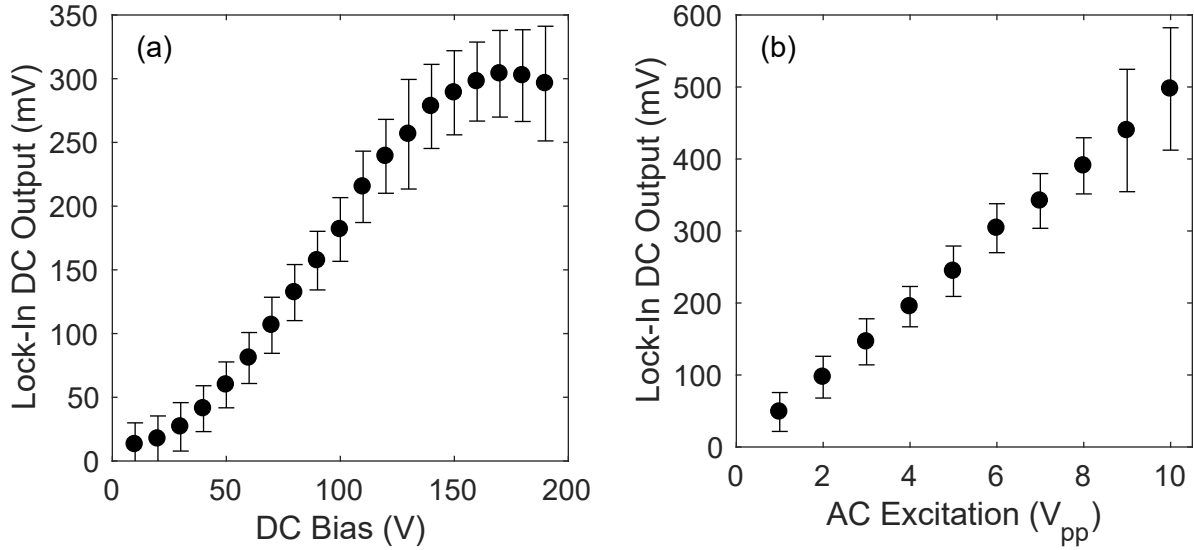
Figure 3.3: Lock-in DC output R as a function of (a) DC bias and (b) AC excitation amplitude.

from the second sound resonant frequency spectrum must be selected and characterized. Recall from Sect. 1.2.1 that the peak height A when vortices are present is compared to the unattenuated height A_0 and FWHM Δ_0 of the peak when the fluid is quiescent using Eqn. (1.9):

$$L = \frac{6\pi\Delta_0}{B\kappa}\left(\frac{A_0}{A} - 1\right).$$

The spectrum at 1.65 K was measured by recording the value of R while stepping f_{TX} from 10–30 kHz in 2 Hz increments, resulting in the spectrum shown in Fig. 3.4. Strong Lorentzian peaks are expected to occur at the resonant frequencies f_r of the channel, which should occur approximately every 643 Hz according to the relationship

$$f_r = \frac{nc_2}{2d}, \tag{3.1}$$

where n represents the nth harmonic, c_2 the second sound velocity, and d the width of the channel (note that thermal contraction of the channel has been taken into account for this calculation). In the measured spectrum, a resonant peak can be observed every 642 Hz on average, in excellent agreement with the prediction.

The 33rd harmonic was selected for characterization at 1.65 K due to its large amplitude, symmetry at the peak, and lack of fine structure. Averaging 20 scans over a frequency range of
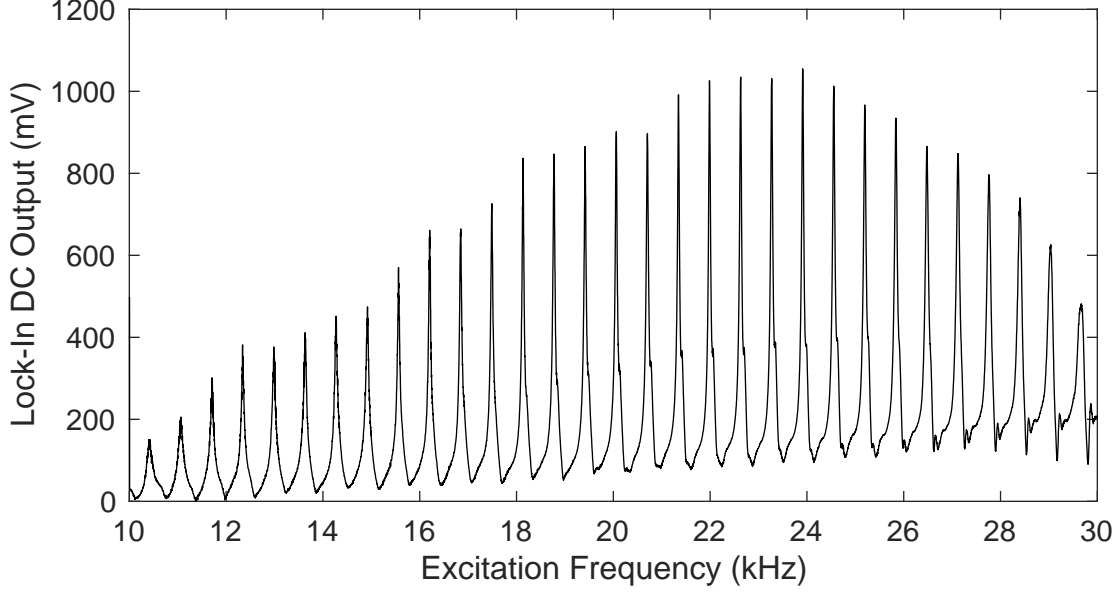
Figure 3.4: Second sound frequency spectrum at 1.65 K.

21.0–21.6 kHz in steps of 2 Hz produced the resonant peak shown in Fig. 3.5. A Lorentzian curve, shown by the black line, fits the measured peak remarkably well. The center frequency and peak voltage are 21.346 kHz and 992 mV, respectively, and the FWHM of the Lorentzian is 59.5 Hz. Note that the secondary structure in the right-hand tail was considered a non-issue since it occurs below the half maximum height of the Lorentzian, and was therefore omitted from the fit and otherwise ignored.

Ideally, f_{TX} could be fixed to $f_r = 21.346$ kHz, and R continuously measured to produce $A(t)$ and convert to $L(t)$ using Eqn. (1.9), producing the time-dependent vortex line density for any number of different flow scenarios. While this method has been used successfully for decaying grid turbulence in the past [42], it is not reliable since the resonant frequency changes with random fluctuations of the fluid temperature. Holding f_{TX} constant while the resonant frequency peak location shifts unpredictably will result in artificial attenuation. A couple of solutions have been devised to work around this temperature stability issue. One consists of a calibration to associate the measured signal, regardless of its relationship to the resonant frequency, with a predetermined peak height [92]. Another uses a closed loop feedback system that oscillates at the channel resonant frequency, whatever it happens to be at any given time, to excite the transmitting OST [93]. For

34
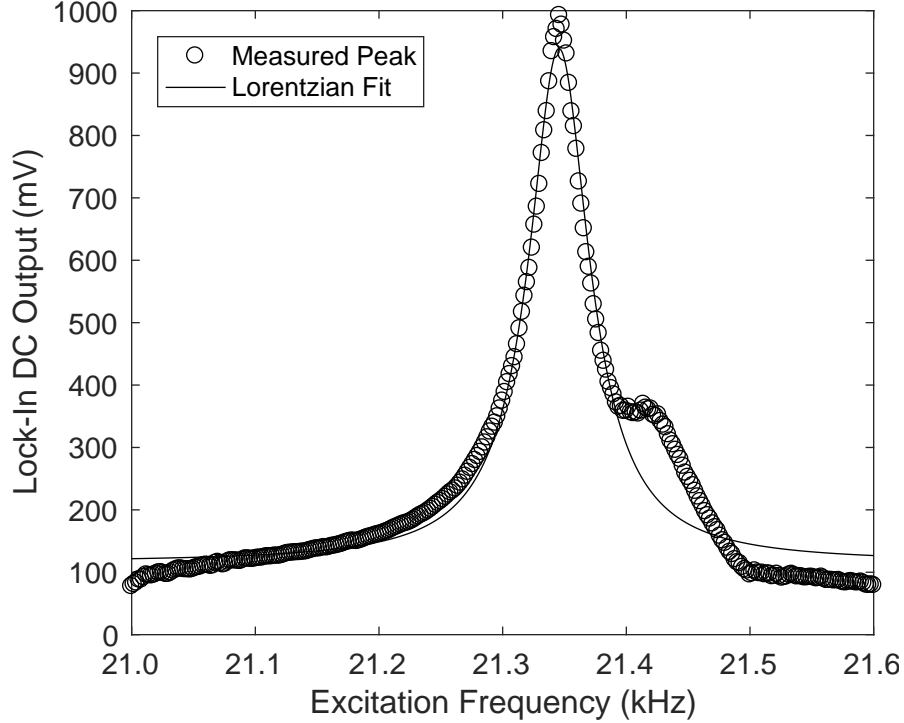
Figure 3.5: 33$^{\text{rd}}$ second sound harmonic at 1.65 K.

this work, the solution involves repeated scans of the resonant peak, ensuring that the peak is captured on each scan. Time resolution is sacrificed, but not to an extent that will affect the experimental results.

3.2.2 Steady-state measurement

For steady flow measurements, such as acquisition of an unattenuated peak in quiescent fluid or measurement of vortex line density in steady-state counterflow, there is no time limitation for the peak measurement. The entire resonant peak can be acquired by changing f_{TX} in small steps and recording R at each step. Typically, when applying this frequency step method, the step size is 2 Hz, the system dwells at each step for 25 ms, and each peak is acquired 50 times. Mean unattenuated peak height A_0 can be obtained by averaging the heights of peaks acquired while the fluid is stagnant. Note that this is the average of the peak heights, not the height of the averaged peaks; the latter has no meaning since peak shifts in the frequency domain will effectively smooth over the sharp peaks. Similarly, mean FWHM can be obtained by interpolation of the frequency

at the FWHM for each peak. The attenuated peak height A is obtained in the same manner after steady flow has been established.

3.2.3 Transient measurement

Transient flow, such as turbulence in the wake of the grid, may change drastically in the time required to step over a resonant peak, so the frequency step method is inappropriate. Instead, a sweep method that takes advantage of the DS345 Function Generator capability to sweep the output signal over a specified frequency range is used for transient flow. Continuing the example at 1.65 K from Sect. 3.2.1, f_{TX} was configured to sweep linearly from 21.334–21.358 kHz over a period of 50 ms. At the end of the sweep, it instantly begins again from 21.334 kHz. As long as the resonant frequency does not fluctuate outside of the 25 Hz window, the peak will be captured and the correct height can be determined. This limits the time resolution to the sweep period of 50 ms, but there are no anticipated features of the VLD decay curve that require higher resolution.

An example of the raw data stream resulting from application of the frequency sweep method to towed grid turbulence is shown in Fig. 3.6. The lock-in output R was recorded for 61 s beginning just before the mesh grid motion was initiated (note that in a typical experiment the measurement time is longer). Fig. 3.6(a) shows the overall data stream. A clear minimum occurs at the beginning, when the grid passes between the second sound transducers. The signal magnitude then appears to increase smoothly while the vortex tangle decays. On closer inspection, Fig. 3.6(b), the sequence of small peaks that results from the frequency sweep method can be clearly observed. It is the maximum value of each of these peaks that can be used to determine vortex line density within each 50 ms time interval.

A time resolved series of the resonant frequency peak height $A(t)$ can be formed by locating the global minimum and subsequent local maxima in the raw data stream. The global minimum occurs when the grid passes between the second sound transducers, almost completely obstructing propagation of the second sound wave. This point is taken as the time origin, $t = 0$. For each subsequent local maximum, the time elapsed from $t = 0$ is determined, and the magnitude is sorted into a discretized array representing $A(t)$ where each index corresponds to a 50 ms time window. For example, if a peak occurs 0–50 ms after $t = 0$, its magnitude is stored as the first element in the array. Conversion of $A(t)$ to $L(t)$ is then accomplished with Eqn. (1.9) as usual. Due to unpredictable shifts of the unattenuated peak height over long periods of time, A_0 is computed for
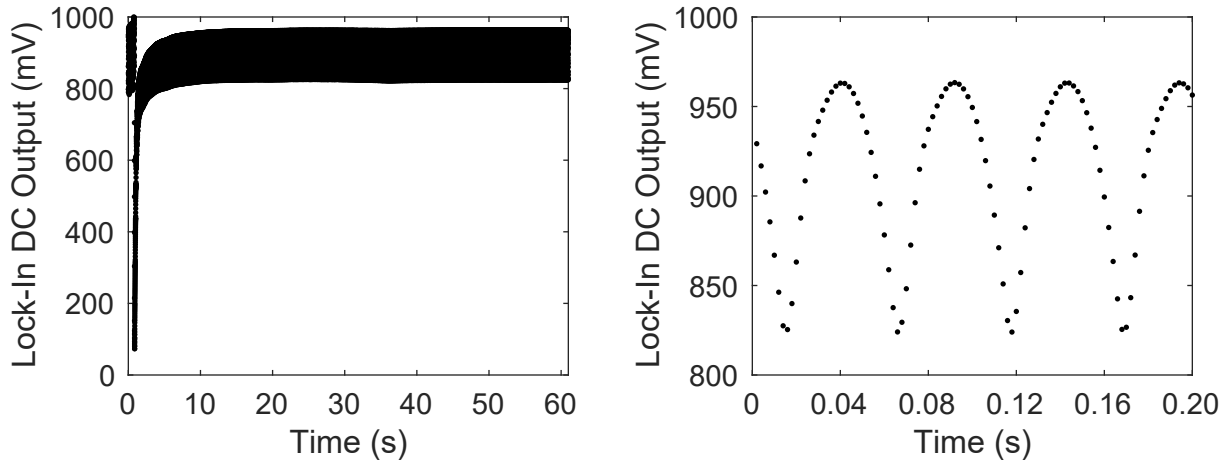
Figure 3.6: (a) General and (b) fine structure of the second sound data stream.

each acquisition by averaging the peak height in the last 10 s of the data stream. A suitably large number of decay curves for each point in the parameter space, typically 20, can then be averaged to generate a curve representing the mean vortex line density as a function of time.

3.3 Particle tracking velocimetry

Probably the most common flow visualization technique is particle image velocimetry (PIV), an Eulerian approach that has been used extensively for classical fluids and was first applied to He II by Zhang and Van Sciver [54]. A pair of images separated by a known time interval dt are segmented into interrogation windows, which are cross-correlated. Assuming that the images depict a single smoothly varying velocity field, the cross-correlation function for each interrogation window will exhibit a strong peak corresponding with the local mean particle displacement $d\mathbf{x}$ [45]. Local velocity vectors for each window are obtained from $d\mathbf{x}/dt$, producing the velocity field in the imaging region.

In He II, the images do not depict a single smoothly varying velocity field. Particles are either entrained by the normal fluid or trapped on quantized vortices, and the behavior of particles in each group can be significantly different. A more appropriate technique is particle tracking velocimetry (PTV), a Lagrangian approach that was first applied to He II by Paoletti et al. [52]. Locations $\mathbf{x}$ of individual tracer particles are tracked throughout a video, or sequence of images acquired with

a consistent separation interval dt, to form trajectories for each particle. This approach is more reliable for He II since spatial averaging of the trajectories is not required to obtain the velocity measurement. However, practical application of PTV to He II presents significant challenges, including seeding of the flow field with suitable tracer particles, generating flow under carefully controlled conditions, and extracting quantitative information from the image data.

3.3.1 Tracer particle generation

Solidified deuterium tracer particles are employed for this work. They are formed presumably by deposition when the seed gas, comprised of deuterium gas diluted with helium, is delivered directly into the He II-filled channel via the delivery tube. Seed gas is prepared using the partial pressure blending system shown in Fig. 3.7. The process begins with the linear drive shaft fully lowered, which places the delivery tube inside the channel, and with all of the blending system valves open, to evacuate the system.
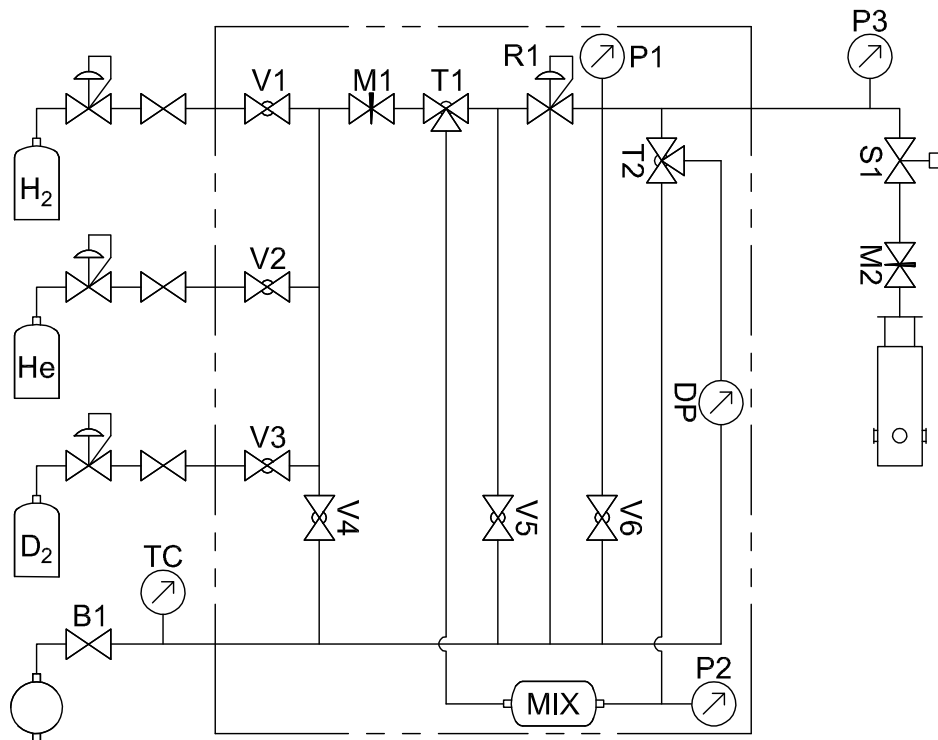
Figure 3.7: Partial pressure blending system used to create tracer particle seed gas.

First the injector solenoid S1 is closed and the flow control valve M2 is adjusted to one full turn open. Compressed gas cylinders are opened after the gas inlet valves V1, V2, and V3 are closed. The inlet manifold, mixed gas storage cylinders, and seed gas delivery line are then isolated from the vacuum manifold by closing valves V4, V5, and V6, respectively; the metering valve M1 is adjusted fully clockwise; and the storage cylinders are connected to the inlet manifold by turning the three-way valve T1 to the "Fill" position.

The inlet manifold is first filled with D_2 by opening V3 and M1 is slowly opened until the desired D_2 partial pressure is obtained in the storage cylinders. Storage cylinder absolute pressure can be measured with the electronic differential pressure sensor DP by turning T2 to the "Tanks" position. When the desired partial pressure is obtained, the D_2 supply is isolated from the inlet manifold by closing V3, and the manifold is purged by briefly connecting it to the vacuum manifold through V4. This process is repeated for the He gas until the desired D_2 concentration is achieved. Since the mixture can be treated as ideal, D_2 concentration is the ratio of D_2 partial pressure to mixture total pressure. Table 3.1 lists concentrations that work for for a number of He II temperatures.

Mixed gas is transferred to the injector solenoid by turning T1 to the "Experiment" position and turning the knob on the storage cylinder regulator R1 clockwise until the downstream pressure gage P3 indicates about 600 mbar (absolute). Then gas can be delivered to the cryostat by opening the injector solenoid. Typically the valve is opened for 30 s, closed for about one minute, and then opened again for 30 s. After 10–30 minutes a cloud of small tracer particles should appear in the imaging region of the channel, and flow generation and image acquisition can begin.

Particles usually linger for only one acquisition cycle in the grid turbulence experiment, and two or three in the counterflow experiment. New particles must be formed periodically by returning the linear drive shaft to the fully lowered position, opening V4, V5, and V6 to purge the blending system, and then repeating the seeding process.

Size of the particles formed using this method can be determined by measuring their terminal velocity v_{slip}, obtained by applying the particle tracking algorithm (discussed in Sect. 3.3.3) to

Table 3.1: Suggested D_2 concentration for seed gas used at several He II temperatures.

Temperature (K)	1.65	1.70	1.85	1.95	2.00	2.12
Concentration (%)	13	13	5	10	9	1

settling particles in quiescent He II [48, 94]. The terminal velocity is related to particle size d_p according to the expression obtained by balancing the Stokes drag force acting on the particle with its weight in liquid helium:

$$v_{slip} = \frac{g\left(\rho - \rho_p\right)d_p}{18\mu_n}.$$ (3.2)

Here μ_n is the normal fluid dynamic viscosity, ρ_p is the density of the particle, and g is acceleration due to gravity. Eqn. (3.2) can be rearranged to give the particle size as a function of the measured terminal velocity:

$$d_p = \sqrt{\frac{18\mu_n v_{slip}}{g\left(\rho - \rho_p\right)}}.$$ (3.3)

Using this method, v_{slip} is typically measured in the range of 4–5 μm. As an example, in one typical case the slip velocity was -0.42±0.25 mm/s, and the corresponding particle size, shown in Fig. 3.8, was calculated as 4.6±1.3 μm.

This essentially sets the resolution for the visualization experiment, as the particle size represents the smallest length scale that can be resolved [95]. Since the inter-vortex spacing should be of the order 10 μm or greater (for both counterflow and grid turbulence measurements), these particles are suitable for probing length scales both above and below the mean line spacing.
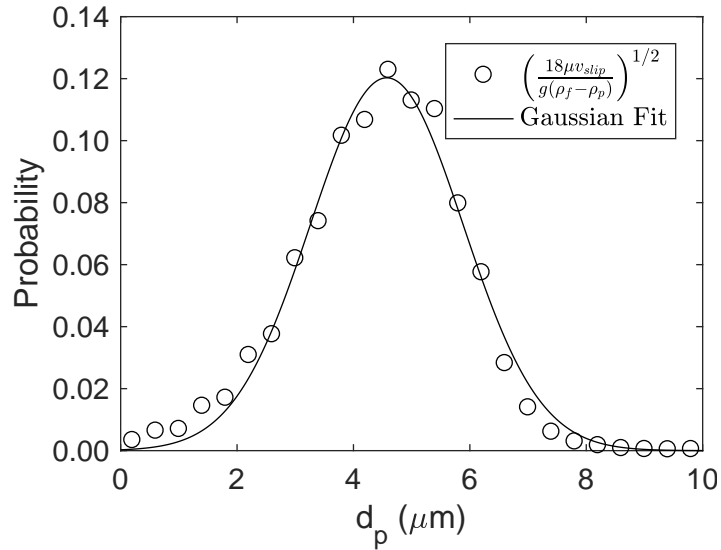
Figure 3.8: Probability density function for solidified tracer particle size.

3.3.2 Flow generation and image acquisition

The facility is designed to accommodate visualization of both thermal counterflow and towed-grid turbulence. The protocol for coordinating flow generation and image acquisition depends on which type of flow will be investigated.

Counterflow. PTV could conceivably be applied to study either steady-state counterflow, in which the heat current is sustained, or transient counterflow, in which the heat current changes over time (e.g. decaying counterflow, where the heater is suddenly turned off). The scope of this work is limited to visualization of steady-state counterflow, so coordination of the heater and image acquisition system is relatively simple. A block diagram of the instruments involved is shown in Fig. 3.9.

The camera is configured for an internal trigger, and the acquisition rate and exposure time are configured within Motion Studio. The mechanical shutter is triggered by the synchronization output pulse from the camera, which is active each time the camera acquires an image. Configuring
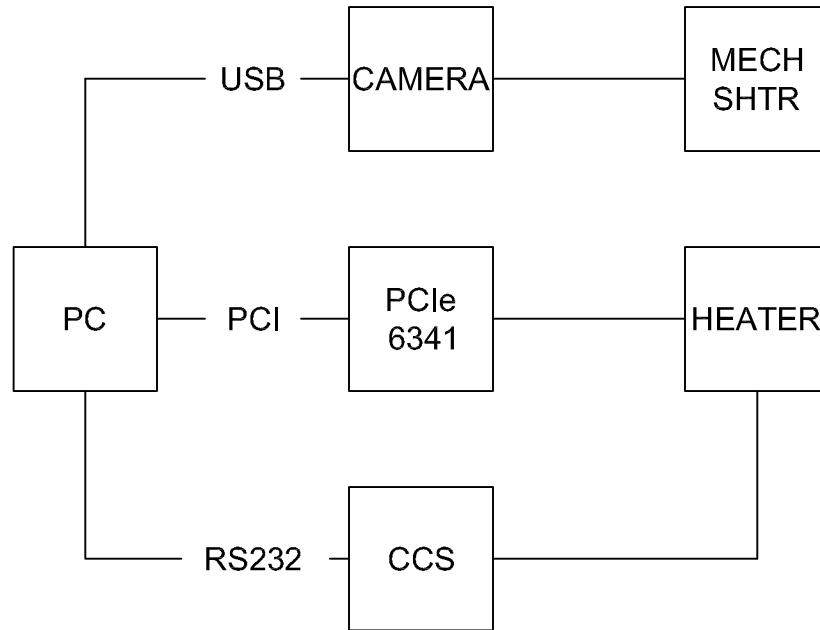
Figure 3.9: Block diagram of the instruments used to control the counterflow visualization experiment.

the shutter to remain open for a period of time exceeding the image acquisition period ensures that it will remain open throughout the acquisition.

A constant current I applied to the resistive heater (see Sect. 2.2.1) generates a steady heat flux q, the magnitude of which is obtained by measuring the voltage drop V across the heater using the multi-function I/O device:

$$q = \frac{VI}{d^2},$$

(3.4)

where $d \approx 1.6$ cm is the channel side length. After waiting several seconds for the counterflow to become fully established (at least 20 s is recommended [23]), image acquisition is triggered manually in Motion Studio and the camera records video until the onboard memory is full. The sequence is then transmitted to the computer, and additional video can be recorded as long as particles remain in the channel.

Grid turbulence. Towed grid turbulence is transient by nature, with the turbulent energy beginning to decay immediately after the grid is pulled. Existing measurements of decaying grid turbulence using second sound attenuation monitor vortex line density for several tens of seconds after pulling the grid [31]. A similar decay period, perhaps 40 s, should be a suitable target for the PTV measurement. Based on the limited camera memory, a continuous acquisition for 40 s limits the frame rate to 18 fps, which is far from acceptable.

An efficient compromise is to record bursts of images at a higher frame rate at specified times throughout the decay period. 20 short videos consisting of 34 images each are recorded at 120 fps. They cover time windows $t = n \pm 0.142$ s, where $n = 0, 2, 4, \ldots, 38$ and $t = 0$ is the time that the grid passes the geometric center of the channel.

The purpose of the first video centered at $t = 0$ is to calibrate the timing. Ideally, the grid should cross the center of the channel halfway through the video, but slight timing errors are inevitable. By observing the grid position in this video, the correct time origin can be established, and any necessary timing correction can be applied to the remaining videos in post-processing.

The rest of the videos will be used to construct snapshots of the velocity field during 0.2 s time windows centered at 2 s intervals throughout the decay period. Only 0.2 s of each 0.284 s video is used for analysis; the extra images, five before the analysis window and five after, give all particles appearing in the analysis window an opportunity to satisfy the trajectory length criteria (see Sect. 3.3.3).

This timing scheme is significantly more complicated than the one applied to steady-state counterflow, and must be controlled by a computer to ensure timing accuracy. The network of instruments involved is shown in the block diagram of Fig. 3.10.

First the desired grid velocity is communicated to the motor controller as a four-bit binary number using four digital I/O channels on each of the multifunction I/O device and the motor controller. It then waits to receive a trigger pulse.

A Quantum Composers [96] Model 9518 Pulse Generator orchestrates the grid motion and image acquisition by triggering the motor controller, mechanical shutter, and camera. While the pulse generator gate is pulled up by the computer, image acquisition is active. A single pulse lasting 100 ms instructs the motor controller to move the grid to the top of the channel and hold it there. After a short delay, the shutter is opened and 35 8 μs pulses at 120 Hz trigger the camera. It acquires an image while the trigger input is pulled up, so the sensor is exposed for the pulse duration of 8 μs. The first 34 pulses cause the camera to capture images and the last pulse instructs it to switch to the next memory segment. The shutter trigger is deactivated at the end of each burst.
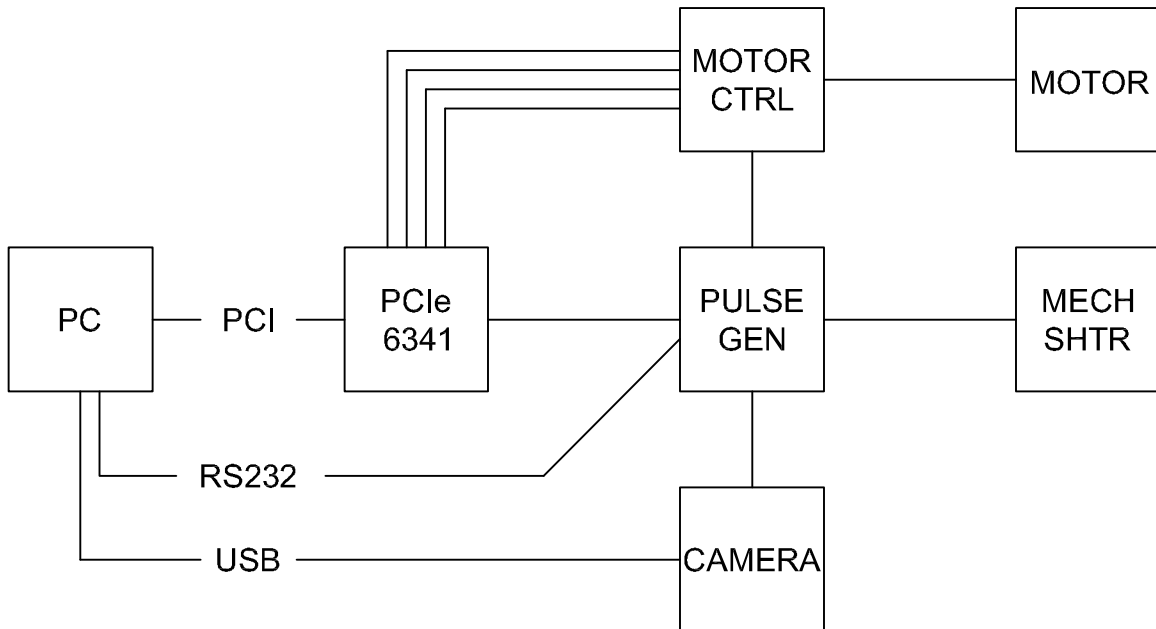
Figure 3.10: Block diagram of the instruments used to control the grid turbulence visualization experiment.

Trigger bursts for the shutter and camera are repeated at 2 s intervals until the pulse generator gate is pulled down at the end of the decay period.

Duration of the short delay t_d between the grid trigger and first camera burst depends on grid speed v_g. It is calculated such that the grid passes the center of the channel halfway through the first video. After accelerating at a constant rate $a_g = 525$ cm/s^2 for a time period of t_a, the grid reaches velocity v_g:

$$t_a = \frac{v_g}{a_g}. \tag{3.5}$$

During this finite acceleration period, the grid covers a portion of the stroke

$$s_a = \frac{1}{2} a_g t_a^2. \tag{3.6}$$

Substituting Eqn. (3.5) into Eqn. (3.6) produces an expression for s_a in terms of v_g:

$$s_a = \frac{v_g^2}{2a_g}. \tag{3.7}$$

Once the grid reaches v_g, the remaining distance to the center of the channel s_v is

$$s_v = \frac{s}{2} - s_a, \tag{3.8}$$

which is covered in the period of time

$$t_v = \frac{s_v}{/} v_g. \tag{3.9}$$

Substituting Eqn. (3.7) into Eqn. (3.8), and then putting the resulting expression for s_v into Eqn. (3.9) produces

$$t_v = \frac{s}{2v_g} - \frac{v_g}{2a_g}. \tag{3.10}$$

The total time required to reach the center of the channel is then the sum of the finite acceleration and constant velocity periods, Eqns. (3.5) and (3.10), and the delay time is this sum less half the duration of the video:

$$t_d = \frac{s}{2v_g} + \frac{v_g}{2a_g} - 0.142. \tag{3.11}$$

Once all 20 videos are acquired—all camera memory segments will be filled—they are automatically transferred to the computer. The grid automatically moves back to the bottom of the channel after about two minutes. It is possible for ice to form on the bellows while the grid is held at the top of the channel. This must be removed, otherwise small ice crystals trapped between the leaves may cause the bellows to rupture upon contraction.

3.3.3 Tracking algorithm

The particle tracking algorithm developed for this work is based on the feature-point tracking algorithm of Sbalzarini and Koumoutsakos [97], which itself seems to be adopted from Crocker and Grier [98]. Though the algorithm is available as open-source software, a customized adaptation written in a combination of MATLAB [99] and Fortran was developed for this work to improve execution speed and applicability to flow visualization in He II.

A three-dimensional array of pixel intensity values, $I_p(c, r)$, where p denotes the page index (image number), c the column (horizontal) index, and r the row (vertical) index, represents the sequence of images. Each image depicts the tracer particles as well as the channel side walls, the distance between which is used to convert a measured number of pixels to SI length units.

Image stabilization. A custom image stabilization routine minimizes the effect of environmental vibrations that cause the channel to appear in a different place in each image. Since the channel position changes, but not its geometry, image cross-correlation can be used to determine the channel displacement between two images. A sub-image, I_1^s, consisting of the first several columns—those that depict the channel wall—of the first image I_1 is used as a reference. Channel displacement in image I_p with respect to I_1 is then obtained by maximizing the cross-correlation function $R_{1p}(i)$ of the sub-images I_p^s and I_1^s:

$$R_{1p}(i) = \sum_r \sum_c I_1^s(c - i, r) I_p^s(c, r).$$

(3.12)

The correlation length i is typically restricted to $-5 \leq i \leq 5$, and the cross-correlation is applied in the horizontal direction only. Channel walls are then cropped out of the images, and the number of columns cropped from the left side of each image is adjusted by the correlation length that maximizes R_{1p}.

Particle location. Particle coordinates in each image are inferred by local intensity maxima, and sub-pixel resolution is obtained through intensity moments. First, background variation and digital camera discretization noise are removed from the stabilized images using a combination low-pass and Gaussian filter. The filter kernel K is given by

$$K(i, j) = \frac{1}{BK_0} \left(e^{\left(-\frac{i^2 + j^2}{4\lambda^2}\right)} - \frac{B}{(2w + 1)^2} \right),$$

(3.13)

where B and K_0 are normalization constants (see Sbalzarini and Koumoutsakos [97]), λ is the Gaussian filter half-width (typically $\lambda = 1$), and w is the kernel radius. The filtered image I_p^f is obtained by the convolution of I_p and K:

$$I_p^f(c,r) = \sum_{i=-w}^{w} \sum_{j=-w}^{w} I_p(c-i, r-j) K(i,j).$$

(3.14)

Dilated images I_p^d are obtained by grayscale dilation of the filtered images. Any position (c,r) that satisfies $I_p^d(c,r) = I_p^f(c,r)$ is a local light intensity maximum. Maxima that exceed a threshold intensity (typically $12\mu_p$, where μ_p is the mean intensity of image p) are considered candidate tracer particle centroid locations.

To exclude large particles that do not faithfully follow the flow, the particle location algorithm is executed twice. A relatively large filter kernel (typically $w = 12$), which favors larger particles, is applied on the first pass. A smaller kernel (typically $w = 3$) is more suitable for detecting small particles and is applied on the second pass. Any candidate particle detected on the first pass that would saturate the smaller kernel is removed from the image. This criteria is based on the zero-order intensity moment m_0, given by

$$m_0 = \sum_{i^2+j^2 \leq w^2} I_p^f(c+i, r+j).$$

(3.15)

Saturation is assumed if $m_0 > 0.6\pi w^2$, where the relevant w is that of the second-pass kernel.

On the second pass, candidate locations of the suitably sized particles are refined with sub-pixel resolution using the center-of-intensity moments ϵ_c and ϵ_r:

$$\begin{bmatrix} \epsilon_c \\ \epsilon_r \end{bmatrix} = \frac{1}{m_0} \sum_{i^2+j^2 \leq w^2} \begin{bmatrix} i \\ j \end{bmatrix} I_p^f(c+i, r+j).$$

(3.16)

The second-order intensity moment m_2 for each particle is given by

$$m_2 = \frac{1}{m_0} \sum_{i^2+j^2 \leq w^2} (i^2 + j^2) A_p^f(c+i, r+j)$$

(3.17)

and will be used in the linking algorithm to form particle trajectories. Refined candidate locations $(c + \epsilon_c, r + \epsilon_r)$ for each image and their associated intensity moments m_0 and m_2 are saved to disk for use by the linking algorithm.

Sbalzarini and Koumoutsakos describe an additional step in which the intensity characteristics (m_0 and m_2) of the candidates are compared with each other, and any outliers are eliminated from

the list. This is designed to prevent false detections carrying forward into the linking algorithm, but it assumes that the majority of particles have similar size and shape. Solidified D_2 particles are not uniformly shaped or sized, so this step is omitted.

Trajectory formation. Candidate particles identified in I_p are linked with the corresponding candidate particles in I_{p+1} through an association matrix G of size $m+1$ by $n+1$, where m is the number of candidate particles in I_p and n the number of candidate particles in I_{p+1}. If candidate i from I_p is the same particle as candidate j from I_{p+1}, then $G(i,j) = 1$ to indicate the link. The extra, or zeroth, row and column handle particles that appear in only one image. For example, $G(i,0) = 1$ indicates that candidate particle i appears in I_p but not in I_{p+1}. Only one link can occur in each row and column of G (except for the zeroth row and column; there can be multiple particles that are not linked). The correct form of the association matrix is obtained by shuffling the links until a cost functional, Φ, is minimized:

$$\Phi = \sum_{i=0}^{m} \sum_{j=0}^{n} \phi(i,j) G_{ij}. \tag{3.18}$$

The cost function, ϕ, should be a function of two candidate particle characteristics and should have a global minimum where candidate i and candidate j represent the same physical tracer particle. For this work the cost function is

$$\phi(i,j) = (c_i - c_j)^2 + (r_i - r_j)^2 + (m_{0,i} - m_{0,j})^2 + \frac{1}{4}(m_{2,i} + m_{2,j})^2. \tag{3.19}$$

This is nearly the same cost function suggested by Sbalzarini and Koumoutsakos, except that the influence of m_2 has been reduced so that non-uniformity of the particle shape will not prevent links. In some cases, an additional restriction is placed on the trajectory angle, making it prohibitively expensive to link particles in a way that introduces a bend in the track exceeding $\pm 45°$. This improves reliability when the particle displacement between images exceeds the separation distance between particles, for example in the first several seconds of decaying grid turbulence, when the local fluid velocity is quite large.

Once Φ is minimized the established links are used to generate particle tracks, or add data for newly linked particles to existing tracks, as appropriate. One comma-separated value file is written for each track, containing the (p, c, r) coordinates of each point. After all successive pairs of images

have been linked, any trajectory files containing less than six entries are discarded. This serves as a last line of defense against incorrect links.

The resulting list of particle trajectories represents temporal and spatial coordinates, $(t, \mathbf{x})$, of many particles throughout the flow field. Such data can easily be converted into velocity measurements, which are immensely useful for characterizing the flow field, as will be discussed in the experimental results presented in the next several chapters.

3.4   Chapter summary

To generate quality data for characterization of He II turbulence, the experimental apparatus must first be safely cooled down to cryogenic temperature, and then either a second sound attenuation or flow visualization experiment carefully executed. A second sound data acquisition system has been designed and calibrated to work with the custom second sound transducers and produce quality vortex line density measurements in both steady-state and transient flow. Tracer particles for flow visualization can be produced in He II, and their motion in either thermal counterflow or towed-grid turbulence tracked with a customized and efficient algorithm, resulting in quantitative information about the fluid velocity.

CHAPTER 4

PARTICLE MOTION IN STEADY-STATE THERMAL COUNTERFLOW

Flow visualization has become a popular tool for the study of thermal counterflow, with several different methods applied in the most recent two decades [100], but analysis of counterflow visualization data remains particularly challenging because of the numerous factors that influence particle motion. Besides interactions with the normal fluid through viscous forces and the superfluid through inertial and added mass effects [53], particles can become trapped on quantized vortices [17, 49], which move at some velocity $\mathbf{v}_L \neq \mathbf{v}_s$. Furthermore, the particles are not necessarily stationary on the vortices, but are thought to slide along the core due to a drag force exerted by the normal fluid [50, 51].

A concrete understanding of this ambiguous particle motion in thermal counterflow has been the subject of numerous experimental, theoretical, and computational efforts. The work that relates to particle motion and velocity statistics will be reviewed in this chapter, and a new method for analyzing PTV data will be presented, in which particles entrained by the normal fluid are analyzed separately from those trapped on vortices. Applying this new method to the routine investigations of particle motion and velocity statistics reveals some interesting points that were previously missed.

4.1 Background and motivation

The first experiments by Zhang and Van Sciver made use of the PIV technique [54], in which a pair of images separated by a short time interval are segmented, and cross-correlation of the segments together with knowledge of the image separation time is sufficient to obtain the velocity vector for each segment [45]. Zhang and Van Sciver studied counterflow in a vertical channel generated by a range of heat flux, $110 \leq q \leq 1370$ mW/cm^2, at a variety of temperatures, $1.62 \leq T \leq 2.00$ K. They found that for a one-dimensional counterflow, regardless of temperature or applied heat flux, the measured particle velocity, v_p, is approximately half of the theoretical normal

fluid velocity: $v_p \approx v_n/2$. According to the subsequent theory of Sergeev et al., the observed behavior can be explained by interactions between the particles and quantized vortex lines [101].

Other experimental investigations of particle motion in thermal counterflow have employed the PTV technique [48, 52, 102, 103], in which individual particle locations are tracked throughout a sequence of images. The results of Paoletti et al. show that some particle tracks correspond to the normal fluid motion, exhibiting relatively straight trajectories with mean particle velocity $v_p \approx v_n$ in the same direction as the heat current, while others show erratic behavior with net motion against the heat current [52]. In this experiment the temperature range was $1.80 \leq T \leq 2.15$ K and the heat flux range was $13 \leq q \leq 90$ mW/cm^2, an order of magnitude less than that of Zhang and Van Sciver. The numerical work of Kivotides suggests two regimes of particle motion that are separated by the applied heat flux. The simulations show that when the vortex tangle is relatively dilute, as is the case when the applied heat flux is lower, particles have a relatively large mean free path through the tangle, with some traversing the entire observation volume at v_n without interacting with vortices [50]. On the other hand, when the tangle is relatively dense, particles cannot avoid interaction with vortices, and their mean velocity is lower than v_n [104].

Chagovets and Van Sciver used the PTV method intending to scan a parameter space covering that of the PIV experiment by Zhang and Van Sciver as well as the PTV experiment by Paoletti et al., thereby observing the transition between the two proposed flow regimes in a single experiment [48]. However, due to a hardware limitation, the heat flux range was limited to $7 \leq q \leq 100$ mW/cm^2 at $1.55 \leq T \leq 2.00$ K [48], which does not quite extend into the region probed by Zhang and Van Sciver. The results were nonetheless insightful, providing a discussion of the trapping of particles on quantized vortices and their subsequent dislocation, which presumably plays a role in the transition between the two regimes of particle motion [48]. Work has continued on classifying particle motion in thermal counterflow, with approaches focused on qualitative features of the particle trajectories [102] and analysis of particle motion as a function of their size [103].

Another experimental approach to thermal counterflow that makes use of PTV is the analysis of transverse (i.e., perpendicular to the direction of normal fluid flow) particle velocity statistics. It has been shown that for both steady state [105] and decaying [106] counterflow, the probability density function (PDF) for transverse particle velocity u_p exhibits a Gaussian core with non-classical tails proportional to $|u_p|^{-3}$. In some cases, the tails are attributed to the motion of particles trapped

on vortices that have just experienced a reconnection event [106]. Others point out that the tails can be predicted from the superfluid velocity field in the vicinity of a vortex core, without the need to consider vortex reconnection [95, 105]. However, in light of numerical simulations that show particles suitably close to the vortex core have a tendency to become trapped rather than trace the superfluid velocity field [107, 108], this explanation is unlikely. Regardless, the tails have been shown to exist only when the probing time, t_1, is smaller than the average travel time between quantized vortex lines, $t_2 = \ell / \langle v_p \rangle$, where $\ell = L^{-1/2}$ represents the mean distance between vortex lines. When the ratio of these times, $\tau = t_1/t_2$, exceeds unity, the tails disappear and the PDF assumes the classical Gaussian form [105]. This has been interpreted as an implication that counterflow turbulence behaves classically on large length scales [95, 105].

To further explore the motion of particles in thermal counterflow, a systematic collection of steady-state thermal counterflow data has been acquired across a wide range of heat flux. The data cover $38 \le q \le 215$ mW/cm^2 at $T = 1.70$ K, $38 \le q \le 366$ mW/cm^2 at $T = 1.85$ K, and $17 \le q \le 481$ mW/cm^2 at $T = 2.00$ K. This parameter space substantially overlaps those of the existing PTV experiments ($13 \le q \le 90$ mW/cm^2 at $1.80 \le T \le 2.15$ K [52] and $7 \le q \le 100$ mW/cm^2 at $1.55 \le T \le 2.00$ K [48]) and the original PIV experiment ($110 \le q \le 1370$ mW/cm^2 at $1.62 \le T \le 2.00$ K [54]).

In the following sections, the data set is used to more or less repeat the previous investigations into streamwise particle motion and transverse velocity statistics. However, two important points separate this effort from existing work. For the first time in a single experiment, the applied heat flux range overlaps with the PIV experiments of Zhang and Van Sciver as well as with the PTV experiments of Paoletti et al. and Chagovets and Van Sciver, providing experimental resolution of the apparently disparate relationships between v_p and v_n. Secondly, a new particle classification scheme, based on streamwise velocity v_p, is introduced so that particles entrained by the normal fluid can be analyzed separately from those trapped on vortices. Application of the separation scheme indicates that some information is missed when all particles are grouped together, as was the approach in previous experiments.

4.2 Streamwise particle behavior

Fig. 4.1 shows some of the particle tracks observed at 1.85 K as well as the corresponding streamwise velocity PDFs. Though the particle tracks have the same structure as those shown in several previous studies [48, 52, 102], and it is well known that streamwise velocity PDFs, at least in the lower heat flux regime, exhibit two peaks [52, 94, 106], this figure showcases the novelty of the new approach to data analysis. The two-peak structure of the PDFs exemplified in Figs. 4.1(d) and (e) is the basis for analyzing the motion of particles moving with the normal fluid separately from those under the influence of the vortex tangle. Those moving with the normal fluid, whose velocity measurements contribute to the peak with higher mean value, are given the name "Group 2" or G2 for short. Those moving with the vortex tangle, whose velocity measurements contribute to the peak with lower mean value, are given the name "Group 1" or G1. For qualitative differentiation, the following criteria decide whether an instantaneous velocity sample represents G1 or G2 behavior. If the instantaneous velocity of a particle satisfies $v_p < \mu_2 - 2\sigma_2$, where μ_2 and σ_2 are the mean and standard deviation, respectively, for a Gaussian curve fit to the G2 peak, it is assumed to exhibit G1 behavior. Likewise, if $v_p > \mu_1 + 2\sigma_1$, it is assumed to exhibit G2 behavior. In cases where $\mu_2 - \mu_1 > 2\sigma_1 + 2\sigma_2$, i.e. the peaks are well separated, the criteria are reversed ($v_p < \mu_1 + 2\sigma_1$ counts as G1 and $v_p > \mu_2 - 2\sigma_2$ counts as G2) to prevent measurements falling in between the two peaks from counting toward both groups. As a result, the separation scheme generates ensembles of velocity measurements that represent G1 and G2. For brevity in the ensuing discussions, these names are used to refer interchangeably to the entire physical group of particles as well as the representative measurement ensemble. An additional group, G3, is defined for the high heat flux regime. Since the streamwise velocity PDF exhibits just one peak for higher heat flux, as exemplified in Fig. 4.1(f), all of the measured velocity samples are representative of G3 behavior.

The tracks and Gaussian fits of Fig. 4.1 are color coded: G1 is shown in blue, G2 in red, and G3 in black. In the top row (Figs. 4.1(a) and (d)), which represents relatively low heat flux ($q = 38$ mW/cm^2), the G2 tracks are long, straight, and oriented in the same direction as the heat current, while the G1 tracks meander and are randomly oriented. The corresponding peaks in the PDF are well defined (i.e., clearly separated from one another). In the middle row (Figs. 4.1(b) and (e)), which represents moderate heat flux ($q = 122$ mW/cm^2), the G2 tracks are still straight
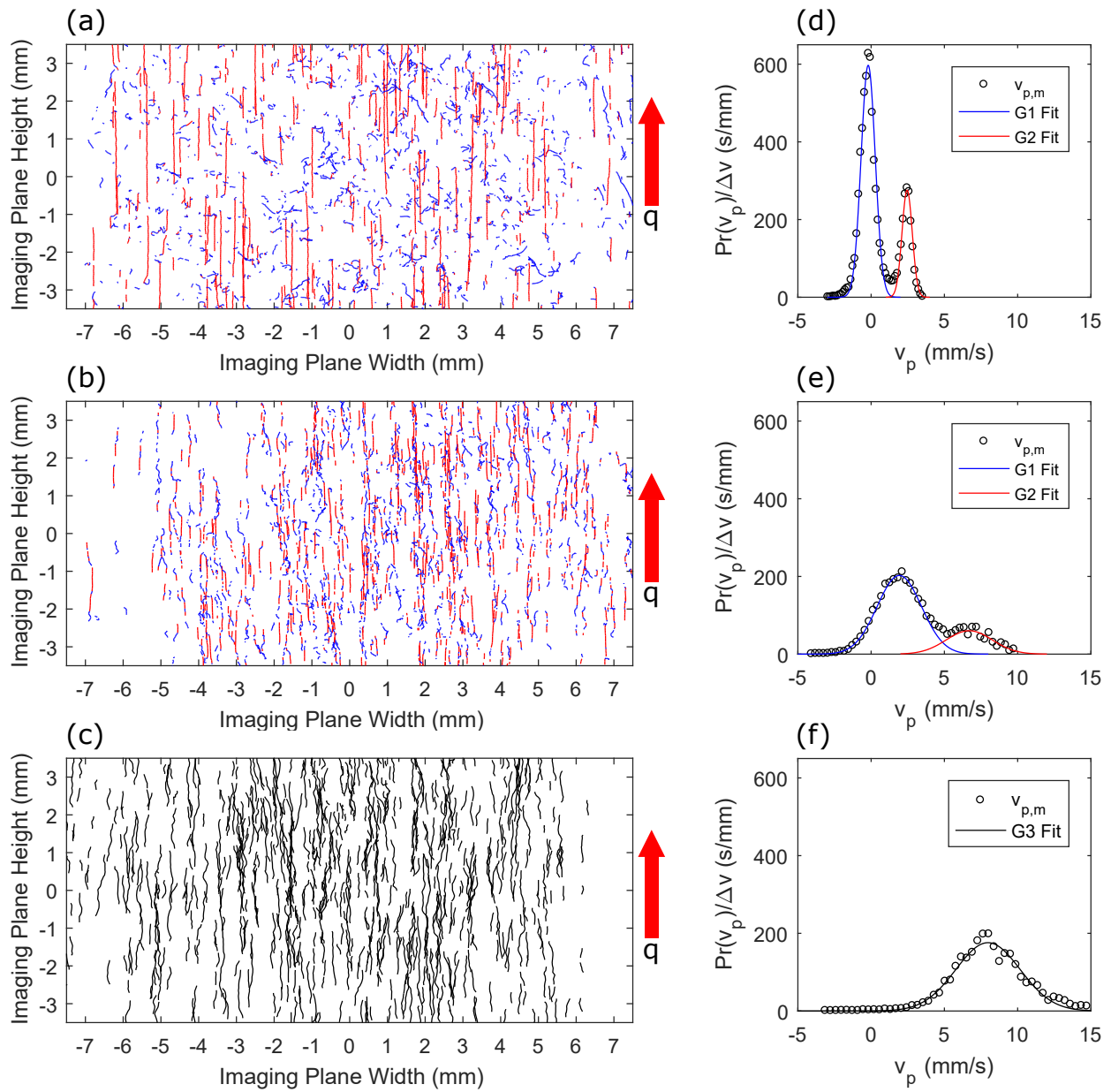
Figure 4.1: (a)-(c): Particle tracks observed for $q = 38$, 122, and 320 mW/cm^2, respectively, at 1.85 K. (d)-(f): Corresponding particle streamwise velocity PDFs.

and vertically oriented, but are frequently interrupted by short G1 segments. This likely represents the trapping of particles by quantized vortices, and the subsequent dislocation of the particle that stems from the increased normal fluid drag force [48, 50]. As a whole, the G1 tracks move in the same direction as the heat current, though in a slower and considerably less undeviating fashion than the G2 tracks. A positive shift in the mean value of both peaks can be observed in Fig. 4.1(e), and the peaks are less well defined, appearing to merge together. Though the evolution of particle velocity as a function of applied heat flux in this regime has been thoroughly discussed by Chagovets and Van Sciver, their assumption that the two group behavior continues indefinitely does not appear to be correct [48]. The bottom row (Figs. 4.1(c) and (f)), representing higher heat current ($q = 320$ mW/cm^2), shows that G3 tracks are all oriented in the same direction as the heat current but exhibit significant transverse motion, and their PDF exhibits only one peak.

For consistency with the existing experimental literature [48, 52, 54, 94], Fig. 4.2 shows v_p as a function of v_n for each point in the parameter space. The top panel shows results only for $T = 2.00$ K and the bottom panel shows results for the other two temperatures. v_p is represented by the mean value of Gaussians fit to the streamwise velocity PDFs (as in the examples of Figs. 4.1(d)-(f)). In all cases, v_p for the G2 peak is approximately equal to $v_n + v_{slip}$, where v_{slip} is the velocity offset caused by non-neutral density of the particles. This trend is indicated by the solid black line. Mean velocity of the G1 peak, for very small heat flux, is similar to the superfluid velocity with the same correction factor, $v_s + v_{slip}$, indicated by the blue line. This behavior is expected for low counterflow velocities since the superfluid carries the vortex tangle, on average, at v_s [109], and it has been demonstrated in recent visualization experiments [48, 52] and numerical simulations [51]. As the heat flux increases and mutual friction begins to affect the vortex tangle, the G1 velocity departs from $v_s + v_{slip}$ and instead corresponds to $v_n/2 + c$, indicated by the dashed black line, where c is an offset of about 2 mm/s. At 2.00 K, as the heat flux continues to increase, the single peak PDF structure appears, with the mean value beginning from some value between v_n and $v_n/2 + c$ and eventually settling at the latter. This transition region occurs between normal fluid velocities of roughly 7 and 15 mm/s, as indicated by the vertical dotted lines in Fig. 4.2(a). However, for 1.85 and 1.70 K, this transition appears to be absent, with the mean value of G3 PDFs immediately collapsing onto the $v_n/2 + c$ trendline when v_n exceeds 7 or 8 mm/s. This probably results from a limitation of the imaging system; it seems that particles moving faster than about 9 mm/s cannot
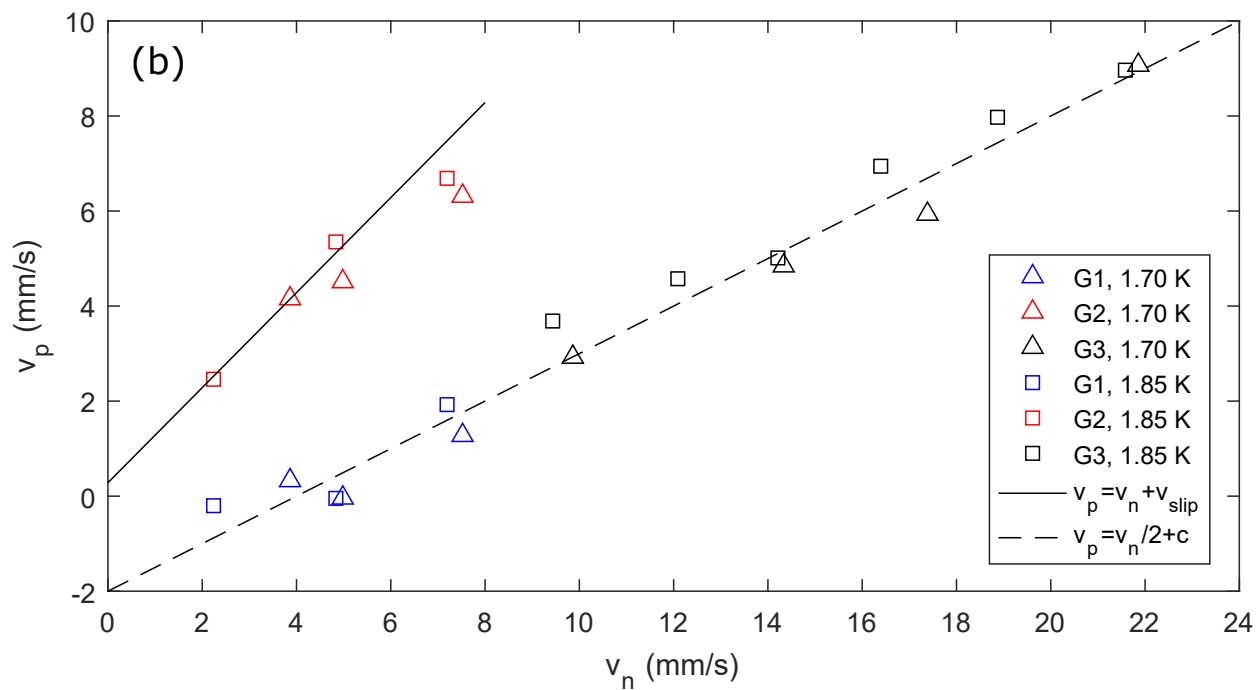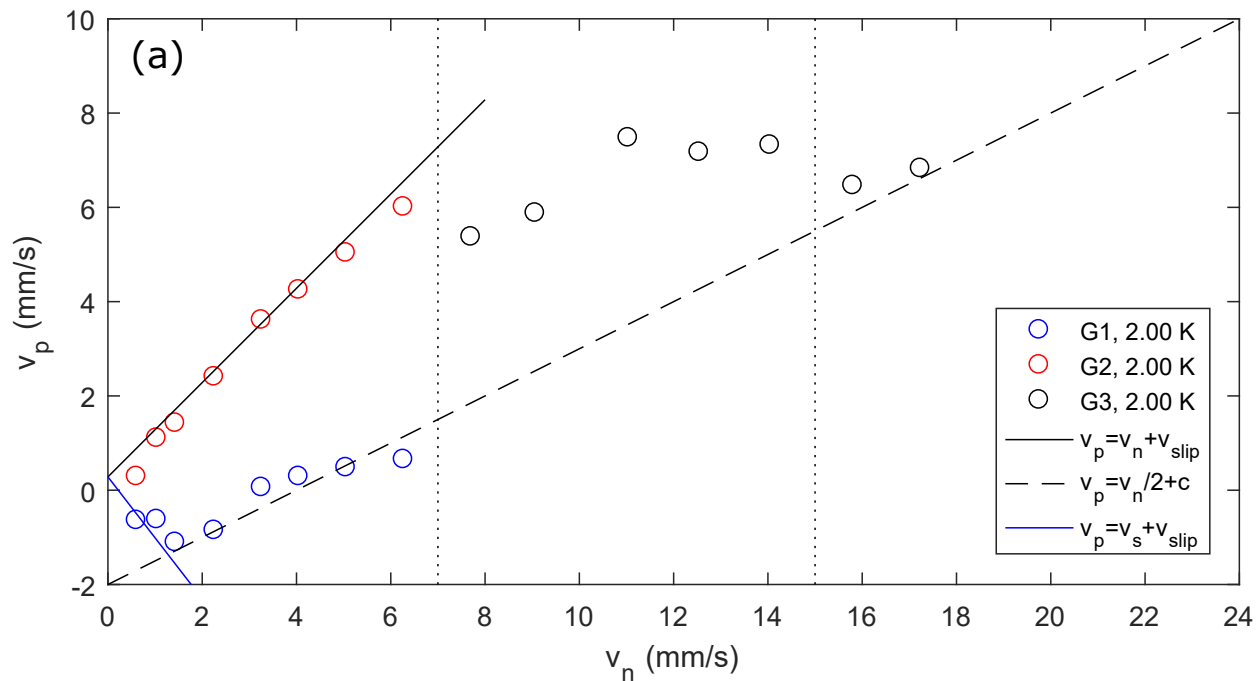
Figure 4.2: Measured particle velocity v_p as a function of the theoretical normal fluid velocity v_n for (a) $T = 2.00$ K and (b) $T = 1.85$ K and $T = 1.70$ K.

be resolved. Since the dynamic viscosity of the normal fluid is smaller at these temperatures than at 2.00 K [44], it makes sense that the critical drag force preventing particles from remaining trapped on vortices [48] is surpassed at higher values of v_n that may be beyond what can be resolved. In this case, the G3 data shown in Fig. 4.2 would in fact be miscategorized G1 data. As an additional note, small values of v_{ns} were not observed at these temperatures, so the transition of G1 velocity from $v_s + v_{slip}$ to $v_n/2 + c$ does not appear either.

These observations are consistent with the existing literature on experimental measurements of particle motion in thermal counterflow: when the applied heat flux is lower, particles can be observed moving at approximately v_n [52], and when it is higher, particles can be observed moving at approximately $v_n/2$ [54]. However, this is the first time that one experiment yields both observations, experimentally confirming a long-held theory that the early discrepancy was a matter of different flow regimes occurring for different ranges of the applied heat flux [53].

4.3   Transverse particle velocity

Statistical analysis of particle motion in thermal counterflow using PTV is typically focused on the evolution of transverse particle velocity or acceleration PDFs with changing temperature, heat flux, or most commonly, probing time scale [95, 105, 110, 111]. In these analyses the statistical sample consists of all of the detected particles. This approach raises some concern when one considers the vastly different characteristics of the transverse motion exhibited by the G1 and G2 tracks in Fig. 4.1(a), and to a lesser extent in Fig. 4.1(b). The following analysis of the transverse particle velocity for G1 and G2 shows that some information is indeed missed when the two groups are not considered separately.

First note that, within each group, the streamwise and transverse velocity components are uncorrelated. In other words, the samples taken from any slice of the streamwise PDF will accurately represent the entire transverse distribution (provided the extracted sample size is large enough), and vice versa. This is important to the success of the separation scheme since the streamwise velocity PDFs for G1 and G2 end up quite lopsided. However, as will be seen in the figures of this section, the transverse velocity PDFs are sufficiently resolved.

Fig. 4.3 shows G1, G2, and combined (G1+G2) transverse velocity PDFs. In Fig. 4.3(a) ($q = 91$ mW/cm^2) the G2 sample size exceeds the G1 sample size. In Fig. 4.3(b) ($q = 113$ mW/cm^2)
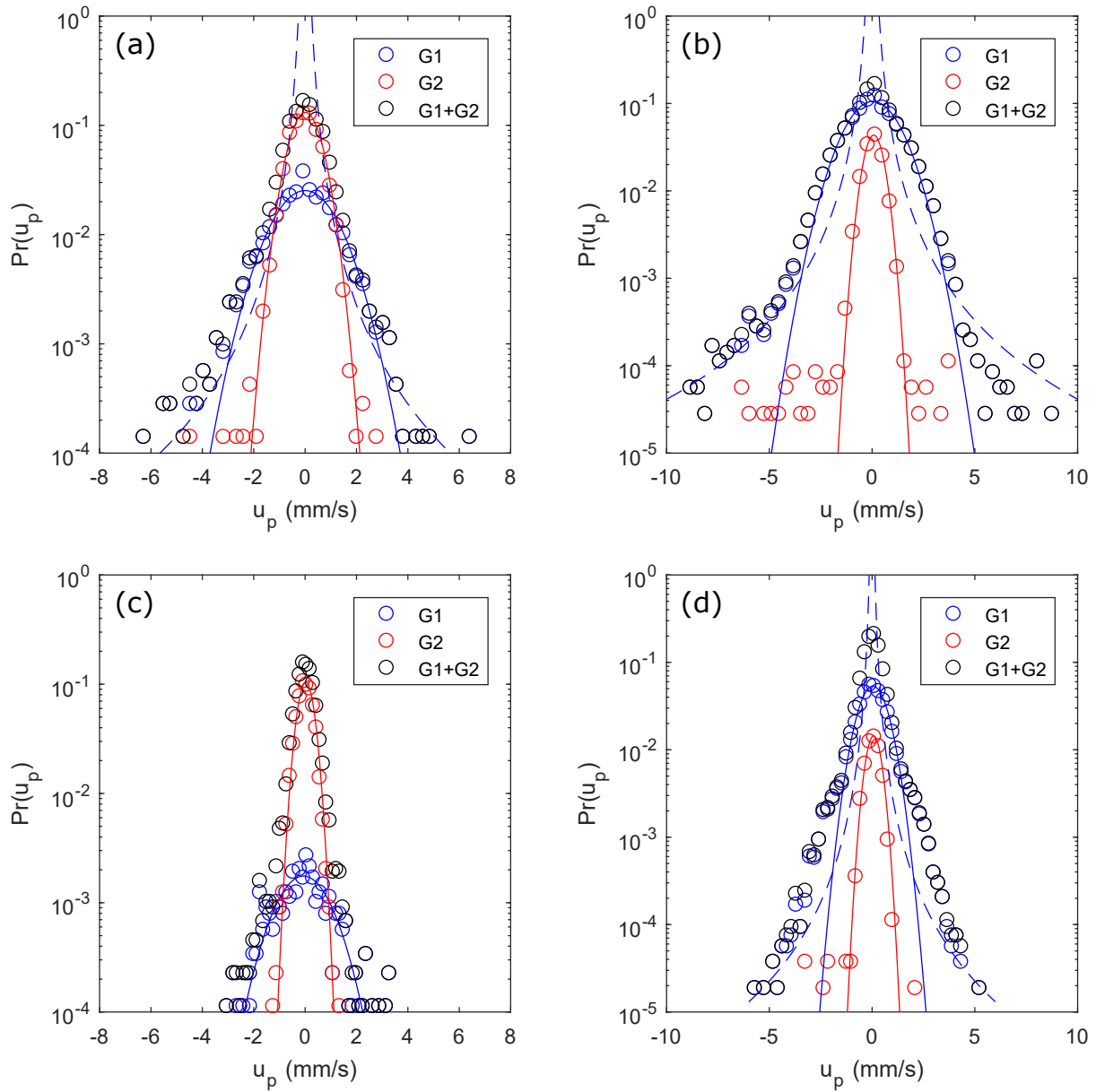
Figure 4.3: Probability distributions for the measured transverse particle velocity at $T = 2.00$ K for the cases where (a) $q = 91$ mW/cm^2 and (b) $q = 113$ mW/cm^2. (c) and (d) show the same data but the minimum probing length has been changed to 2ℓ.

the opposite is true. To show the relative contributions of G1 and G2 to the combined PDF, the normalization is $Pr_{g,i} = n_{g,i}/N$, where $n_{g,i}$ is the number of samples in the ith bin for group g, and N is the total number of combined G1 and G2 samples. It is clear that, regardless of the relative sample size, G1 dominates the tail region of the combined PDF. Though the G2 PDFs appear to have some structure at the ends, it is not coherent and occurs with probability at least an order of magnitude less than the corresponding G1 contribution. This is likely due to a small number of misclassified velocity measurements; those with streamwise component more than two standard deviations outside the group mean can be potentially placed in the wrong group. This effect could be confirmed by inspecting the location of these specific velocity samples in the particle tracks, and judging based on the local geometry whether they truly belong to G1 or G2.

The Gaussian core of the G1 PDF is substantially wider than the G2 PDF. This becomes of consequence when the G2 sample size is larger, as in Fig. 4.3(a). As a result, the combined PDF may be broken into three regions. The tip region is Gaussian and due primarily to the G2 PDF. The middle region is due to the combined G2 PDF and Gaussian core of the G1 PDF, and has a different mathematical description than the tip region. The tail region exhibits the $|u_p|^{-3}$ power law behavior due exclusively to the G1 PDF tails. If the combined PDF is considered alone, it is possible to mistake the middle region for the beginning of the power law tails, leading to incorrect conclusions about the particle velocity statistics.

Figs. 4.3(c) and (d) show the same data as Figs. 4.3(a) and (b), respectively, except the minimum probing length scale has been increased to 2ℓ, twice the mean vortex line spacing. It is important to note that this differs from the approach described in the existing literature [105], which is an adjustment of the probing time scale. The latter is achieved by using every other, or every third, etc., position measurement along a particle track to calculate the velocity, simulating a reduction in the image acquisition rate [105]. Alternatively, a true adjustment of the minimum probing length can be accomplished by discarding position measurements only if they are not sufficiently separated from the previous location in the trajectory. Velocity samples are then computed as $\mathbf{v}_i = (\mathbf{x}_{i+j} - \mathbf{x}_i)/jdt$, where i represents the ith position along a track and j represents the number of subsequent points to skip such that $\|\mathbf{x}_{i+j} - \mathbf{x}_i\|$ exceeds the desired minimum length scale. Increasing the probing length in this manner results in a drastic reduction of the number of G1 samples, since the mean G1 velocity is small compared to the mean G2 velocity. For a fixed

sample size, the PDF tails are quenched since many of the measurements contributing to them are discarded. This is apparent in Fig. 4.3(c), where the probability of observing a particle with G1 velocity is drastically reduced, and the extents of the PDF do not resemble the power law curve. The tails of Fig. 4.3(d) are more or less eliminated as well, though the effect is not as obvious since the G1 sample size for this case was considerably larger.

An alternative way to present the data is shown in Fig. 4.4, which contains several transverse velocity PDFs for each of G1, G2, and G3. Several curves with different values of the non-dimensional time τ are shown in each case. In the same manner as the existing literature, $\tau = t_1/t_2$, where t_1 is the time elapsed between successive images and $t_2 = \ell/\langle v_p \rangle$ [105], except that in this case $\langle v_p \rangle$ is computed for each group instead of for all of the detected particles. Defined in this way, t_2 represents the average time for a particle of each respective group to traverse the intervortex distance.

A Gaussian form is evident in the core of all PDFs, regardless of group or probing time scale, as indicated by the solid black curve in all three panels $\left(A \exp\left(-(u_p/\sigma_u)^2 \right) \right.$, where A is a constant). This is consistent with the existing literature [95, 105]. For G1, shown in Fig. 4.4(a), a power law curve $(A|u_p/\sigma_u|^{-3}$, where A is a constant), indicated by the dashed curve, can be drawn through
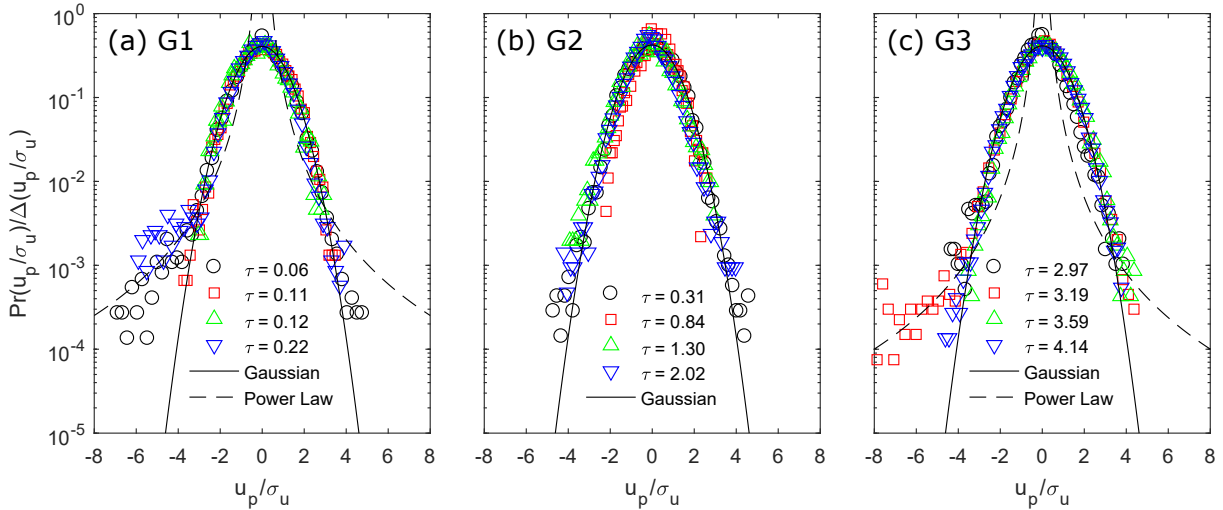

Figure 4.4: Normalized probability distribution for the measured transverse velocity of particles contributing to (a) G1, (b) G2, and (c) G3.

the tail region. This region is defined as the data that falls more than $4\sigma_u$ from the center of the PDF. While the size of this data set is not sufficient to resolve extended tails, deviation from the Gaussian profile is clear, and the nondimensional time is less than unity for all of the cases shown, indicating that the probing time is smaller than the average intervortex travel time. According to the existing literature, these are the correct conditions for power law tails [95, 105].

The G2 PDFs of Fig 4.4(b) present a different picture: all cases show purely Gaussian form, even though $\tau < 1$ for some data and $\tau > 1$ for others. This is likely because G2 consists of velocity measurements contributing to the part of the streamwise PDF that is normally attributed to particles moving with the normal fluid [48, 52]. Since the normal component behaves more or less classically, it makes sense for the normal fluid transverse velocity PDF to have the same Gaussian form that a classical fluid PDF would have.

Despite the relatively long probing times ($\tau \gtrsim 3$) for G3 PDFs, shown in Fig. 4.4(c), deviation from the Gaussian core can be observed in one case. As with G1, a power law curve can be drawn through this tail structure. Previous experimental results suggest that the PDF should have Gaussian form if $\tau > 1$, but those investigations did not include the high heat flux G3 region [105]. Indeed, little is known about the novel form of turbulence that exists in this high heat flux region, where both the normal fluid [23] and superfluid can become turbulent.

4.4   Root mean square velocity fluctuation

A feature of both streamwise and transverse velocity PDFs that has not yet been considered is the peak width, which is related to the standard deviation, or root mean square velocity fluctuation. Fig. 4.5 shows the standard deviation of the Gaussians fit to all streamwise and transverse velocity data obtained at 2.00 K. Data for G1 is shown in blue, G2 in red, and G3 in black. At first glance, the figure adds weight to the importance of the separation scheme, particularly for the analysis of transverse velocity statistics, since a clear divergence between G1 and G2 transverse velocity fluctuation is evident as the heat flux increases. Closer inspection reveals some additional, more subtle, observations.

The measured transverse velocity standard deviation σ_u for G2 is fairly constant throughout the range of applied heat flux at 2.00 K; the velocity fluctuation does not increase noticeably until the transition to G3. This suggests that the normal fluid may not be turbulent in the two-peak
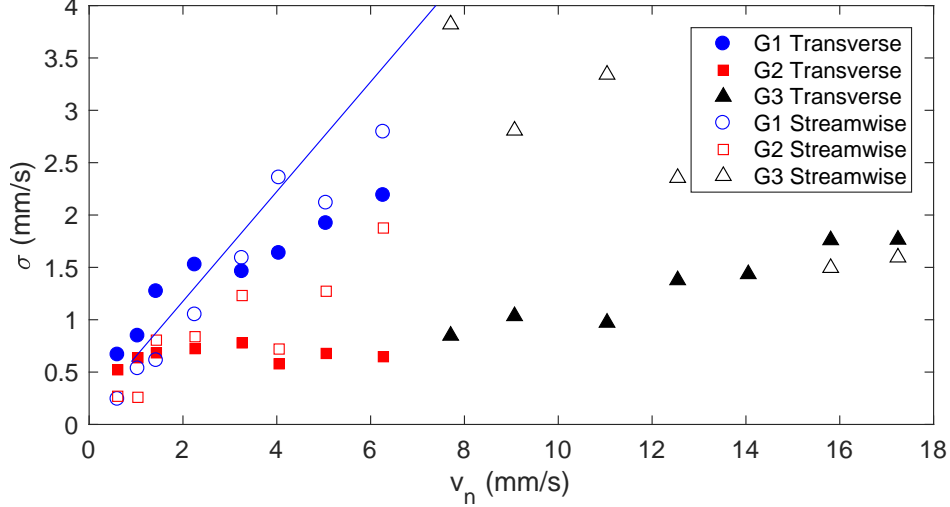
Figure 4.5: Standard deviation of the measured streamwise and transverse particle velocity for G1, G2, and G3 at $T = 2.00$ K.

regime. A measurement of vortex line density in decaying counterflow can be employed to further investigate this possibility. According to the recent work of Gao et al., if large-scale turbulence exists in the normal fluid, the line density should decay briefly as $L(t) \propto t^{-1}$ before exhibiting a "bump" structure and transitioning to $L(t) \propto t^{-3/2}$ [112]. If large-scale turbulence is absent, the decay should follow $L(t) \propto t^{-1}$ throughout the entire decay. Fig. 4.6 shows the decay of VLD at 1.70 K from a steady-state counterflow in the two-peak region (G1 and G2, $q = 50$ mW/cm^2) and the single peak region (G3, $q = 193$ mW/cm^2). Indeed, line density decays from the two-peak region as $L(t) \propto t^{-1}$ before background noise dominates the second sound signal, while a clear "bump" structure and associated change in the decay rate is seen for decay from the single-peak region. Together, the velocity fluctuation observed with PTV in steady-state counterflow and the VLD decay rate observed with second sound attenuation in decaying counterflow strongly suggest that large-scale normal fluid turbulence is absent from the two-peak regime.

Unlike the transverse fluctuations, streamwise velocity fluctuation for G2 does appear to increase with heat flux. A probable explanation proposed by Vinen [113] is that since particles exhibiting G2 behavior move primarily under the influence of drag force from the normal fluid, their velocity is subject to local variations of the normal fluid velocity. As the normal fluid passes across the vortex tangle, wakes can form behind each individual vortex line due to mutual friction; within these
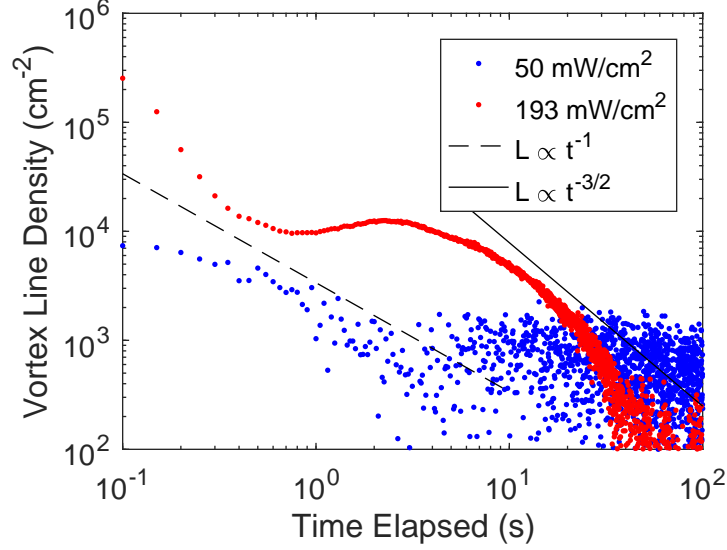
Figure 4.6: Vortex line density in decaying thermal counterflow from the two-peak and single-peak regions.

wakes, the normal fluid velocity can vary significantly. It makes sense that the same fluctuations do not appear in the transverse particle velocity since there is no mean flow in that direction.

Turning to G1, velocity fluctuations in both the streamwise and transverse direction increase linearly with applied heat flux. It may be that the G1 velocity fluctuations are tied to fluctuations of the vortex line velocity. Based on the localized induction approximation, the line velocity as a function of its local curvature R can be written as [114]:

$$v_L = \frac{\kappa}{4\pi R} \ln\left(\frac{R}{\xi_0}\right).$$

(4.1)

The line velocity fluctuation can then be obtained from $\langle v_L^2 \rangle^{1/2}$:

$$\langle v_L^2 \rangle^{1/2} = \frac{\kappa}{4\pi} \left\langle \frac{1}{R^2} \ln^2\left(\frac{R}{\xi_0}\right) \right\rangle^{1/2}.$$

(4.2)

Neglecting the slow variation of the natural logarithm with L, the substitution $R \approx \ell$ can be made and the constant $\ln\left(\ell/\xi_0\right)$ removed from the average [115]. The remaining term $\langle 1/R^2 \rangle^{1/2}$ can be replaced by $c_2 L^{1/2}$, where c_2 is a temperature dependent parameter [114–116], and the line density can be written in terms of the normal fluid velocity as per (1.6):

$$\left\langle \frac{1}{R^2} \right\rangle^{1/2} \approx c_2 \gamma \left(\frac{\rho}{\rho_s} v_n - v_0 \right).$$

(4.3)

62

The resulting expression for root mean square vortex line velocity fluctuation as a function of the normal fluid velocity is:

$$\begin{aligned} \langle v_L^2 \rangle^{1/2} &\approx \frac{\kappa c_2 \gamma}{4\pi} \ln\left(\frac{\ell}{\xi_0}\right)\left(\frac{\rho}{\rho_s}v_n - v_0\right) \quad \text{if} \quad \frac{\rho}{\rho_s}v_n > v_0 \\ \langle v_L^2 \rangle^{1/2} &= 0 \quad\quad\quad\quad\quad\quad\quad\quad\quad\quad \text{if} \quad \frac{\rho}{\rho_s}v_n \leq v_0 \end{aligned} \tag{4.4}$$

This simple approach yields a linear relationship between $\langle v_L^2 \rangle^{1/2}$ and v_n, provided the counterflow velocity exceeds v_0. Using values for c_2 [115] and γ [29] derived from the work of Gao et al., and an approximate value of $\ell \approx 100\,\mu\text{m}$, the proportionality constant is 0.54. The solid blue line of Fig. 4.5 represents Eqn. (4.4), with a small offset to adjust for environmental noise. It agrees reasonably well with the observed G1 velocity fluctuation, suggesting that the G1 particle velocity fluctuations are, to a good extent, caused by fluctuations of the vortex line velocity. However, it should be kept in mind that the particle vortex interaction is quite complicated, and also depends on such factors as the relative motion between the particles, vortices, and normal fluid, and deformation of the tangle due to the presence of particles.

4.5 Chapter summary

A systematic study of solidified particle motion in He II thermal counterflow has been performed using the PTV technique. For the first time in a single experiment, the driving heat flux extends from the low range, previously investigated by PTV, to the high range, previously investigated by PIV. Demonstrating that the streamwise velocity PDFs transform from a double peak structure, with one peak centered at v_n and one near $v_n/2$, into a single peak centered near $v_n/2$, rectifies the previous experimental observations as well as predictions obtained through numerical simulations.

A set of simple criteria has been devised to isolate the normal fluid and vortex tangle velocity statistics. Application of the separation criteria shows that G1 velocity measurements dominate the non-classical tail structure of transverse velocity PDFs, while G2 velocity statistics exhibit more or less classical behavior. Furthermore, it is now possible to investigate root mean square velocity fluctuations of particles in each group. This investigation has suggested that large-scale turbulence is absent from the normal fluid in the two-peak regime, has already inspired additional research into the source of anisotropy in the normal fluid [113], and has linked G1 velocity fluctuations to fluctuations of the vortex tangle velocity.

The contents of this chapter have been peer-reviewed and appear in Physical Review Fluids [117].

CHAPTER 5

NEW APPLICATIONS FOR PTV IN THERMAL COUNTERFLOW

The previous chapter introduced a new technique for separately analyzing particles entrained by the normal fluid and those trapped on vortices. Usefulness of this technique was demonstrated by revisiting common anlyses of streamwise particle motion in response to increasing heat flux and transverse particle velocity PDFs, and showing that additional information can be uncovered when G1 and G2 are analyzed separately. This chapter explores the utility of PTV in conjunction with the separation scheme for characterizing thermal counterflow in ways that were not previously possible. In Sect. 5.1, acceleration along G1 tracks containing segments that contribute to transverse velocity PDF power law tails will be examined in an attempt to uncover the origin of the tails. In Sect. 5.2, G1 velocity fluctuations will be used to suggest that PTV can be used to provide spatially resolved experimental measurement of an important parameter related to energy dissipation in quantum and quasiclassical turbulence. In Sect. 5.3, the potential of G2 track length to indicate the mean free path of a particle traveling through the vortex tangle, and as an alternative means to obtain vortex line density, will be investigated.

5.1 Vortex reconnection and velocity PDF tails

Transverse particle velocity PDFs exhibiting $|u|^{-3}$ power law tails are commonly observed when PTV is applied to thermal counterflow in He II [105, 106]. As was shown in Sect. 4.3, these tails are due to G1. Two physical mechanisms could lead to the power law tails. For large values of the velocity, i.e. in the tail region, the PDF for the velocity field in the vicinity of a singular vortex is proportional to $|v|^{-3}$ [118]. Therefore the PDF for particles tracing the superfluid component in the vicinity of a quantized vortex should exhibit the power law tails. This explanation has been invoked on occasion to explain the observation of power law tails in transverse particle velocity PDFs [95, 105], but it is unlikely to be the correct interpretation, as solid particles tend to become trapped on vortices rather than respond to the superfluid [107, 108, 119].

Alternatively, when two vortices reconnect and separate from each other, the minimum separation distance δ grows in time as $\delta \propto |t - t_0|^{1/2}$, where t_0 is the time at which the reconnection occurs [60, 120]. The separation velocity is then proportional to $|t - t_0|^{-1/2}$, and the PDF should take a form proportional to $|u|^{-3}$. Since particles have a tendency to become trapped on vortices, this scaling should be reflected in the observed particle motion and velocity PDFs. Indeed, Paoletti et al. have shown through visualization of decaying counterflow that particle velocity PDFs take the $|u|^{-3}$ form, and they identified numerous pairs of particles moving away from each other with the separation distance growing as $|t - t_0|^{1/2}$ [106]. This is certainly a convincing link between vortex reconnection and velocity PDF power law tails, but no direct link was established between the pairs of particles and the tail region of the PDF.

With the separation scheme, such a link can be established by analyzing the kinematics of particles positively identified as both exhibiting G1 behavior and contributing to the transverse PDF tail region. Since this data comes from a steady-state counterflow with mean flow, acceleration along the tracks must be considered to remove the effects of the mean flow. Based on the $\delta \propto |t - t_0|^{1/2}$ scaling, acceleration along tracks containing a vortrex reconnection should be proportional to $|t - t_0|^{-3/2}$.

First G1 tracks containing a segment that contributes to the tail region of the G1 transverse velocity PDF are identified. As in Sect. 4.3, the tail region is defined as $|u_p| > \mu_u + 4\sigma_u$. Then the time and location of the supposed reconnection event is determined. As a first approximation, it is assumed that the reconnection occurs midway through the track segment that contributes to the PDF tail. It follows that the point at the beginning of the identified segment occurs at $t = t_0 - dt/2$, and the point at the end of the segment occurs at $t = t_0 + dt/2$ (dt is the image acquisition interval). Acceleration along the track as a function of elapsed time can then be calculated for particles accelerating away from (forward event) and towards (reverse event) the reconnection site. The acceleration magnitude $\|\mathbf{a}\|$ for each candidate track is then fit with a power law curve of the form

$$\|\mathbf{a}\| = C \, |t - t_0|^{-3/2} \tag{5.1}$$

where C is the fitting parameter. Figs. 5.1(a–c) show examples of G1 tracks, one for each temperature, that contribute to the transverse velocity PDF tail. The first point in each track is surrounded by a blue circle, and the high velocity segment that contributes to the tail region is identified with
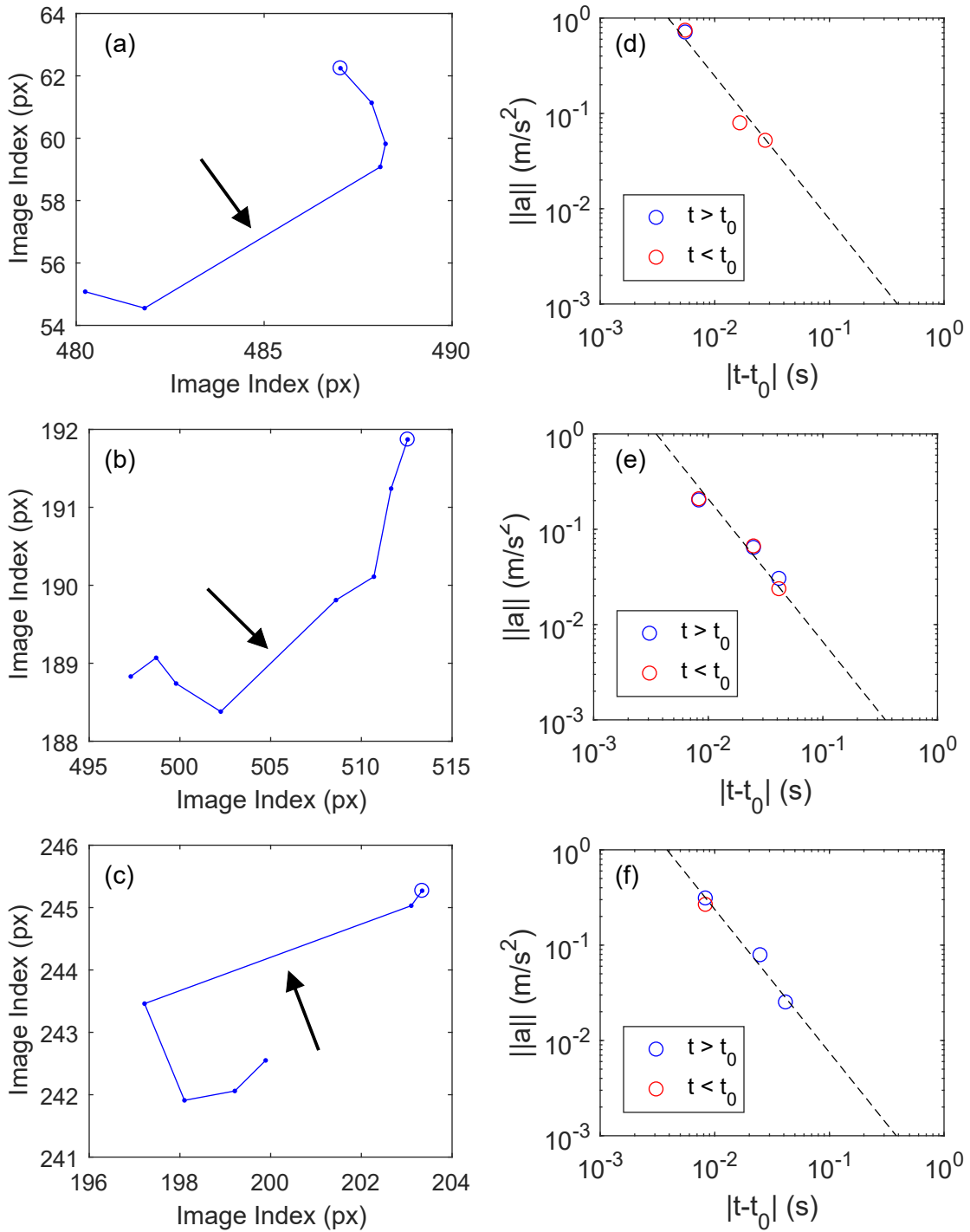
Figure 5.1: Selected G1 tracks that contribute to transverse PDF tails at (a) 1.70 K, (b) 1.85 K, and (c) 2.00 K, and (d)-(f) the corresponding acceleration along the tracks. Dashed lines represent Eqn. (5.1).

an arrow. In each of these tracks, there is a noticeable change in direction before or after the high velocity segment, indicative of vortex reconnection. Figs. 5.1(d–f) show the corresponding acceleration magnitudes along each track as a function of temporal separation from the reconnection event. Forward events are shown in blue and reverse events in red. The dashed line represents (5.1). In all three cases, acceleration along the track agrees remarkably well with the predicted $|t - t_0|^{-3/2}$ scaling. Interestingly, the fitting parameter is approximately the same in all three cases, having an average value of $C \approx 0.25$ mm/s$^{1/2}$ independent of temperature. This provides a positive link between transverse velocity PDF tails and vortex reconnection, since the G1 tracks that contribute to the tails obey the acceleration scaling extrapolated from the work of Paoletti et al. [106].

5.2   Experimental measurement of c_2

In Sect. 4.4, it was shown that G1 velocity fluctuations are to a large extent caused by fluctuations of the vortex line velocity. An expression for root mean square vortex line velocity fluctuation was given in Eqn. (4.4):

$$\langle v_L^2 \rangle^{1/2} \approx \frac{\kappa c_2 \gamma}{4\pi} \ln\left(\frac{\ell}{\xi_0}\right) \left(\frac{\rho}{\rho_s} v_n - v_0\right)$$

provided the counterflow velocity $\rho v_n / \rho_s$ exceeds v_0. To illustrate agreement with the G1 rms velocity fluctuations σ_{G1}, values for γ, v_0, and c_2 were borrowed from the recent work of Gao et al. [29, 115], and the mean line spacing ℓ was approximated across the entire parameter space. Since the agreement between σ_{G1} and $\langle v_L^2 \rangle^{1/2}$ appears to be reasonable, the measured G1 velocity fluctuations might be used in place of $\langle v_L^2 \rangle^{1/2}$, and Eqn. (4.4) used to estimate one of the other parameters. In particular, the value of c_2, the proportionality constant relating vortex line density to the mean line curvature, has been the subject of numerical [115, 116] and experimental study [121].

Energy dissipation in quantum turbulence, assuming that a random tangle of vortices exists without large-scale turbulence in the normal fluid, is described by a parameter χ_2, first introduced by Vinen in 1957 [20]. In quasiclassical turbulence, when the two fluids are coupled at scales exceeding ℓ [36], dissipation is governed by an effective kinematic viscosity ν' as proposed by Stalp et al. [31, 122]. Both dissipation parameters can be written in terms of c_2 [114]:

$$\chi_2 = \frac{1}{2}\alpha c_2^2 \ln \frac{\ell}{\xi_0} \tag{5.2}$$

68

and [115]

$$\nu' = \frac{\kappa\alpha}{16\pi^2}c_2^2 \ln^2 \frac{\ell}{\xi_0} \tag{5.3}$$

where α is a temperature-dependent mutual friction coefficient [44]. Numerical simulations producing a value for c_2 show that it depends on temperature [116] and perhaps also the specific form of the flow, in which case producing a reliable estimation of c_2 is still beyond the capabilities of numerical simulations [115], and the traditional second sound method provides averaged information across the measurement volume [121]. An experimental measurement of c_2, even if it applies only to flow in a square channel of 16 mm side length, would be a valuable step towards a complete understanding of dissipation in quantum turbulence, particularly if the measurements are spatially resolved.

Accepting the assumption that σ_{G1} represents $\langle v_L^2 \rangle^{1/2}$, reliable values for ℓ, γ, and v_0 must still be established. The normal fluid velocity v_n is easily obtained by knowledge of the experimental conditions through $v_n = q/\rho s T$, and the other terms in (4.4) are known constants. Each of ℓ, γ, and v_0 can be obtained by application of second sound attenuation to steady-state counterflow.

For each point in the counterflow parameter space, as well as the baseline (quiescent, $q = 0$) case for each temperature, a suitable second sound resonance peak was scanned 50 times. For each of the 50 baseline peaks, A_0 was determined by averaging the maximum values of the measured peaks, and Δ_0 was determined by linear interpolation between the points nearest the half-maximum
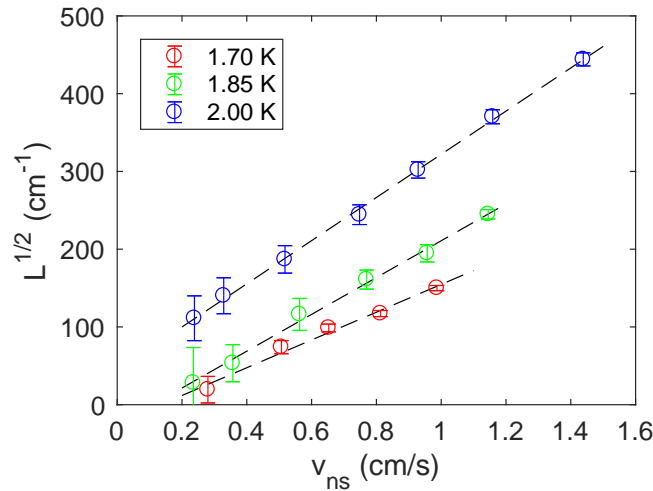

Figure 5.2: Square root of vortex line density as a function of steady-state counterflow velocity.

value. The attenuated amplitude A for each peak measured during steady-state counterflow was determined in a similar fashion. The resulting vortex line density is shown in Fig. 5.2, depicted by $L^{1/2}$ as a function of the steady-state counterflow velocity v_{ns}. Standard deviations of A_0, Δ_0, and A were propagated through Eqn. (1.9) to produce the error bars.

Calculation of the mean line spacing is trivial: $\ell = L^{-1/2}$. It is also straightforward to extract values of γ and v_0 for each temperature by fitting a first-order polynomial of the form $p_1 v_{ns} + p_0$ to the data of Fig. 5.2, as indicated by the dashed lines, where the first-order coefficient $p_1 = \gamma$ and the constant term $p_0 = \gamma v_0$, as per Eqn.(1.6). Fig. 5.3(a) shows the extracted γ-coefficient as a function of temperature, and Fig. 5.3(b) shows v_0. Error bars represent 95% confidence intervals for the linear fit. The numerical values are tabulated in Table 5.1. It is unclear why $v_0 < 0$ at 2.00 K.

Finally, values of c_2 can be extracted using the procedure illustrated in Fig. 5.4. Panels (a)–(c) show $\sigma_{G1} \ln^{-1} (\ell/\xi_0)$ as a function of $v_{ns} - v_0$ for $T = 1.70$, 1.85, and 2.00 K, respectively. The logarithmic term must be included in the dependent variable since it is a function of mean vortex line spacing, and by extension, indeed depends on the counterflow velocity. The dashed lines represent linear fits for which, according to Eqn. (4.4), the slope is $\kappa \gamma c_2/4\pi$. The values
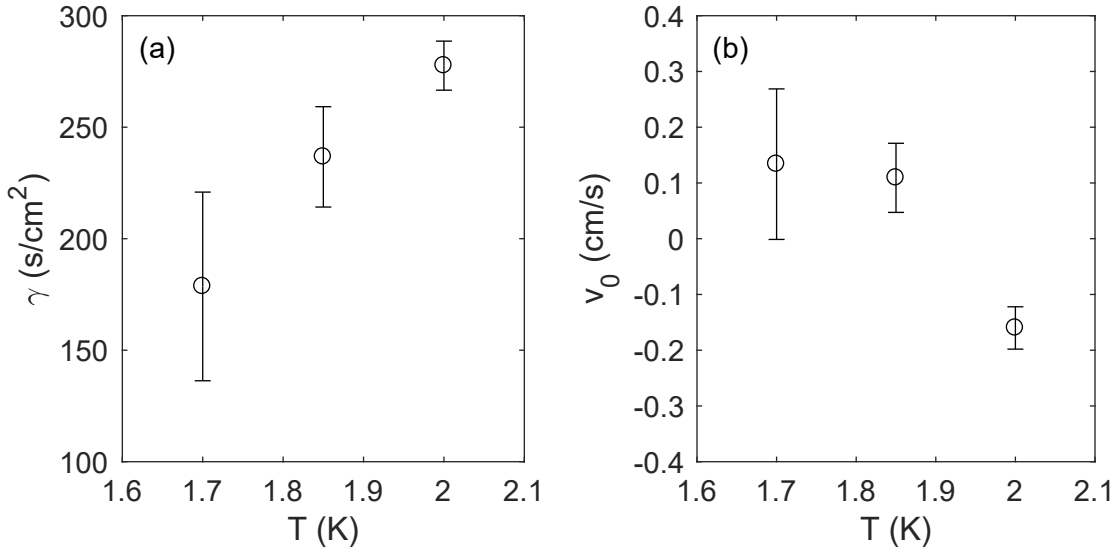

Figure 5.3: Calculated values for the γ-coefficient and v_0 as functions of temperature.
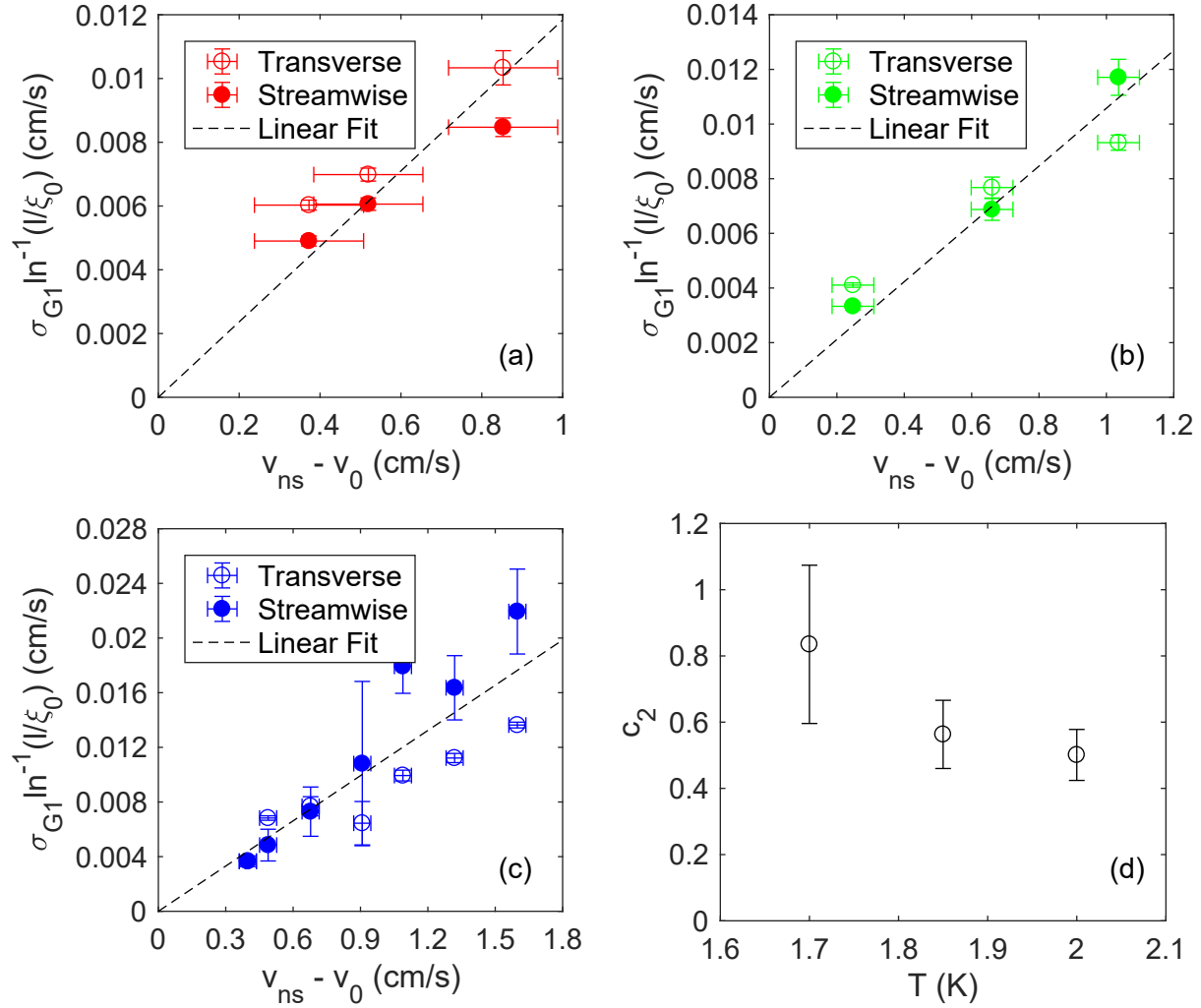
70

Figure 5.4: Linear fit to $\sigma_{G1} \ln^{-1}(\ell/\xi_0)$ as a function of $v_{ns} - v_0$ at (a) $T = 1.70$, (b) 1.85, and (c) 2.00 K. (d) Extracted values of c_2 as a function of temperature.

for c_2 required to produce the lines are shown in Fig. 5.4(d). They are slightly less than those reported in existing simulations [115, 116] and experiments [121], but the overall trend, a decrease with increasing temperature, is preserved. Geometric factors, i.e., the relatively large size of the experimental flow channel, may be partially responsible for the difference. It should also be kept in mind that while fluctuations of the local vortex line velocity play a large role in G1 velocity fluctuations, as shown in Sect. 4.4, they are not solely responsible; other factors, such as drag from the normal fluid, can also affect the G1 particle velocity [50, 51]. Nonetheless, the results

indicate that use of PTV to estimate c_2 is feasible, implying that the parameter can be spatially resolved by estimating its local value based on local G1 velocity fluctuations. Spatial resolution is of consequence for counterflow in which the normal fluid is laminar and the vortex tangle is not spatially uniform. Numeric values for c_2 are tabulated alongside γ and v_0 in Table 5.1.

Table 5.1: Measured values for the γ-coefficient and v_0.

T (K)	γ (s/cm^2)	v_0 (cm/s)	c_2
1.70	178.6 ± 42.3	0.134 ± 0.135	0.835 ± 0.239
1.85	236.7 ± 22.5	0.109 ± 0.062	0.563 ± 0.103
2.00	277.6 ± 11.0	-0.160 ± 0.038	0.501 ± 0.077

5.3   Mean free path and vortex line density

A persistent question throughout the discussion of G1 and G2 particle behavior is what causes particles to move under the influence of the normal fluid or vortex tangle in the first place. Many discussions on the behavior of particles in thermal counterflow mention particle size [48, 52, 103, 108]. With the separation scheme, the size distribution for particles contributing to G1 and G2 can be determined. Since particle size cannot be directly measured for a moving particle, the integrated light intensity, or m_0 from the tracking algorithm (see Sect. 3.3.3), is used as a substitute. Fig. 5.5 shows that the integrated light intensity PDFs for G1 and G2 are nearly identical across the full range of observed particle size, suggesting that for solidified tracer particles in the size range produced by the seeding system (see Sect. 3.3.1), the trapping probability is not influenced by particle size.

An alternative consideration is that at the beginning of the image acquisition, particles are either trapped or untrapped, and whether the G2 particles become trapped during the acquisition period depends primarily on their mean free path through the vortex tangle. As a very simple estimation, a particle might become trapped if the volume traversed by its trapping cross section contains a line segment comparable in length to the trapping cross section. A two-dimensional projection of the particle, $\pi d_p{}^2/4$, is used to represent the trapping cross section. The volume traversed by the cross section is then $s\pi d_p{}^2/4$, where s denotes the mean free path. Multiplication by L gives the vortex line length within this volume, and as per the estimation, the result must be
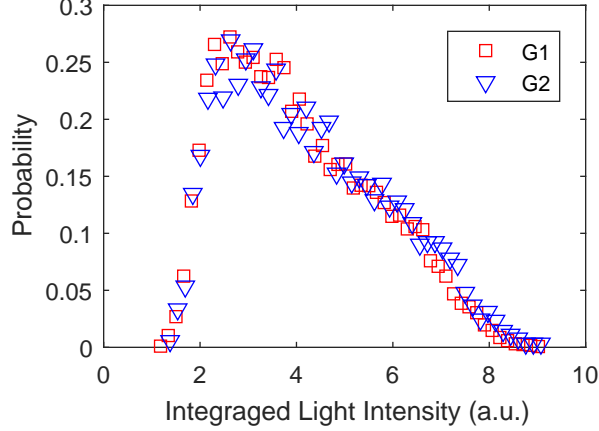
Figure 5.5: Probability distribution for the size (indicated by integrated light intensity) of particles contributing to G1 and G2 for the case where $T = 1.85$ K and $q = 38$ mW/cm^2.

less than d_p for the particle to remain untrapped:

$$\frac{\pi}{4}d_p{}^2 sL \leq d_p. \tag{5.4}$$

A simple representation for the mean free path is then

$$s \lesssim \frac{4}{\pi d_p L}. \tag{5.5}$$

As examples, consider the cases shown in Figs. 4.1(a) and (b) for which the temperature was 1.85 K and the heat flux was 38 and 122 mW/cm^2, respectively. The corresponding vortex line densities from Fig. 5.2 are $L = 2846$ cm^{-2} and $L = 59959$ cm^{-2}. For particles with diameter 4.6 μm, as per Fig. 3.8, the estimated mean free path is about 1 cm for case (a), and many of the G2 tracks are indeed of the order 1 cm. For case (b) the calculated mean free path is about 0.5 mm, and it can be seen that many of the G2 tracks, particularly the longer ones, are roughly 0.5 mm. Furthermore, in both cases, close inspection reveals that many of the tracks begin and end with G1 segments, which indicate interactions with the vortex tangle. Though this simple estimation is reasonably accurate, a proper determination of the mean free path requires complex numerical simulations, taking into account the complicated dynamics of He II, such as Kelvin waves on quantized vortices, drag force exerted by the normal fluid, and relative motion of the particles and vortex tangle. Similar simulations by Kivotides indeed show that when the vortex tangle is relatively sparse, particles can move a significant distance (in some cases throughout the entire

73

computational domain) without interacting with vortices [50], but when the tangle is relatively dense the particles experience constant interaction with the tangle [104].

To truly judge the accuracy of the mean free path approximation, the mean length of observed G2 tracks could be used to represent s, and the quantity $(\pi d_p s/4)^{1/2}$ compared to the mean line spacing, $\ell = L^{-1/2}$. Ideally, the ensemble of measured G2 track lengths should have a Gaussian distribution centered at the mean free path of a particle through the vortex tangle. The PDF for G2 track length as observed at $T = 2.00$ K, $q = 40$ mw/cm^2 is shown in Fig. 5.6.

Clearly, the observed track lengths do not exhibit the ideal Gaussian distribution; the PDF does not even have a symmetric shape with a clear mean value. However, for 2D planar velocimetry, this is to be expected. G2 tracks begin and end for reasons other than de-trapping or trapping events. Particles tracing the normal fluid are free to enter and leave the imaging plane through the top or bottom of the image as well as by drifting in- or out-of-plane in the direction normal to the camera, leading to the observation of tracks that are shorter than the mean free path. Conversely, it is not possible to observe a track longer than the mean free path (at least, not much longer). Therefore, instead of estimating s with the mean G2 track length, it will be estimated with the mean length of the longest 10% of observed G2 tracks.
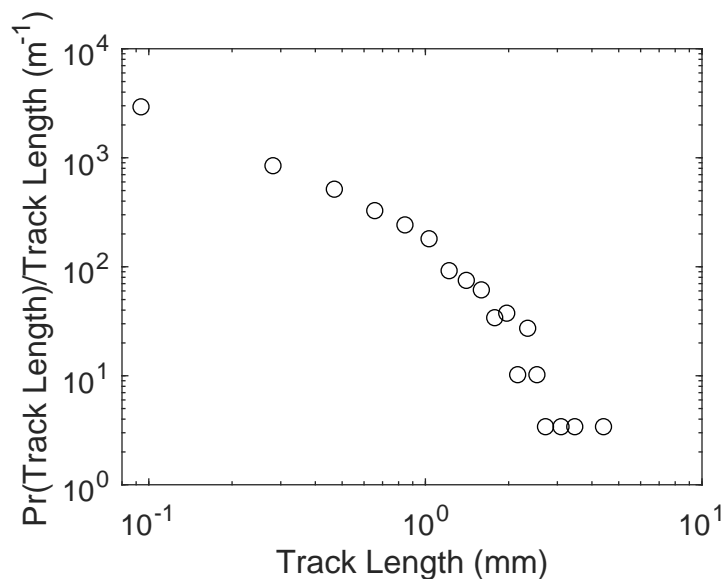

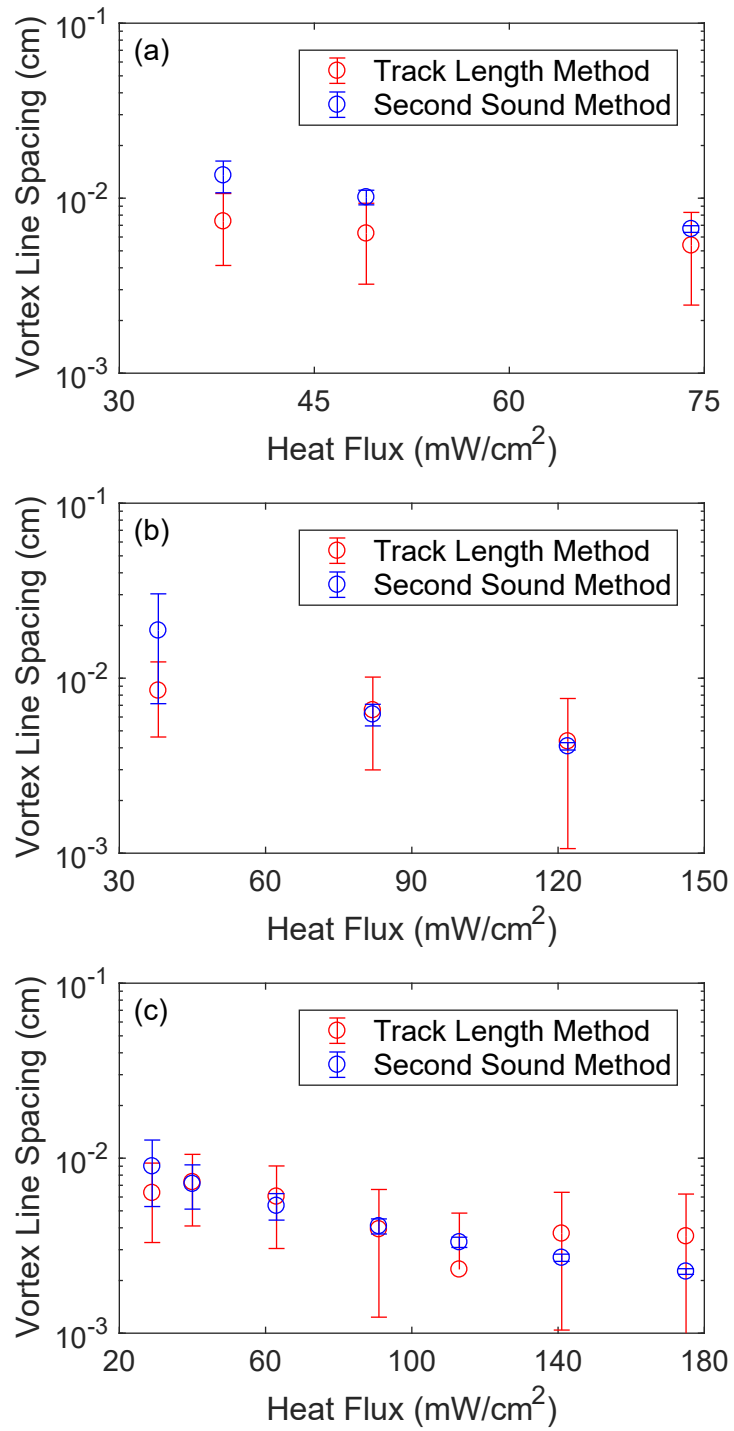Figure 5.6: G2 track length PDF at $T = 2.00$ K, $q = 40$ mW/cm2.

Figure 5.7: Prediction of mean vortex line spacing using G2 mean free path model and traditional second sound attenuation for (a) $T = 1.70$ K, (b) $T = 1.85$ K, and (c) $T = 2.00$ K.

Fig. 5.7 shows the mean vortex line spacing as a function of heat flux for (a) 1.70 K, (b) 1.85 K, and (c) 2.00 K. The red markers predict ℓ using the mean free path model, where the longest 10% of G2 tracks observed for each point in the parameter space represent s and $d_p = 4.6 \pm 1.3$ μm. Standard deviations for s and d_p were propagated through Eqn. (5.5) to produce the error bars. The blue markers represent the line spacing obtained from second sound attenuation as discussed in Sect. 5.2 and shown in Fig. 5.2.

For a simple approximation, the accuracy is remarkable, but the assumption that G2 track lengths represent the mean free path should be approached with caution, since it does not account for the possibility of a mean vortex tangle drift. If the vortex tangle drifts at v_s, for example, in the direction opposite the particle motion, the true mean free path between vortices is longer than the observed G2 track length by a factor of ρ/ρ_s. Though some experiments, including this one, suggest that the mean drift velocity is indeed similar to v_s for small enough heat flux [52, 109], others suggest that the tangle moves in the direction of the normal fluid [123], or does not move at all [124]. It is therefore not clear what correction factor should be applied to Eqn. (5.5) to account for the drifting tangle. In any case, for higher heat flux when the tangle is relatively dense and the normal fluid carries particles quickly between vortex lines, the correction is likely to be negligible. However, the inclusion of ρ/ρ_s for lower heat flux may be necessary, as shown by the larger discrepancy between line spacing measured by second sound attenuation and the mean free path model for lower heat flux in Fig. 5.7. The results presented here still show strong validity of the mean free path model, and further suggest that flow visualization using PTV, together with the separation scheme, may be a potential alternative to second sound attenuation for estimation of vortex line density in steady-state thermal counterflow.

5.4 Chapter summary

The separation scheme for separately analyzing particle entrained by the normal fluid and those trapped on quantized vortices has led to three noteworthy observations. Vortex reconnection has been positively linked to particle velocity PDF power law tails by showing that acceleration along G1 tracks that contribute to the tails follows the predicted scaling for vortices accelerating away from a reconnection site. G1 rms velocity fluctuations have been used to experimentally estimate the value of c_2, an important parameter related to dissipation of turbulent energy in He II. Finally,

a simple but remarkably accurate model for the mean free path of particles traveling through the vortex tangle relates G2 track length to mean vortex line spacing, providing a new way to estimate VLD in steady-state thermal counterflow.

Some of the contents of this chapter have been peer-reviewed and appear in Physical Review Fluids [117]. Submission of the remaining materials to the Physical Review is pending.

CHAPTER 6

GRID TURBULENCE

In this chapter, the capability of the apparatus described in Chapter 2 to visualize towed-grid turbulence in He II will be demonstrated by presentation of the preliminary grid turbulence data set, which includes systematic measurements of both second sound attenuation and particle motion in the wake of the grid. Though detailed analysis of this data will be left to future work, a clear link will be established between the PTV data and the measurements it enables, such as reliable estimation of the effective kinematic viscosity and computation of both transverse and longitudinal structure functions and characteristics of the flow derived from them.

6.1 Background and motivation

In 1999, the groundbreaking He II decaying grid turbulence experiment conducted by Stalp et al. [31] led Vinen to propose that grid turbulence in He II is quasiclassical in nature, or that it exhibits the characteristics of classical turbulence on length scales exceeding the mean vortex line spacing due to coupling of the two fluids by mutual friction [36]. Stalp et al. proposed a model for the energy spectrum $E(k,t)$, which describes the kinetic energy concentrated in eddies of spacial frequency, or wave number, k, for HIT in a finite channel that decays over time. In their model, the energy-containing length scale $l_e = 2\pi/k_e$ grows over time, until it becomes saturated by the size of the channel at $t = t_s$. Assuming that the energy spectrum exhibits the classical Kolmogorov form in the inertial sub-range $k_e \leq k \leq k_\eta$, where k_η corresponds to the Kolmogorov scale at which viscous dissipation truncates the spectrum, they show that the total energy density decays as $E \propto t^{-6/5}$ for $t \leq t_s$ and gradually transitions [125, 126] to $E \propto t^{-2}$ for $t \geq t_s$. For HIT, the energy density and vorticity are related by the expression

$$\frac{dE}{dt} = -\nu \left\langle \omega^2 \right\rangle, \tag{6.1}$$

where ω represents vorticity [67]. Based on this expression and the anticipated energy decay rates, the predicted vorticity decay rates are $\omega \propto t^{-11/10}$ for $t \leq t_s$ and $\omega \propto t^{-3/2}$ for $t \geq t_s$.

Stalp et al. make the further assumption that vorticity in the superfluid is related to the vortex line density, $\omega = \kappa L$, so that the expression

$$\frac{dE}{dt} = -\nu' \left(\kappa L \right)^2 \tag{6.2}$$

is analogous to Eqn. (6.1), but includes an effective kinematic viscosity ν' that accounts for viscous dissipation in the normal fluid as well as interaction of the two fluids through mutual friction [122]. Accepting this assumption, it follows that the vortex line density should decay at the same rate as predicted for vorticity in classical HIT. It was indeed shown that vortex line density decays as $t^{-11/10}$ before transitioning to $t^{-3/2}$ [31, 126], and the effective kinematic viscosity was evaluated across a broad temperature range [122]. While strong agreement between the theoretical model and experimental results gives merit to the former, direct experimental verification of the assumptions involved can be obtained by repeating the experiments, but adding flow visualization as a diagnostic tool.

6.2   Preliminary data

The experimental apparatus described in Chapter 2 is capable of measuring towed-grid turbulence spanning a large parameter space, with temperatures down to $T \approx 1.2$ K, grid speeds up to $v_g = 60$ cm/s, and grid mesh sizes $M = 3$, 3.75, and 5 mm. Thus far, systematic data acquisition has been accomplished at temperatures of $T = 1.65$, 1.95, and 2.12 K, corresponding to superfluid density fractions of $\rho_s/\rho \approx 80\%$, 50\%, and 20\%, respectively. Grid speeds of 15, 30, and 60 cm/s were covered at $T = 1.65$ and 1.95 K, but v_g was limited to 30 cm/s at 2.12 K. All data was obtained using the $M = 3$ mm grid.

6.2.1   Second sound attenuation

Using the procedure outlined in Sect. 3.2.3, vortex line density as a function of time in decaying towed-grid turbulence has been measured for three grid speeds, $v_g = 15$, 30, and 60 cm/s. For second sound measurements, the temperature was limited to 1.65 K, at which the second sound velocity does not vary much with temperature (see Fig. 1.3). Fig. 6.1 shows the averaged vortex line density for each of the three grid speeds over a decay period of 100 s.

The dashed and solid lines indicate decay rates of $t^{-11/10}$ and $t^{-3/2}$, respectively. They appear to fit the data well for all three grid speeds, but whether the fits are appropriate is better determined
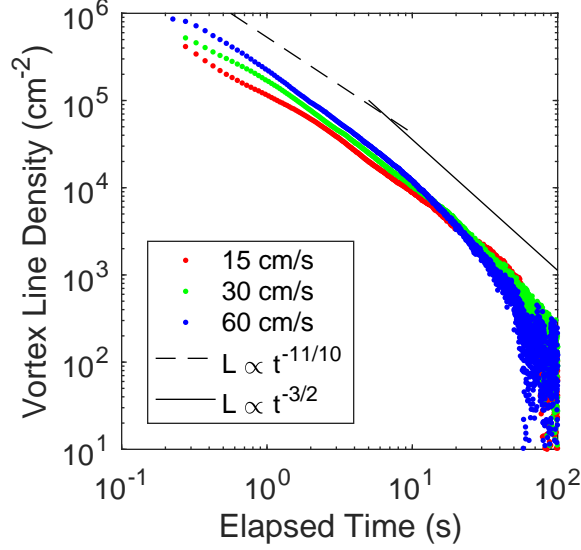
Figure 6.1: Vortex line density in decaying grid turbulence at 1.65 K (3 mm grid mesh size).

by the ratio of measured line density to the proposed decay rate. For example, where $L(t)$ decays as $t^{-3/2}$, $Lt^{3/2}$ should be a flat curve [125, 126]. In Fig. 6.2(a) and Fig. 6.2(b), the measured line density is compared with decay rates of $t^{-11/10}$ and $t^{-3/2}$, respectively.

The compensated curves of Fig. 6.2(a) are relatively flat, indicating that the $t^{-11/10}$ decay rate leading up to saturation of the energy-containing length scale by the channel size is probably a good fit. However, those of Fig. 6.2(b) are not quite flat, indicating that the raw data probably does not decay as $t^{-3/2}$ after saturation.

There are two ways to recover a plateau in the compensated curves. One is to examine whether the raw data follow different power laws. Fig. 6.2(c) and Fig. 6.2(d) show that comparing L to $t^{-6/5}$ and t^{-2}, respectively, produces remarkably flat regions. Though these decay rates do not correspond with those predicted for vorticity in HIT, it is interesting that they correspond to another physical quantity: the predicted energy decay rates. However, such observations are not accepted by the He II research community.

Alternatively, flatness in the compensated curves can be obtained by introducing a virtual time origin, t_0, such that $L \propto (t + t_0)^n$, where n is the desired decay rate. In other words, t_0 is a fitting parameter that can be adjusted until the data show the desired results [125]. This is the method typically accepted in the quantum turbulence community. Fig. 6.3 shows that, indeed, $L(t - t_0)^{3/2}$
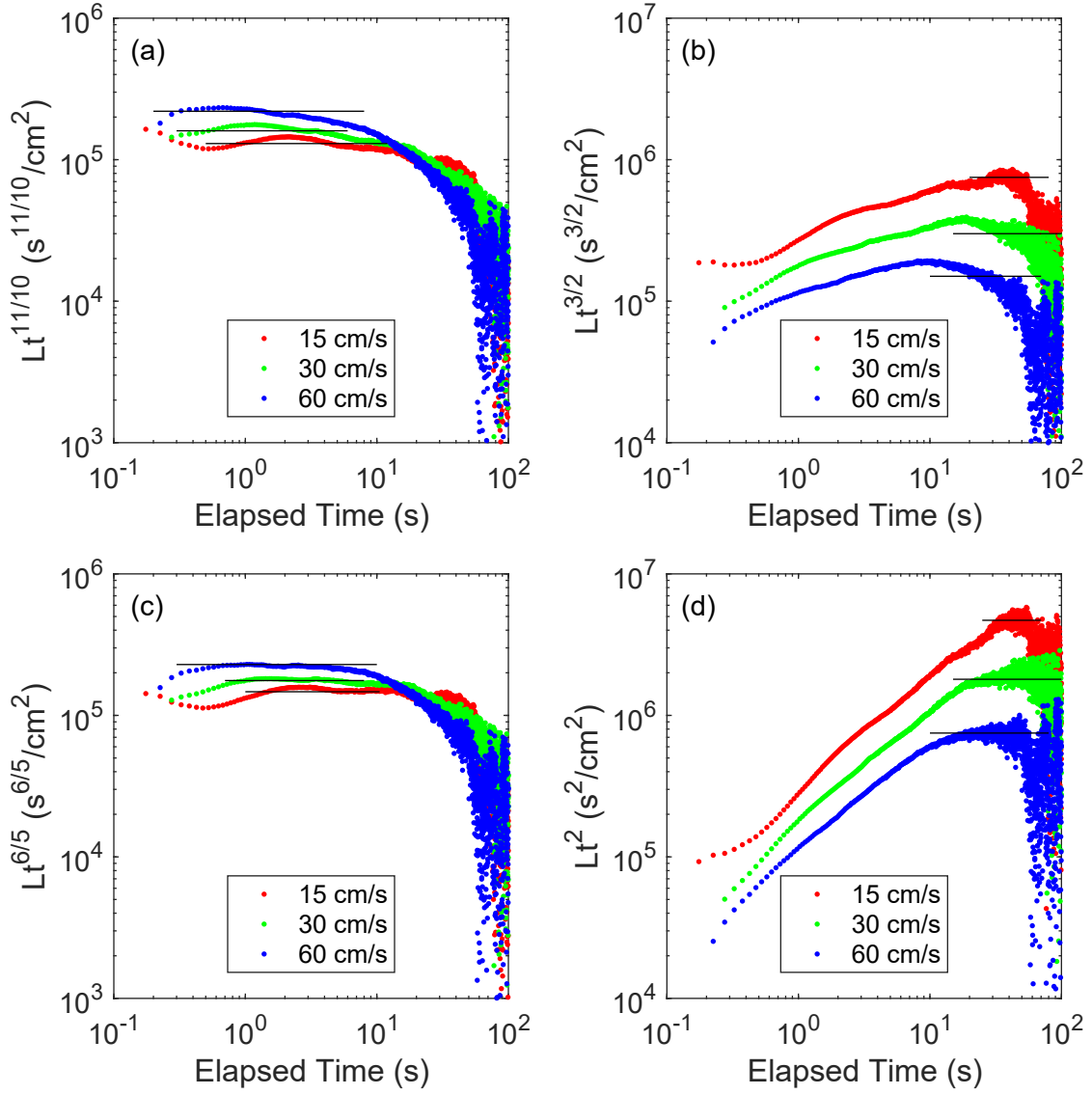
Figure 6.2: Vortex line density compensated by decay rates (a) $t^{-11/10}$, (b) $t^{-3/2}$ (data are shifted vertically for clarity), (c) $t^{-6/5}$, and (d) t^{-2} (data are shifted vertically for clarity). Black horizontal lines are included for reference.
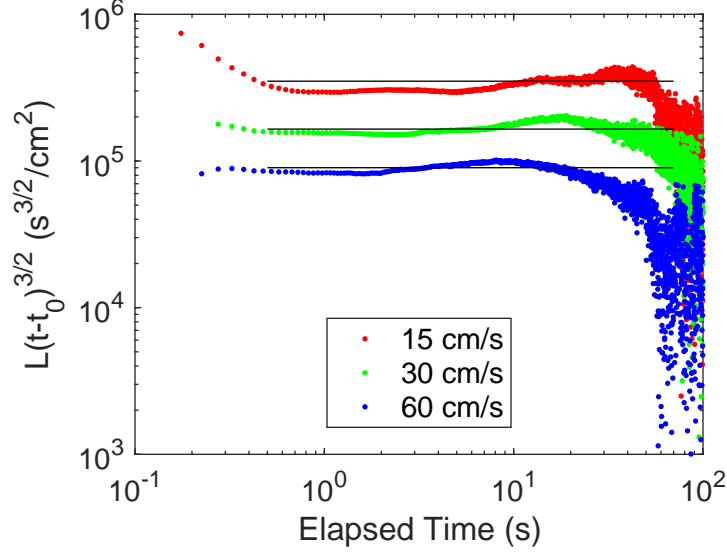
Figure 6.3: Vortex line density compensated by $(t + t_0)^{-3/2}$ (data are shifted vertically for clarity). Black horizontal lines are included for reference.

produces more or less flat curves throughout the decay if $t_0 = 0.8$, 0.5, and 0.3 s for grid speeds $v_g = 15$, 30, and 60 cm/s, respectively. With this adjustment, it can be claimed that the second sound data agree with existing literature.

6.2.2 Particle tracking velocimetry

For each point in the parameter space, the PTV procedure described in Sect. 3.3 was repeated several times, resulting in several hundred short videos of particle motion throughout the turbulence decay period. To represent the data graphically, the rms velocity fluctuation, defined as

$$u_{rms} = \left\langle (u - \langle u \rangle)^2 \right\rangle^{1/2} \tag{6.3}$$

in the transverse direction (perpendicular to the grid motion) and

$$v_{rms} = \left\langle (v - \langle v \rangle)^2 \right\rangle^{1/2} \tag{6.4}$$

in the axial direction (parallel to the grid motion), was determined at each 2 s time interval throughout the decay. In Eqns. (6.3) and (6.4), u and v represent a particle velocity measurement in the transverse and axial directions, respectively, and $\langle \dots \rangle$ denotes an ensemble average. Fig. 6.4(a)
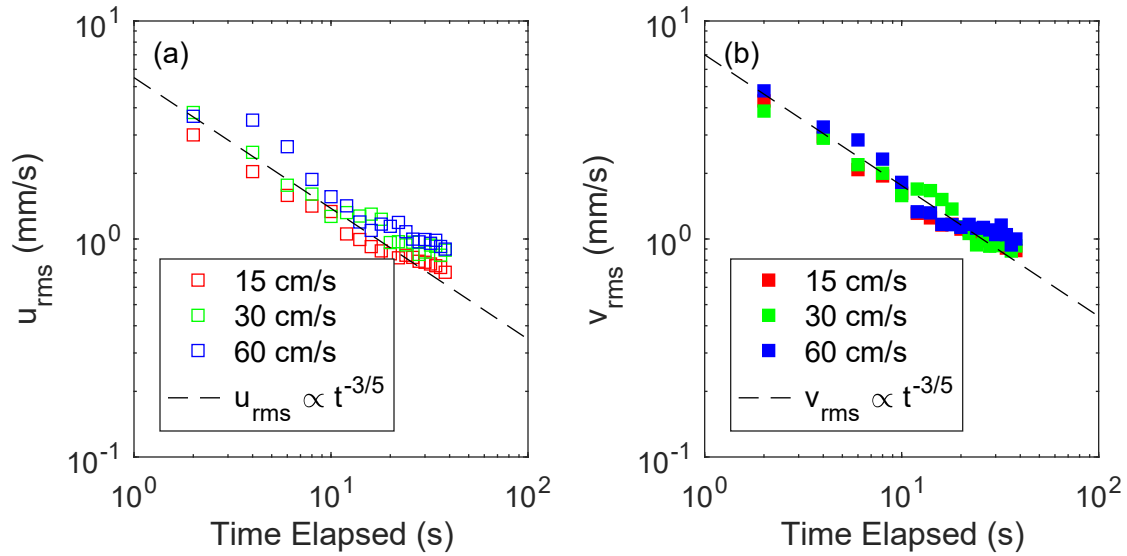
82

Figure 6.4: Root mean square velocity fluctuations in the (a) transverse and (b) axial directions for all three grid speeds at 1.95 K.

shows u_{rms} as a function of decay time for all three grid speeds at 1.95 K, and Fig. 6.4(b) shows the same for v_{rms}.

According to the theory of Stalp et al., energy content of the bulk fluid should decay as $t^{-6/5}$ before the energy-containing eddy size becomes comparable with the channel size, and then as t^{-2} after saturation [31]. Since the kinetic energy density is proportional to the mean-square velocity fluctuation, the predicted evolution for rms fluctuation is $t^{-3/5}$ and t^{-1}. As shown by the dashed lines of Fig. 6.4, both u_{rms} and v_{rms} decay as $t^{-3/5}$ for the first several seconds. However, in the range of 10–20 s, instead of increasing to t^{-1}, the decay rate decreases. A number of stray effects, including thermal counterflow from remnant heating [127] or surface waves induced by the linear drive shaft, may be responsible.

The data can also be presented for all three temperatures at constant grid speed, as is the case for u_{rms} and v_{rms} in Fig. 6.5(a) and Fig. 6.5(b), respectively. While the initial decay as $t^{-3/5}$ is preserved for all three temperatures, a noticeable feature is the apparent increase of u_{rms} and v_{rms} in the late decay regime for 1.65 K. This is likely an artificial effect caused by the particle delivery tube. When the tube suddenly breaks the free surface of the liquid helium bath as the linear drive shaft moves upward, it may introduce surface waves in the reservoir, the effects of which could
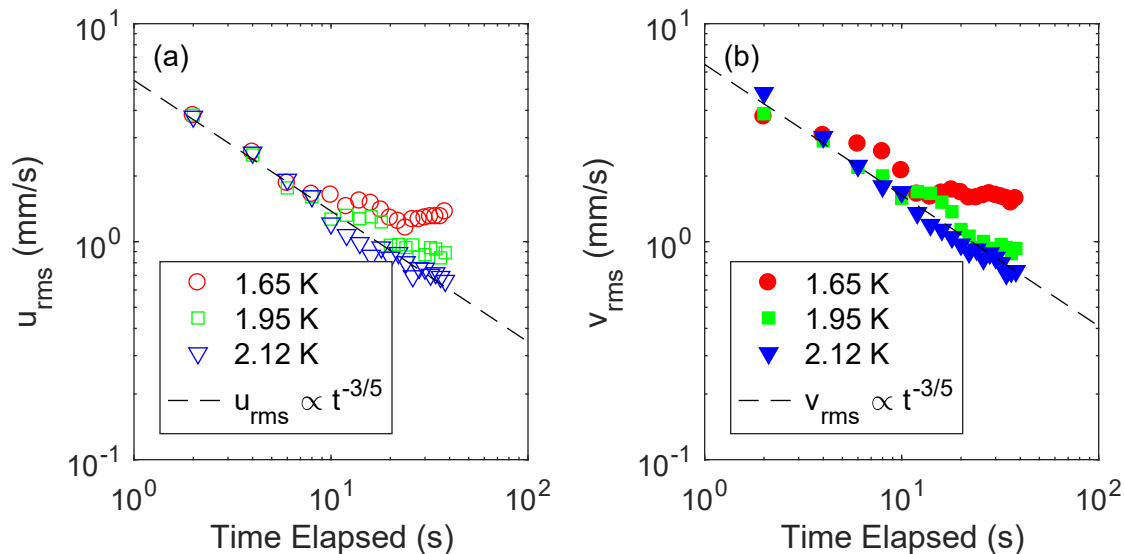
Figure 6.5: Root mean square velocity fluctuations in the (a) transverse and (b) axial directions for all three temperatures at $v_g = 30$ cm/s.

be felt in the channel. Surface waves appear in the bulk fluid as circular motion [128], consistent with the observed increase of rms velocity in both directions. No such increase is observed for $T = 1.95$ K or $T = 2.12$ K, though the higher normal fluid content at these temperatures may quench the wave motion before it reaches the imaging region. If this is the case, it is a design flaw inherent to the particle delivery system and not easily corrected. Fortunately, a considerable amount of information can still be extracted from the PTV data.

6.3   Effective kinematic viscosity

In their original calculation of the effective kinematic viscosity based solely on measurements of second sound attenuation in towed grid turbulence [122], Stalp et al. relied on two significant assumptions: that the size of the energy-containing eddies eventually becomes saturated by the channel size, and that the coupled turbulence exhibits a classical Kolmogorov energy spectrum on all length scales. However, these assumptions may not be appropriate [65, 129]. As Gao et al. have recently pointed out, measurements of the vortex line density as well as the energy content of the coupled fluid are necessary for reliable estimation of the effective kinematic viscosity [65]. They propose two contributions to the total kinetic energy density E in turbulent He II. The contribution

from individual vortex lines on scales at or below the mean line spacing ℓ, represented by E_1, is given by

$$E_1 = \frac{\kappa^2}{4\pi} \frac{\rho_s}{\rho} \ln \left(\frac{\ell}{\xi_0} \right) L, \tag{6.5}$$

while the contribution from coupled turbulence in the bulk fluid, represented by E_2, is given by

$$E_2 = \frac{3}{2} u_{rms}^2 = \frac{3}{2} v_{rms}^2. \tag{6.6}$$

The use of either u_{rms} or v_{rms} to represent the velocity fluctuation in all three spatial directions relies on the assumption that turbulence in the coupled fluid is isotropic, a reasonable assumption based on the similar decay behaviors exhibited in Figs. 6.4 and 6.5. Accepting the relationship between energy density and vortex line density given in Eqn. (6.2) and inserting the expressions for E_1 and E_2 yields

$$\frac{\kappa^2}{4\pi} \frac{\rho_s}{\rho} \ln \left(\frac{\ell}{\xi_0} \right) \frac{dL}{dt} + 3u_{rms} \frac{du_{rms}}{dt} = -\nu' \left(\kappa L \right)^2. \tag{6.7}$$

Besides ν', the contents of Eqn. (6.7) are either known constants, known functions of temperature, or experimentally measured quantities. In particular, the line density L and spacing ℓ can be obtained from second sound attenuation, and the rms velocity fluctuation u_{rms} (or v_{rms}) from PTV, as clearly exhibited in Sect. 6.2.

Gao et al. have applied this method to decaying thermal counterflow turbulence, which exhibits quasiclassical behavior in the late decay regime [36, 65], and found values for ν' that indeed differ from those originally reported by Stalp et al. [122]. However, this method for determining ν' has not yet been applied to towed-grid turbulence. Since this parameter governs the decay of quasiclassical turbulence, and is vital to the application of He II to high-Re fluid dynamics, the method of Gao et al. and the grid turbulence data collected for this work will be combined to produce reliable measurements of ν' in decaying grid turbulence.

6.4 Structure functions

The nth-order longitudinal structure function $S_n^{\|}(r)$ is given by

$$S_n^{\|}(r) = \left\langle \left| v_{\|}(\mathbf{x} + \mathbf{r}) - v_{\|}(\mathbf{x}) \right|^n \right\rangle, \tag{6.8}$$

where $v_{\|}$ is the magnitude of the local velocity in the direction parallel to the vector $\mathbf{r}$ drawn between two locations $\mathbf{x}$ and $\mathbf{x} + \mathbf{r}$. Likewise, the nth-order transverse structure function $S_n^{\perp}(r)$ is

given by

$$S_n^\perp (r) = \langle |v_\perp (\mathbf{x} + \mathbf{r}) - v_\perp (\mathbf{x})|^n \rangle . \tag{6.9}$$

Though particle tracking is essentially a Lagrangian technique, the particle seeding density and distribution in each image is such that reliable calculations of the structure functions can still be obtained. For a successive pair of images, the velocity differences between each pair of particles, with one located at $\mathbf{x}$ and the other at $\mathbf{x} + \mathbf{r}$, can be used to build the structure functions. Since the particles are not evenly spaced, the resulting velocity increments will need to be sorted into discretized bins based on their separation distance r. This approach is based on the assumption that the turbulent flow field does not evolve much in the time separating the two images, which is probably a fair assumption. Larger ensembles can be generated to produce more reliable structure functions if it is further assumed that the energy does not decay significantly in the 0.2 s time window of each video. Each successive pair of images in the sequence can be used, and the result will be transverse and longitudinal structure functions of any order for each 2 s decay interval.

6.4.1 Energy spectrum

The second-order structure function is linked to the one-dimensional energy spectrum through the velocity autocorrelation. Expanding the expression for a second-order structure function, in the longitudinal direction for example, and rearranging the terms results in

$$R_\| (r) = \langle v_\| (\mathbf{x}) \, v_\| (\mathbf{x} + \mathbf{r}) \rangle = v_{rms}^2 - \frac{1}{2} S_2^\|, \tag{6.10}$$

where $R_\| (r) = \langle v_\| (\mathbf{x}) \, v_\| (\mathbf{x} + \mathbf{r}) \rangle$ is the autocorrelation of $v_\|$. As a note in passing, just about anything can be used for the mean-square velocity that appears in Eqn. (6.10). Since towed-grid turbulence is homogeneous and isotropic, u_{rms} or v_{rms} from Sect. 6.2.2 would both be appropriate. Alternatively, $R_\| (r)$ could be calculated directly, with no need to first determine $S_2^\|$.

The one-dimensional energy spectrum is given by the Fourier transformation of the autocorrelation [128],

$$E_\| (k) = \frac{1}{2\pi} \int\limits_{-\infty}^{\infty} e^{-ikr} R_\| (r) \, dr, \tag{6.11}$$

and the three-dimensional spectrum by [67]

$$E (k) = k^3 \frac{\partial}{\partial k} \left(\frac{1}{k} \frac{\partial E_\|}{\partial k} \right) . \tag{6.12}$$

Structure functions such as $S_2^{\parallel}(r)$ (or, equivalently, $S_2^{\perp}(r)$ or $R_{\parallel}(r)$ or $R_{\perp}(r)$) are closely related to the energy spectrum, and can be readily obtained at 2 s intervals throughout the first 40 s of the turbulence decay. By extension, the flow visulaization data provides reliable information about time evolution of the energy spectrum in decaying towed-grid turbulence.

6.4.2 Intermittency

Structure functions are expected to scale as

$$S_n(r) \propto r^{\varsigma_n}, \tag{6.13}$$

where the scaling exponent $\varsigma_n = n/3$ [67]. In cases where the turbulence is intermittent, or the velocity field exhibits rare large-scale anomalies, the scaling exponents for higher-order structure functions depart from Eqn. (6.13). Such intermittence and its temperature dependence, if any, is a topic of open debate in quasiclassical turbulence. Recent numerical work that points to temperature-dependent intermittency enhancement [39, 130] is both refuted [40] and supported [127] by experimental investigations. The large parameter space covered by this work, and the capability to directly compute the velocity structure functions based on PTV data, offers additional insight into the structure function scaling and intermittency enhancement. As an alternative to direct computation if the velocity sample sizes are not large enough to resolve the rare intermittent events, structure function scaling can be obtained through the extended self-similarity hypothesis [131], which predicts that the nth-order structure functions scale as $S_3(r)^{\varsigma_n}$, and has been applied to successfully predict the scaling exponent based on measured third-order structure functions in He II turbulence [127].

6.5 Chapter summary

New flow visualization data showing the decay of turbulence in the wake of a $M = 3$ mm grid pulled at speeds of $v_g = 15$, 30, and 60 cm/s through He II at temperatures of 1.65, 1.95, and 2.12 K have been produced. Additionally, using the same apparatus, attenuation of second sound has been measured for 100 s of the decay at all three grid speeds and $T = 1.65$ K. These data sets enable critical measurements of the characteristics of quasiclassical turbulence, such as a reliable estimation of the effective kinematic viscosity and velocity structure functions, which are closely related to the energy spectrum and intermittency of the coupled turbulence.

CHAPTER 7

CONCLUDING REMARKS

Application of both second sound attenuation and particle tracking velocimetry to thermal counter-flow and towed-grid turbulence in He II, an unprecedented approach to He II turbulence research, has been enabled by development of a new state-of-the-art experimental facility. Data covering a wide parameter range have been systematically collected for both thermal counterflow and towed-grid turbulence. Analysis of the counterflow data have led to a number of insights about quantum turbulence, vastly increasing the utility of PTV as a quantitative measurement tool for thermal counterflow, and future analysis of the grid turbulence data will likely have the same impact. Furthermore, the equipment and methods developed have additional potential beyond the applications explored in this work.

7.1   Contributions of this work

The key contribution from the work on thermal counterflow is the separation scheme. Differentiating particles entrained by the normal fluid (G2) from those trapped on quantized vortices (G1) allows statistics of the two groups to be investigated separately, and has enabled measurements of thermal counterflow that were previously inhibited by the particle motion ambiguity.

1. By covering a wide range of applied heat flux in a single experiment, a long-standing discrepancy over the relationship between v_p and v_n has been solved. Though theoretical and numerical work has already proposed that two regimes for particle behavior exist and are distinguished by the applied heat flux [53], this work provides experimental verification that particles—at least those entrained by the normal fluid—move at v_n for relatively low heat flux, while all particles move at roughly $v_n/2$ for relatively high heat flux.

2. The separation scheme immediately revealed that some information is missed when the two groups are analyzed together, for example, power-law tails in the particle velocity PDFs are due entirely to G1.

3. Using the separation scheme to measure acceleration along G1 tracks that contribute to the PDF power law tails, a direct link was established between vortex reconnection and the power law tails.

4. Using the separation scheme, G1 velocity fluctuations were linked to fluctuations in the local vortex line velocity, and the link can be used to make the first experimental measurement of c_2, an important parameter related to energy dissipation in both quantum and quasiclassical turbulence [115].

5. Using the separation scheme to measure the length of G2 tracks, a model for the mean free path of particles through the vortex tangle was established and used to estimate, with remarkable accuracy, the mean spacing between vortex lines, suggesting that G2 track length may be an alternative to second sound attenuation for measurement of vortex line density.

For decaying grid turbulence in He II, access to velocity fluctuations of the turbulent flow field, which essentially represent the kinetic energy content of the coupled turbulence, opens the door to several new measurements.

1. Using the visualization data in conjunction with second sound attenuation data will provide a more accurate measurement of ν' than was possible in the original towed-grid turbulence experiments, which used second sound alone [65, 122].

2. Velocity structure functions can be computed based on the measured particle velocity, providing insight about the evolution of the energy spectrum in He II decaying grid turbulence, which was previously based on assumptions [31].

3. Intermittency in quasiclassical turbulence and its temperature dependence, which is a currently contested topic in He II research [39, 40, 127, 130], can also be evaluated using the velocity structure functions.

Though analysis of the grid turbulence data is left for future work due to extensive investigations of thermal counterflow, these first-of-their-kind data promise to yield important new quantitative characteristics of quasiclassical turbulence that move towards the use of He II for high-Re fluid dynamics applications.

7.2   Suggestions for future work

For thermal counterflow, one possible future direction is to study the structure and scaling laws of PDFs related to the trajectory geometry, instead of the particle kinematics. This approach to Lagrangian fluid dynamics has recently emerged in classical fluids, where curvature of the trajectories [132] or the relative angle of velocity vectors as a function of their temporal separation along the track [133] are used to characterize the fluid dynamics. Applications to simulations of classical

turbulent flows have revealed power law scaling of the PDFs for trajectory angle [134], curvature, and torsion [134, 135] that characterize the turbulence. This approach has not yet been introduced to quantum turbulence, and may offer an opportunity for quantitative characterization of the vortex tangle dynamics in thermal counterflow [136]. With the separation scheme introduced in this work, particles tracing the vortex tangle (G1) can be identified and used for such analysis.

The most obvious path forward for the grid turbulence experiment is to systematically increase the parameter space covered by the flow visualization and second sound data. An easy approach is to change the grid size. Grids with larger mesh size, $M = 3.75$ mm and $M = 5$ mm, have already been produced, but have not yet been used for the experiment. A more difficult, but still necessary, approach is to develop a second sound data acquisition method that can be used successfully for transient flow at a wide range of He II temperatures. The frequency sweep method used for this work is limited to temperatures near 1.65 K, where temperature fluctuations in the liquid helium bath do not have much affect on the second sound velocity. One attractive solution is the resonant frequency tracking amplifier designed by Yang et al., a closed-loop feedback system that always oscillates at the channel resonant frequency, even if it fluctuates with temperature [93]. This solution should be adapted with caution, as it is not clear whether the loop oscillation frequency is controlled by the second sound resonant frequency or by compensations for frequency-dependent phase shifts in other equipment that comprises the feedback loop. A phase-tracking amplifier, which would adjust the driving frequency to maintain constant phase shift over the second sound transducer pair, may be a more reliable solution, but it relies on the assumption that phase shift is constant at resonance. Preliminary testing suggests that this is the case for even harmonics, but more thorough testing is needed.

A final recommendation for continuation of the grid turbulence visualization experiment is to redesign the particle delivery tube. This is a costly endeavor but would solve multiple issues and help smooth the data acquisition and analysis processes. The first issue is that when the injector tube breaks the free surface of the liquid helium bath, it seems to induce surface waves that propagate into the bulk liquid in the channel after several seconds, overwhelming the effects of the grid-generated turbulence at later decay times. This effect is more pronounced at lower temperatures. The second issue is also related to moving the tube above the liquid surface, as doing so seems to release residual D_2, which then falls into the channel and appears in the image

data as overwhelmingly large clusters, which must be removed by hand during the data analysis phase. For the counterflow experiment, this is not an issue since the tube is retracted before data acquisition begins, and data acquisition can be delayed while the residual D_2 settles. However, for grid turbulence, data acquisition must begin even while the grid is in motion, so the large clusters are inevitable. Ideally, the delivery tube would be separated from the linear drive shaft, so that they can be moved independently, or at least, so the tube can be retracted before the grid is pulled. Implementation will probably require significant modifications to the drive shaft and channel support structure, but the resulting improvement to data quality would surely be worth the effort.

APPENDIX A

COPYRIGHT PERMISSIONS

Figures 1.1, 1.2, and 1.3 are from *Helium Cryogenics* by S. W. Van Sciver [9]. Permission to use these figures was obtained from the publisher, and the agreements are reproduced here.

This Agreement between Brian Mastracci ("You") and Springer Nature ("Springer Nature") consists of your license details and the terms and conditions provided by Springer Nature and Copyright Clearance Center.

License Number	4394891488432
License date	Jul 23, 2018
Licensed Content Publisher	Springer Nature
Licensed Content Publication	Springer eBook
Licensed Content Title	Helium as a Quantum Fluid
Licensed Content Author	Steven W. Van Sciver
Licensed Content Date	Jan 1, 2012
Type of Use	Thesis/Dissertation
Requestor type	academic/university or research institute
Format	electronic
Portion	figures/tables/illustrations
Number of figures/tables /illustrations	2
Will you be translating?	no
Circulation/distribution	<501
Author of this Springer Nature content	no
Title	Application of particle tracking velocimetry to thermal counterflow and towed-grid turbulence in Helium II
Instructor name	Dr. Wei Guo
Institution name	Florida State University
Expected presentation date	Aug 2018
Portions	Figures 6.13 and 6.19

For Journal Content:
Reprinted by permission from [the Licensor]: [Journal Publisher (e.g. Nature/Springer/Palgrave)] [JOURNAL NAME] [REFERENCE CITATION (Article name, Author(s) Name), [COPYRIGHT] (year of publication)

For Advance Online Publication papers:
Reprinted by permission from [the Licensor]: [Journal Publisher (e.g. Nature/Springer/Palgrave)] [JOURNAL NAME] [REFERENCE CITATION (Article name, Author(s) Name), [COPYRIGHT] (year of publication), advance online publication, day month year (doi: 10.1038/sj.[JOURNAL ACRONYM].)

For Adaptations/Translations:
Adapted/Translated by permission from [the Licensor]: [Journal Publisher (e.g. Nature/Springer/Palgrave)] [JOURNAL NAME] [REFERENCE CITATION (Article name, Author(s) Name), [COPYRIGHT] (year of publication)

Note: For any republication from the British Journal of Cancer, the following credit line style applies:

Reprinted/adapted/translated by permission from [the Licensor]: on behalf of Cancer Research UK: : [Journal Publisher (e.g. Nature/Springer/Palgrave)] [JOURNAL NAME] [REFERENCE CITATION (Article name, Author(s) Name), [COPYRIGHT] (year of publication)

For Advance Online Publication papers:
Reprinted by permission from The [the Licensor]: on behalf of Cancer Research UK: [Journal Publisher (e.g. Nature/Springer/Palgrave)] [JOURNAL NAME] [REFERENCE CITATION (Article name, Author(s) Name), [COPYRIGHT] (year of publication), advance online publication, day month year (doi: 10.1038/sj.[JOURNAL ACRONYM])

For Book content:
Reprinted/adapted by permission from [the Licensor]: [Book Publisher (e.g. Palgrave Macmillan, Springer etc) [Book Title] by [Book author(s)] [COPYRIGHT] (year of publication)

Other Conditions:

Version 1.0

REFERENCES

[1] R. de Bruyn Ouboter, "Superconductivity: Discoveries during the early years of low temperature research at Leiden 1908–1914," IEEE Trans. Magnetics **23**, 355 (1987).

[2] C. H. Rode, D. Arenius, W. C. Chronis, D. Kashy, and M. Keesee, "2.0 K CEBAF cryogenics," in *Adv. Cryo. Eng.*, volume 35 (Plenum Press, New York, 1990).

[3] F. Millet, P. Roussel, L. Tavian, and U. Wagner, "A possible 1.8 K refrigeration cycle for the large hadron collider," in *Adv. Cryo. Eng.*, volume 43 (Plenum Press, New York, 1998).

[4] S. W. Van Sciver, R. J. Miller, S. Welton, H. J. Schneider-Muntau, and G. McIntosh, "Cryogenic system for the 45 Tesla hybrid magnet," in *Adv. Cryo. Eng.*, volume 39 (Plenum Press, New York, 1994).

[5] P. V. Mason, "Science and applications of He-II in space," in *Adv. Cryo. Eng.*, volume 35 (Plenum Press, New York, 1990).

[6] L. Skrbek, J. J. Niemela, and R. J. Donnelly, "Turbulent flows at cryogenic temperatures: a new frontier," J. Phys.: Condens. Matter **11**, 7761 (1999).

[7] K. R. Sreenivasan and R. J. Donnelly, "Role of cryogenic helium in classical fluid dynamics: Basic research and model testing," Adv. Appl. Mech. **37**, 239 (2001).

[8] W. F. Vinen, "Fifty years of superfluid helium," in *Adv. Cryo. Eng.*, volume 35 (Plenum Press, New York, 1990).

[9] S. W. Van Sciver, *Helium Cryogenics* (Springer, New York, 2012).

[10] L. Tisza, "Transport phenomena in helium II," Nature **141**, 913 (1938).

[11] L. Landau, "Theory of the superfluidity of helium II," Phys. Rev. **60**, 356 (1941).

[12] D. V. Osborne, "The rotation of liquid helium II," Proc. Phys. Soc. A **63**, 909 (1950).

[13] C. J. Gorter and J. H. Mellink, "On the irreversible processes in liquid helium II," Physica **15**, 285 (1949).

[14] H. E. Hall and W. F. Vinen, "The rotation of liquid helium II I. Experiments on the propagation of second sound in uniformly rotating helium II," Proc. R. Soc. London Ser. A **238**, 204 (1956).

[15] R. P. Feynman, "Application of quantum mechanics to liquid helium," in *Progress in Low Temperature Physics*, volume 1 (Elsevier, Amsterdam, 1955).

[16] G. A. Williams and R. E. Packard, "Photographs of quantized vortex lines in rotating He II," Phys. Rev. Lett. **33**, 280 (1974).

[17] G. P. Bewley, D. P. Lathrop, and K. R. Sreenivasan, "Superfluid helium: Visualization of quantized vortices," Nature **441**, 588 (2006).

[18] H. E. Hall and W. F. Vinen, "The rotation of liquid helium II II. The theory of mutual friction in uniformly rotating helium II," Proc. R. Soc. London Ser. A **238**, 215 (1956).

[19] W. F. Vinen, "Mutual friction in a heat current in liquid helium II. II. Experiments on transient effects," Proc. R. Soc. London, Ser. A **240**, 128 (1957).

[20] W. F. Vinen, "Mutual friction in a heat current in liquid helium II. III. Theory of the mutual friction," Proc. R. Soc. London, Ser. A **242**, 493 (1957).

[21] R. J. Donnelly and C. E. Swanson, "Quantum turbulence," J. Fluid Mech. **173**, 387 (1986).

[22] W. Guo, S. B. Cahn, J. A. Nikkel, W. F. Vinen, and D. N. McKinsey, "Visualization study of counterflow in superfluid ^{4}He using metastable helium molecules," Phys. Rev. Lett. **105**, 045301 (2010).

[23] A. Marakov, J. Gao, W. Guo, S. W. Van Sciver, G. G. Ihas, D. N. McKinsey, and W. F. Vinen, "Visualization of the normal-fluid turbulence in counterflowing superfluid ^{4}He," Phys. Rev. B **91**, 094503 (2015).

[24] C. E. Chase, "Thermal conduction in liquid helium II. I. Temperature dependence," Phys. Rev. **127**, 361 (1962).

[25] P. E. Dimotakis and J. E. Broadwell, "Local temperature measurements in supercritical counterflow in liquid helium II," Phys. Fluids **16**, 1787 (1973).

[26] R. K. Childers and J. T. Tough, "Helium II thermal counterflow: Temperature- and pressure-difference data and analysis in terms of the Vinen theory," Phys. Rev. B **13**, 1040 (1976).

[27] K. P. Martin and J. T. Tough, "Evolution of superfluid turbulence in thermal counterflow," Phys. Rev. B **27**, 2788 (1983).

[28] S. Babuin, M. Stammeier, E. Varga, M. Rotter, and L. Skrbek, "Quantum turbulence of bellows-driven ^{4}He superflow: Steady state," Phys. Rev. B **86**, 134515 (2012).

[29] J. Gao, E. Varga, W. Guo, and W. F. Vinen, "Energy spectrum of thermal counterflow turbulence in superfluid helium-4," Phys. Rev. B **96**, 094511 (2017).

[30] E. Varga, S. Babuin, and L. Skrbek, "Second-sound studies of coflow and counterflow of superfluid 4He in channels," Phys. Fluids **27**, 065101 (2015).

[31] S. R. Stalp, L. Skrbek, and R. J. Donnelly, "Decay of grid turbulence in a finite channel," Phys. Rev. Lett. **82**, 4831 (1999).

[32] J. Maurer and P. Tabeling, "Local investigation of superfluid turbulence," Europhys. Lett. **43**, 29 (1998).

[33] B. Saint-Michel, E. Herbert, J. Salort, C. Baudet, M. B. Mardion, P. Bonnay, M. Bourgoin, B. Castaing, L. Chevillard, F. Daviaud, P. Diribarne, B. Dubrulle, Y. Gagne, M. Gibert, A. Girard, B. Hbral, T. Lehner, and B. Rousset, "Probing quantum and classical turbulence analogy in von Kármán liquid helium, nitrogen, and water experiments," Phys. Fluids **26**, 125109 (2014).

[34] J. Salort, C. Baudet, B. Castaing, B. Chabaud, F. Daviaud, T. Didelot, P. Diribarne, B. Dubrulle, Y. Gagne, F. Gauthier, A. Girard, B. Hbral, B. Rousset, P. Thibault, and P.-E. Roche, "Turbulent velocity spectra in superfluid flows," Phys. Fluids **22**, 125102 (2010).

[35] S. Babuin, E. Varga, and L. Skrbek, "The decay of forced turbulent coflow of He II past a grid," J. Low Temp. Phys. **175**, 324 (2014).

[36] W. F. Vinen, "Classical character of turbulence in a quantum liquid," Phys. Rev. B **61**, 1410 (2000).

[37] A. W. Baggaley, C. F. Barenghi, A. Shukurov, and Y. A. Sergeev, "Coherent vortex structures in quantum turbulence," Europhys. Lett. **98**, 26002 (2012).

[38] D. Kivotides, "Interactions between normal-fluid and superfluid vortex rings in helium-4," Europhys. Lett. **112**, 36005 (2015).

[39] L. Boué, V. L'vov, A. Pomyalov, and I. Procaccia, "Enhancement of intermittency in superfluid turbulence," Phys. Rev. Lett. **110**, 014502 (2013).

[40] E. Rusaouen, B. Chabaud, J. Salort, and P.-E. Roche, "Intermittency of quantum turbulence with superfluid fractions from 0% to 96%," Phys. Fluids **29**, 105108 (2017).

[41] R. A. Sherlock and D. O. Edwards, "Oscillating superleak second sound transducers," Rev. Sci. Instrum. **41**, 1603 (1970).

[42] S. R. Stalp, *Decay of grid turbulence in superfluid helium*, Ph.D. thesis, University of Oregon (1998).

[43] L. Skrbek and K. R. Sreenivasan, "Developed quantum turbulence and its decay," Phys. Fluids **24**, 011301 (2012).

[44] R. J. Donnelly and C. F. Barenghi, "The observed properties of liquid helium at the saturated vapor pressure," J. Phys. Chem. Ref. Data **27**, 1217 (1998).

[45] M. Raffel, C. Willert, and J. Kompenhans, *Particle Image Velocimetry* (Springer, Berlin, 1998).

[46] D. Celik, M. R. Smith, and S. W. Van Sciver, "A particle seeding apparatus for cryogenic flow visualization," in *Adv. Cryo. Eng.*, volume 45 (Plenum Press, New York, 2000).

[47] G. P. Bewley, K. R. Sreenivasan, and D. P. Lathrop, "Particles for tracing turbulent liquid helium," Exp. Fluids **44**, 887 (2008).

[48] T. V. Chagovets and S. W. Van Sciver, "A study of thermal counterflow using particle tracking velocimetry," Phys. Fluids **23**, 107102 (2011).

[49] P. E. Parks and R. J. Donnelly, "Radii of positive and negative ions in helium II," Phys. Rev. Lett. **16**, 45 (1966).

[50] D. Kivotides, "Normal-fluid velocity measurement and superfluid vortex detection in thermal counterflow turbulence," Phys. Rev. B **78**, 224501 (2008).

[51] Y. Mineda, M. Tsubota, Y. A. Sergeev, C. F. Barenghi, and W. F. Vinen, "Velocity distributions of tracer particles in thermal counterflow in superfluid ^{4}He," Phys. Rev. B **87**, 174508 (2013).

[52] M. S. Paoletti, R. B. Fiorito, K. R. Sreenivasan, and D. P. Lathrop, "Visualization of superfluid helium flow," J. Phys. Soc. Jpn. **77**, 111007 (2008).

[53] Y. A. Sergeev and C. F. Barenghi, "Particles-vortex interactions and flow visualization in 4He," J. Low Temp. Phys. **157**, 429 (2009).

[54] T. Zhang and S. W. Van Sciver, "The motion of micron-sized particles in He II counterflow as observed by the PIV technique," J. Low Temp. Phys. **138**, 865 (2005).

[55] T. Zhang and S. W. Van Sciver, "Large-scale turbulent flow around a cylinder in counterflow superfluid ^{4}He (He(II))," Nature Phys. **1**, 36 (2005).

[56] T. V. Chagovets and S. W. V. Sciver, "Visualization of He II counterflow around a cylinder," Phys. Fluids **25**, 105104 (2013).

[57] D. Duda, M. La Mantia, M. Rotter, and L. Skrbek, "On the visualization of thermal counterflow of He II past a circular cylinder," J. Low Temp. Phys. **175**, 331 (2014).

[58] T. V. Chagovets and S. W. Van Sciver, "Visualization of He II forced flow around a cylinder," Phys. Fluids **27**, 045111 (2015).

[59] T. Xu and S. W. Van Sciver, "Particle image velocimetry measurements of the velocity profile in HeII forced flow," Phys. Fluids **19**, 071703 (2007).

[60] G. P. Bewley, M. S. Paoletti, K. R. Sreenivasan, and D. P. Lathrop, "Characterization of reconnecting vortices in superfluid helium," Proc. Natl. Acad. Sci. USA **105**, 13707 (2008).

[61] M. S. Paoletti, M. E. Fisher, and D. P. Lathrop, "Reconnection dynamics for quantized vortices," Physica D **239**, 1367 (2010).

[62] E. Fonda, D. P. Meichle, N. T. Ouellette, S. Hormoz, and D. P. Lathrop, "Direct observation of kelvin waves excited by quantized vortex reconnection," Proc. Natl. Acad. Sci. USA **111**, 4707 (2014).

[63] P. Švančara and M. La Mantia, "Flows of liquid 4He due to oscillating grids," J. Fluid Mech. **832**, 578 (2017).

[64] J. Gao, A. Marakov, W. Guo, B. T. Pawlowski, S. W. Van Sciver, G. G. Ihas, D. N. McKinsey, and W. F. Vinen, "Producing and imaging a thin line of He2 molecular tracers in helium-4," Rev. Sci. Instrum. **86**, 093904 (2015).

[65] J. Gao, W. Guo, and W. F. Vinen, "Determination of the effective kinematic viscosity for the decay of quasiclassical turbulence in superfluid ^{4}He," Phys. Rev. B **94**, 094502 (2016).

[66] S. Fuzier, B. Baudouy, and S. W. Van Sciver, "Steady-state pressure drop and heat transfer in He II forced flow at high reynolds number," Cryogenics **41**, 453 (2001).

[67] J. O. Hinze, *Turbulence* (McGraw-Hill, 1975).

[68] D. Celik and S. W. Van Sciver, "Large size optical windows for superfluid helium applications," Cryogenics **42**, 547 (2002).

[69] SCHOTT North America, Inc., 400 York Ave., Duryea, PA 18642.

[70] The Chemours Company, 1007 Market St., Wilmington, DE 19899.

[71] Changchun New Industries Optoelectronics Tech. Co., Ltd., No. 888 Jinhu Rd., Changchun, 130103 China.

[72] Integrated Design Tools, 1804 Miccosukee Commons Suite 208, Tallahassee, FL 32308.

[73] Nikon, Inc., 1300 Walt Whitman Rd., Melville, NY 11747.

[74] SCIGRIP Americas, 600 Ellis Rd., Durham, NC 27703.

[75] Henkel AG & Co. KGaA, Henkel AG & Co. KGaA, 40191 Düsseldorf, Germany.

[76] J. W. Ekin, *Experimental Techniques for Low-Temperature Measurements* (Oxford University Press, New York, 2006).

[77] Lake Shore Cryotronics, Inc., 575 McCorkle Blvd., Westerville, OH 43082.

[78] R. C. Dhuley and S. W. Van Sciver, "Epoxy encapsulation of the cernox^{TM} SD thermometer for measuring the temperature of surfaces in liquid helium," Cryogenics **77**, 49 (2016).

[79] Sterlitech Corporation, 22027 70th Ave. S., Kent, WA 98032.

[80] H. J. S. Fernando and I. P. D. De Silva, "Note on secondary flows in oscillating-grid, mixing-box experiments," Phys.Fluids A **5**, 1849 (1993).

[81] R. E. Honey, R. Hershberger, R. J. Donnelly, and D. Bolster, "Oscillating-grid experiments in water and superfluid helium," Phys. Rev. E **89**, 053016 (2014).

[82] C. M. White, A. N. Karpetis, and K. R. Sreenivasan, "High-Reynolds-number turbulence in small apparatus: grid turbulence in cryogenic liquids," J. Fluid Mech. **452**, 189 (2002).

[83] M. R. Smith, R. J. Donnelly, N. Goldenfeld, and W. F. Vinen, "Decay of vorticity in homogeneous turbulence," Phys. Rev. Lett. **71**, 2583 (1993).

[84] Bellowstech, 1289 N U.S. Highway 1, Ormond Beach, FL 32174.

[85] Kuraray America, Inc., 2625 Bay Area Blvd., Suite 600, Houston, TX 77058.

[86] Parker Hannifin Corporation, Electromechanical and Drives Division, 9225 Forsyth Park Dr., Charlotte, NC 28273.

[87] B. Mastracci and W. Guo, "An apparatus for generation and quantitative measurement of homogeneous isotropic turbulence in He II," Rev. Sci. Instrum. **89**, 015107 (2018).

[88] MKS Instruments, Inc., 2 Tech Dr., Suite 201, Andover, MA 01810.

[89] National Instruments, 11500 N. Mopac Expwy., Austin, TX 78759.

[90] Stanford Research Systems, 1290-D Reamwood Ave., Sunnyvale, CA 94089.

[91] M. Liu and M. R. Stern, "Oscillating superleak transducer of second sound," Phys. Rev. Lett. **48**, 1842 (1982).

[92] E. Varga, S. Babuin, V. S. L'vov, A. Pomyalov, and L. Skrbek, "Transition to quantum turbulence and streamwise inhomogeneity of vortex tangle in thermal counterflow," J. Low Temp. Phys. **187**, 531 (2017).

[93] J. Yang, G. G. Ihas, and D. Ekdahl, "Second sound tracking system," Rev. Sci. Instrum. **88**, 104705 (2017).

[94] M. La Mantia, T. V. Chagovets, M. Rotter, and L. Skrbek, "Testing the performance of a cryogenic visualization system on thermal counterflow by using hydrogen and deuterium solid tracers," Rev. Sci. Instrum. **83**, 055109 (2012).

[95] M. La Mantia and L. Skrbek, "Quantum turbulence visualized by particle dynamics," Phys. Rev. B **90**, 014519 (2014).

[96] Quantum Composers, Inc., 212 Discovery Dr., Bozeman, MT 59718.

[97] I. F. Sbalzarini and P. Koumoutsakos, "Feature point tracking and trajectory analysis for video imaging in cell biology," J. Struct. Biol. **151**, 182 (2005).

[98] J. C. Crocker and D. G. Grier, "Methods of digital video microscopy for colloidal studies," J. Coll. Interface Sci. **179**, 298 (1996).

[99] The MathWorks, Inc., 1 Apple Hill Dr., Natick, MA 01760.

[100] W. Guo, M. La Mantia, D. P. Lathrop, and S. W. Van Sciver, "Visualization of two-fluid flows of superfluid helium-4," Proc. Natl. Acad. Sci. USA **111**, 4653 (2014).

[101] Y. A. Sergeev, C. F. Barenghi, and D. Kivotides, "Motion of micron-size particles in turbulent helium II," Phys. Rev. B **74**, 184506 (2006).

[102] M. La Mantia, "Particle trajectories in thermal counterflow of superfluid helium in a wide channel of square cross section," Phys. Fluids **28**, 024102 (2016).

[103] W. Kubo and Y. Tsuji, "Lagrangian trajectory of small particles in superfluid He II," J. Low Temp. Phys. **187**, 611 (2017).

[104] D. Kivotides, "Motion of a spherical solid particle in thermal counterflow turbulence," Phys. Rev. B **77**, 174508 (2008).

[105] M. La Mantia and L. Skrbek, "Quantum, or classical turbulence?" Europhys. Lett. **105**, 46002 (2014).

[106] M. S. Paoletti, M. E. Fisher, K. R. Sreenivasan, and D. P. Lathrop, "Velocity statistics distinguish quantum turbulence from classical turbulence," Phys. Rev. Lett. **101**, 154501 (2008).

[107] C. F. Barenghi, D. Kivotides, and Y. A. Sergeev, "Close approach of a spherical particle and a quantised vortex in helium II," J. Low Temp. Phys. **148**, 293 (2007).

[108] D. Kivotides, C. F. Barenghi, and Y. A. Sergeev, "Interactions between particles and quantized vortices in superfluid helium," Phys. Rev. B **77**, 014527 (2008).

[109] R. T. Wang, C. E. Swanson, and R. J. Donnelly, "Anisotropy and drift of a vortex tangle in helium II," Phys. Rev. B **36**, 5240 (1987).

[110] M. La Mantia, D. Duda, M. Rotter, and L. Skrbek, "Lagrangian accelerations of particles in superfluid turbulence," J. Fluid Mech. **717**, R9 (2013).

[111] M. La Mantia, P. Švančara, D. Duda, and L. Skrbek, "Small-scale universality of particle dynamics in quantum turbulence," Phys. Rev. B **94**, 184512 (2016).

[112] J. Gao, W. Guo, V. L'vov, A. Pomyalov, L. Skrbek, E. Varga, and W. Vinen, "The decay of counterflow turbulence in superfluid ^{4}He," JETP Lett. **103**, 648 (2016).

[113] W. F. Vinen, (Private communication, to be published).

[114] W. F. Vinen and J. J. Niemela, "Quantum turbulence," J. Low Temp. Phys. **128**, 167 (2002).

[115] J. Gao, W. Guo, S. Yui, M. Tsubota, and W. F. Vinen, "Dissipation in quantum turbulence in superfluid ^{4}He above 1 k," Phys. Rev. B **97**, 184518 (2018).

[116] K. W. Schwarz, "Three-dimensional vortex dynamics in superfluid ^{4}He: Homogeneous superfluid turbulence," Phys. Rev. B **38**, 2398 (1988).

[117] B. Mastracci and W. Guo, "Exploration of thermal counterflow in He II using particle tracking velocimetry," Phys. Rev. Fluids **3**, 063304 (2018).

[118] I. A. Min, I. Mezi, and A. Leonard, "Lévy stable distributions for velocity and velocity difference in systems of vortex elements," Phys. Fluids **8**, 1169 (1996).

[119] M. S. Paoletti and D. P. Lathrop, "Quantum turbulence," Annu. Rev. Con. Mat. Phys. **2**, 213 (2011).

[120] A. T. A. M. de Waele and R. G. K. M. Aarts, "Route to vortex reconnection," Phys. Rev. Lett. **72**, 482 (1994).

[121] E. Varga and L. Skrbek, "Dynamics of the density of quantized vortex lines in counterflow turbulence: Experimental investigation," Phys. Rev. B **97**, 064507 (2018).

[122] S. R. Stalp, J. J. Niemela, W. F. Vinen, and R. J. Donnelly, "Dissipation of grid turbulence in helium II," Phys. Fluids **14**, 1377 (2002).

[123] R. A. Ashton and J. A. Northby, "Vortex velocity in turbulent he ii counterflow," Phys. Rev. Lett. **35**, 1714 (1975).

[124] D. D. Awschalom, F. P. Milliken, and K. W. Schwarz, "Properties of superfluid turbulence in a large channel," Phys. Rev. Lett. **53**, 1372 (1984).

[125] L. Skrbek and S. R. Stalp, "On the decay of homogeneous isotropic turbulence," Phys. Fluids **12**, 1997 (2000).

[126] L. Skrbek, J. J. Niemela, and R. J. Donnelly, "Four regimes of decaying grid turbulence in a finite channel," Phys. Rev. Lett. **85**, 2973 (2000).

[127] E. Varga, J. Gao, W. Guo, and L. Skrbek, "Intermittency enhancement in quantum turbulence," arXiv:1806.11353 [physics.flu-dyn].

[128] P. K. Kundu, I. M. Cohen, and D. R. Dowling, *Fluid Mechanics* (Elsevier, Amsterdam, 2012).

[129] D. E. Zmeev, P. M. Walmsley, A. I. Golov, P. V. E. McClintock, S. N. Fisher, and W. F. Vinen, "Dissipation of quasiclassical turbulence in superfluid ^{4}He," Phys. Rev. Lett. **115**, 155303 (2015).

[130] L. Biferale, D. Khomenko, V. L'vov, A. Pomyalov, I. Procaccia, and G. Sahoo, "Turbulent statistics and intermittency enhancement in coflowing superfluid ^{4}He," Phys. Rev. Fluids **3**, 024605 (2018).

[131] R. Benzi, L. Biferale, G. Paladin, A. Vulpiani, and M. Vergassola, "Multifractality in the statistics of the velocity gradients in turbulence," Phys. Rev. Lett. **67**, 2299 (1991).

[132] H. Xu, N. T. Ouellette, and E. Bodenschatz, "Curvature of Lagrangian trajectories in turbulence," Phys. Rev. Lett. **98**, 050201 (2007).

[133] S. Burov, S. M. A. Tabei, T. Huynh, M. P. Murrell, L. H. Philipson, S. A. Rice, M. L. Gardel, N. F. Scherer, and A. R. Dinner, "Distribution of directional change as a signature of complex dynamics," Proc. Natl. Acad. Sci. USA **110**, 19689 (2013).

[134] W. J. T. Bos, B. Kadoch, and K. Schneider, "Angular statistics of Lagrangian trajectories in turbulence," Phys. Rev. Lett. **114**, 214502 (2015).

[135] A. Bhatnagar, A. Gupta, D. Mitra, P. Perlekar, M. Wilkinson, and R. Pandit, "Deviation-angle and trajectory statistics for inertial particles in turbulence," Phys. Rev. E **94**, 063112 (2016).

[136] C. F. Barenghi, (Private communication).

BIOGRAPHICAL SKETCH

Brian Mastracci holds a B.S. in Mechanical Engineering from Virginia Tech and is currently pursuing a Ph.D. in Mechanical Engineering (Cryogenics) at Florida State University.

Publications

B. Mastracci and W. Guo, "Study of vortex dynamics in He II counterflow using particle tracking velocimetry," to be submitted to the Physical Review (2018).

B. Mastracci, W. Guo, and W. F. Vinen, "Particle tracking velocimetry applied to thermal counterflow in superfluid ^{4}He: motion of the normal fluid at small heat fluxes," to be submitted to Phys. Rev. Fluids (2018).

B. Mastracci and W. Guo, "Exploration of thermal counterflow in He II using particle tracking velocimetry," Phys. Rev. Fluids **3**, 063304 (2018).

B. Mastracci and W. Guo, "An apparatus for generation and quantitative measurement of homogeneous isotropic turbulence in He II," Rev. Sci. Instrum. **89**, 015107 (2018).

B. Mastracci and W. Guo, "Visualization of grid-generated turbulence in He II using PTV," IOP Conf. Ser.: Mater. Sci. Eng. **278**, 012081 (2017).

B. Mastracci, S. Takada, and W. Guo, Study of particle motion in He II counterflow across a wide heat flux range," J. Low Temp. Phys. **187**, 446 (2017).

Presentations

B. Mastracci and W. Guo, "Visualization of grid-generated turbulence in He II using PTV," 2017 Joint Cryogenic Engineering Conference and International Cryogenic Materials Conference, July 9–13 2017, Madison WI, USA.

B. Mastracci and W. Guo, "Visualization of grid-generated turbulence in He II using PTV," Quantum Turbulence Workshop, April 10–12 2017, Tallahassee FL, USA.

B. Mastracci, S. Takada, and W. Guo, "Study of particle motion in He II counterflow across a wide heat flux range," International Conference on Quantum Fluids and Solids 2016, Aug. 10–16 2016, Prague, Czech Republic.

B. Mastracci and W. Guo, "Experimental methods for PTV measurement of various liquid helium flows," 11th International Symposium on Particle Image Velocimetry, Sep. 14–16 2015, Santa Barbara CA, USA.